2018

Assessment of Microstructure and Mechanical Behavior of Materials and Phases Observed in Low-Enriched Uranium Monolithic Fuel Plates After Fabrication

Ryan Newell

ASSESSMENT OF MICROSTRUCTURE AND MECHANICAL BEHAVIOR OF MATERIALS AND PHASES OBSERVED IN LOW-ENRICHED URANIUM MONOLITHIC FUEL PLATES AFTER FABRICATION

by

RYAN J. NEWELL II
B.S. University of Central Florida, 2014

A dissertation submitted in partial fulfillment of the requirements
for the degree of Doctor of Philosophy
in the Department of Materials Science and Engineering
in the College of Engineering and Computer Science
at the University of Central Florida
Orlando, Florida

Fall Term
2018

Major Professor: Yongho Sohn

ABSTRACT

Low enriched uranium (LEU) fuels are being developed to reduce the use of highly enriched uranium in power generation to reduce proliferation risks. Challenges arise in providing sufficient fissile U in LEU without reactor redesign. As such, a novel monolithic fuel plate design employs LEU alloyed with 10 wt. % Mo. Throughout fabrication of these fuel plates, metallurgical transformations and reactions take place as a result of elevated temperatures during processing. The transformations include decomposition of the metastable body-centered cubic γ phase in the fuel and metallurgical interactions at interfaces between fuel plate components. This work aims to provide further understanding into physical and mechanical behavior of these constituents as they relate to fuel plate processing and performance. Fuel plate processing includes alloying the U, applying a Zr diffusion barrier, and cladding in AA6061 via hot isostatic press. Experimental Zr barriers were applied via electroplating, plasma-spraying, or roll-bonding and characterized using optical and electron microscopy, demonstrating that roll-bonded Zr exhibits the most favorable properties. During fabrication, regions of the γ-U decompose into α and γ' which revert to γ during annealing or irradiation and heat treatments were designed to induce similar transformations and characterize them using x-ray diffraction and electron microscopy, resulting in a model describing the reversion as a function of time and temperature. The mechanical properties of the fuel and other constituent phases were investigated via instrumented indentation of fuel plates. Phases that occurred in small, discontinuous regions were fabricated in diffusion couples for more reliable indentation. The kinetic and mechanical data produced from this study can be used to estimate the

phase constitution of the fuel plates and subsequently, its behavior in response to fabrication and irradiation.

ACKNOWLEDGMENTS

I want to express my deepest gratitude to all of those who helped me throughout this journey. Thanks to my advisor, Dr. Yongho Sohn, for supporting and believing in me. Thanks to my committee for always giving me a positive support structure and helpful feedback. To all my colleagues, you have made this entire experience enjoyable. Finally, my friends and family, I couldn’t have done it without you.

TABLE OF CONTENTS

LIST OF FIGURES

LIST OF TABLES

CHAPTER 1: INTRODUCTION

1.1 Nuclear Power Generation

Global energy demand is rapidly increasing, ultimately leading to increased CO_2 production and emission. According to the International Energy Agency, global oil demand is projected to exceed 103 million barrels per day (mb/d) by 2040 if no global energy policies change, but must fall below 75 mb/d according to the 450 scenario [1]. The 450 scenario outlines a pathway by which the concentration of greenhouse gases in the atmosphere is limited to 450 parts per million (ppm) CO_2, resulting in a global temperature increase limited to 2°C [2]. To realize the 450 scenario, nuclear electricity generation must increase from its 2.4 trillion kWh in 2016 to 4.5 trillion kWh by 2040 [3].

The governing principal behind nuclear power generation is to convert the heat generated from splitting atomic nuclei into electricity. To capitalize on this phenomenon, neutrons bombard a fuel material (typically uranium-based), resulting in fission (splitting) of the U-235 and U-233 atoms. When the nuclei of the fissile atoms are split, heat is generated which is then converted to electricity with a steam turbine and a generator. The design of nuclear power plants is complex and involves many components, but the present work is dedicated to better understanding nuclear fuel materials for use in high-power research and test reactors.

1.2 Uranium Nuclear Fuel

The increased use of nuclear material is not without risks, however, which could include reactor failure and proliferation of nuclear material. To mitigate these risks, the Reduced Enrichment for Research and Test Reactors (RERTR) Program was conceived in 1978. RERTR was developed by the U.S. Department of Energy with three objectives: (1) development of

advanced low enriched uranium (LEU) fuels, (2) design and safety analysis for reactor conversion, and (3) development of targets and processes for the production of the medical isotope Mo-99 with LEU [4]. LEU fuel is defined by the International Atomic Energy Agency (IAEA) as having a fissile uranium (U-235 or U-233) concentration less than 20 percent by weight, which is unable to be utilized for nuclear explosive devices without further enrichment [5]. As plate-type reactors consume the majority of HEU, conversion efforts are aimed at the development of LEU fuel suitable for replacing HEU fuel in plate type reactors.

To this end, existing research and test reactors must undergo conversion from HEU to LEU fuel. To replace HEU fuels, newly developed LEU fuels must have fissile U densities capable of meeting existing reactor benchmarks. Pure U, however, exhibits anisotropic swelling and unfavorable irradiation behavior [6]. As such, it must be alloyed with other elements to promote stability during fabrication and irradiation. The consequent challenge lies in establishing a stable U-alloy that is capable of providing sufficient U density to directly convert HEU reactors. Early fuel plates designed for LEU conversion utilized uranium aluminides or oxides, which provided up to 2.4 and 3.2 g-U/cm^3, respectively [7]. The densities of these fuels were insufficient to directly convert plate-type HEU reactors without redesign. Subsequently, uranium silicide fuels were proposed, and after increasing the fuel density in the matrix, loading of 6.0 g-U/cm^3 was achieved [8]. The U-density available through silicide fuels was sufficient for conversion of most research reactors globally, but to completely convert high performance research and test reactors to LEU fuel, U-density must exceed 15 g/cm^3 [9].

The uranium loading in LEU fuel plates was not only limited by U-density in the fuel particles, however; the design of the plates contributed to the limitation. The required density of 15 g-U/cm^3 in the fuel particles was derived from a total U-density of 8-9 g/cm^3 required in the

plates required to convert existing reactors. This required density included the entire fuel/matrix region, only 55% of which was comprised of fuel particles [10]. The particle dispersion design would thus be physically limited to about 10.5 g-U/cm^3 if pure U particles were feasible for irradiation. The physical limitation prompted innovation in design, leading to the conception of a monolithic fuel plate design in which the particle/matrix region was replaced with a foil of U-alloy [10]. A schematic comparing the monolithic and dispersion fuel plate designs is shown in Figure 1. The monolithic design allows higher U loading and minimizes the contact area between foil and cladding, where metallurgical interactions between the U-based fuel and Al-based cladding can result in areas characterized by suboptimal mechanical and irradiation behavior. Ultimately, monolithic fuel plates will provide a high-density LEU fuel that replaces HEU fuel in research and test reactors. Following initial fabrication, testing, and characterization efforts, the monolithic fuel plate design with U10Mo alloy fuel has been selected for qualification for use in converting high performance research reactors per the United States high performance research reactor fuel qualification (USHPRR-FQ) program [11].

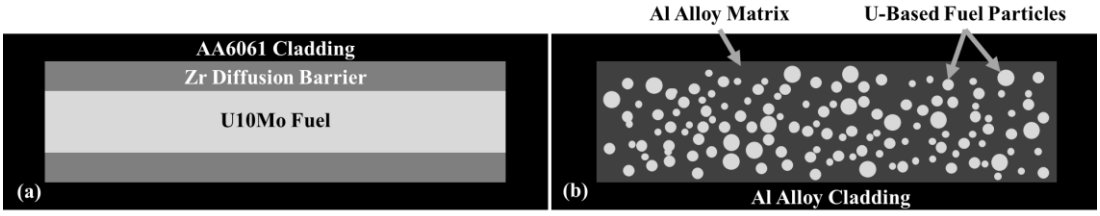

Figure 1. Schematic diagrams of (a) monolithic and (b) dispersion type LEU fuel plates.

1.3 Zirconium Diffusion Barrier

The U-Mo alloy fuel and the AA6061 cladding exhibit rapid and extensive interaction during fabrication and performance, and this phenomenon has been termed *fuel-cladding chemical interaction* (FCCI) [12]. To mitigate the rapid and extensive FCCI, a Zr diffusion barrier was

selected to laminate the fuel-cladding interfaces. In addition to relatively slow interaction with U-Mo alloys [13], Zr was selected as the diffusion barrier material on the basis of its compatibility with existing fabrication methods, thermal conductivity, thermal neutron cross-section, and corrosion resistance [14]. In order to fabricate these monolithic fuel plates with Zr diffusion barriers, the U10Mo fuel is typically co-rolled with Zr sheets, then subsequently undergoes hot isostatic pressing (HIP) to seal the coupon in AA6061 [15].

However, the roll-bonded (RB) Zr diffusion barriers are not without tradeoffs. Throughout the co-rolling and shearing processes, waste containing Zr and U10Mo alloy is generated, adding to the cost of the operation. Additionally, the sheared edges of the coupon remain uncovered, resulting in direct contact between the U10Mo alloys and AA6061 cladding, which may be prone to extensive FCCI. Chemical inhomogeneity (i.e., banding) has also been demonstrated in rolled U10Mo foils, leading to increased decomposition in low-Mo regions of the fuel plates during fabrication [16].

These drawbacks have prompted efforts to investigate alternative methods of applying the Zr diffusion barrier. Candidate techniques include plasma spraying (PS) and electroplating (EP). These techniques eliminate the roll-bonding and shearing operations that result in chemical banding and FCCI. The microstructure of the barriers and U10Mo/Zr interaction layers following the application of the Zr barriers have been documented [17]. However, the microstructural characteristics of the diffusion barriers and their interfacial regions have not been documented following the HIP process.

1.4 Motivation and Objectives

The USHPRR-FQ program aims to benchmark and qualify these monolithic fuels for long-term use in high-performance research and test reactors. The qualified fuels should be accident tolerant, meet power generation demands of high-power reactors, and utilize LEU as the fuel material. The monolithic fuel plate design is capable of meeting these criteria, but prior to its widescale application the behavior of the relevant materials and systems must be well understood and documented. The purpose of this work is to investigate the behavior of the fuel and diffusion barrier materials, specifically as they relate to fabrication and processing of LEU monolithic fuel plates. This includes identifying a preferred application method for Zr diffusion barriers between electroplating, plasma-spraying, or roll-bonding. Detailing the microstructure also includes investigating the decomposition mechanisms that occur in the fuel as a result of fabrication. Subsequently, the decomposed microstructure reverts to the γ phase during irradiation or during annealing, but the kinetics of the transformation or resulting grain structure have not been well documented. Detailed investigation of the microstructural evolution as it relates to fabrication can help provide an understanding on the constitution of the fuel plates prior to irradiation. Computational models can use this info to provide an initial condition in modeling and simulation of the fuel plates' mechanical response to the irradiation conditions. However, accurate and reliable mechanical properties of phases observed within the fuel plates are paramount to providing reliable simulation. Using nanonindentation, the hardness and reduced modulus of phases can be directly measured in the fuel plates, or phases that exist in fuel plates as fine or discontinuous features can be fabricated to be large and continuous in diffusion couples and subsequently indented. The reduced modulus can be used to calculate Young's modulus which can contribute

to calculating the stiffness and mechanical response of the fuel plate overall. The data provided in this study can lead to better understanding of the fuel plate microstructure and mechanical properties, thus promoting more accurate and reliable modeling of fuel plate behavior throughout fabrication and irradiation.

CHAPTER 2: LITERATURE REVIEW

2.1 Fuel Alloy Selection

The allotropes of uranium include the orthorhombic α phase, tetragonal β, and BCC γ, as shown in Figure 2. Elemental uranium exists in the α phase from -230 to 667°C [18-20]. The orthorhombic crystal structure, however, exhibits highly anisotropic swelling under irradiation [21-24]. The unstable performance of elemental α-U necessitates the use of a different crystal structure for uranium irradiation. The alternatives include U-rich intermetallic compounds and solid solutions achieved by alloying. In order to meet density requirements for direct reactor conversion, U_6Me (Me=transition metal) type fuels are the only viable intermetallic compounds [25]. U_6Mn [26] and U_6Fe [27] underwent breakaway swelling at relatively low fission densities, and it is assumed that other intermetallic compounds of this type would behave similarly. Thus, γ solid solutions are the only viable candidates for high performance LEU fuel.

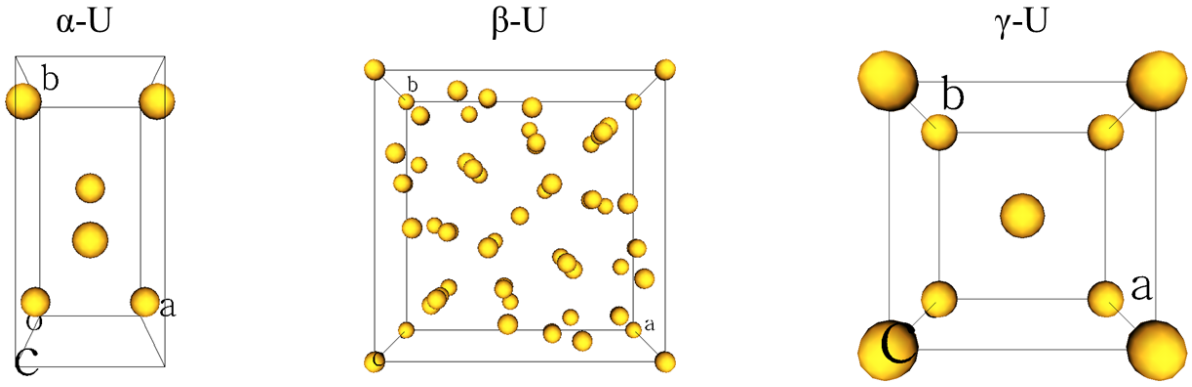

Figure 2. Crystal structures of the U allotropes orthorhombic α, tetragonal β, and BCC γ.

The BCC γ phase is stable in elemental uranium from 777 to 1132°C [28] and its transformation to room temperature equilibrium upon cooling can be hindered with the addition of alloying elements. Specifically, group IV-VIII transition metals form relatively stable solid

solutions with uranium [9, 29]. Of the transition metals, Mo has demonstrated high solubility in uranium (up to ~18 wt. %) and good γ stabilization. Many studies have been conducted to investigate the kinetics of γ decomposition in various U-Mo alloys [30-33], and alloys with 10 wt. % Mo represent a balance of high fissile U density and good stabilization of the metastable γ phase [34-37].

2.2 Phase Transformations in the U-Mo Binary System

The binary U-Mo phase diagram is shown in Figure 3, demonstrating the equilibrium compositions and temperatures for orthorhombic α and tetragonal β-U with negligible Mo solubility, body centered tetragonal U_2Mo (γ'), and BCC γ-U with close to 20 wt. % Mo solubility. The eutectoid point γ ↔ α+γ' exists at roughly 10 wt. % Mo and 560°C.

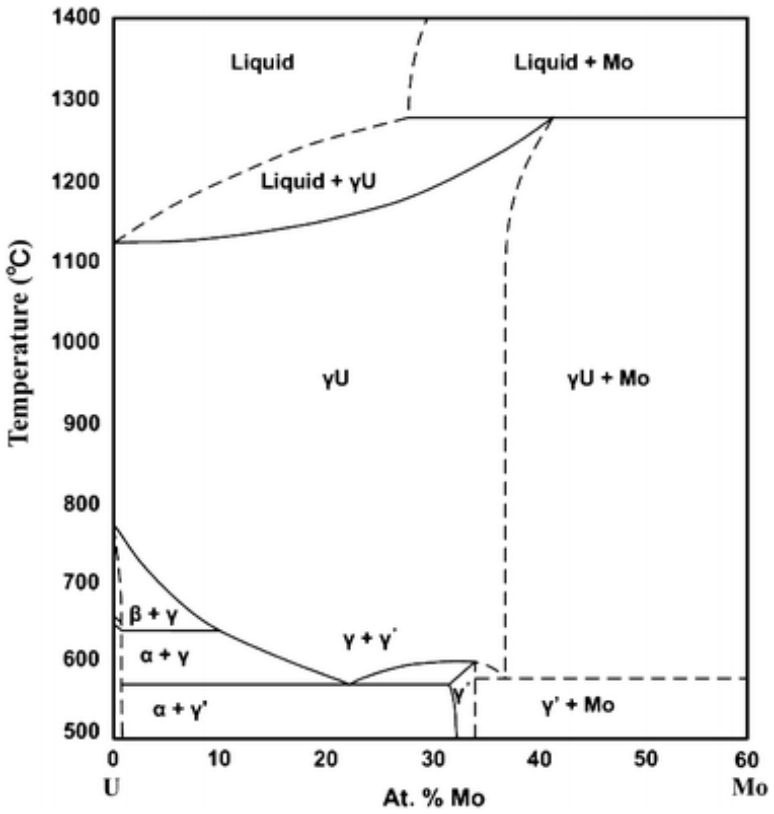

Figure 3. Equilibrium U-Mo binary phase diagram [38].

In early investigation into the U-Mo binary system Ahmann *et* al. [39] and Seybolt *et* al. [40] demonstrated that the γ phase could be retained in water quenched U alloys depending on Mo concentration. In the following years, several metastable phases were identified as cooling rates and Mo concentrations varied [41, 42]. Tangri *et* al. [43] investigated the effects of cooling rate and composition on the crystal structure of U-Mo alloys and reported that up to 11 at. % Mo additions resulted in the formation distorted crystal structures related to the α phase in water quenched U alloys, while alloys with higher Mo content were characterized by distortions of the γ phase. The α-related structures were deemed α': a structure similar to α with contraction of the *b* axis, and α": similar to α with a distortion of the monoclinic angle between *a* and *b* axes. The γ° phase was also reported, having a base-centered tetragonal structure obtained by doubling the *a* and *b* axes and contracting the *c* axis of the BCC γ structure. The phases originated from γ during cooling and occur in the following order: γ, γ°, α", α', α. Recently, Steiner *et* al. investigated the stiffness in U-8 wt. % Mo using resonant ultrasound spectroscopy [44] and provided detailed discussion on the transformation pathway observed as it relates to temperature. In short, the stiffness of the lattice depends on the Mo content in solid solution and the transformations that occur are hindered by increased stiffness associated with increased Mo content. With sufficiently slow cooling or annealing below 560°C, however, the equilibrium α+γ' phases are expected to form in U-Mo alloys per the T-T-T diagram shown in Figure 4 [31].

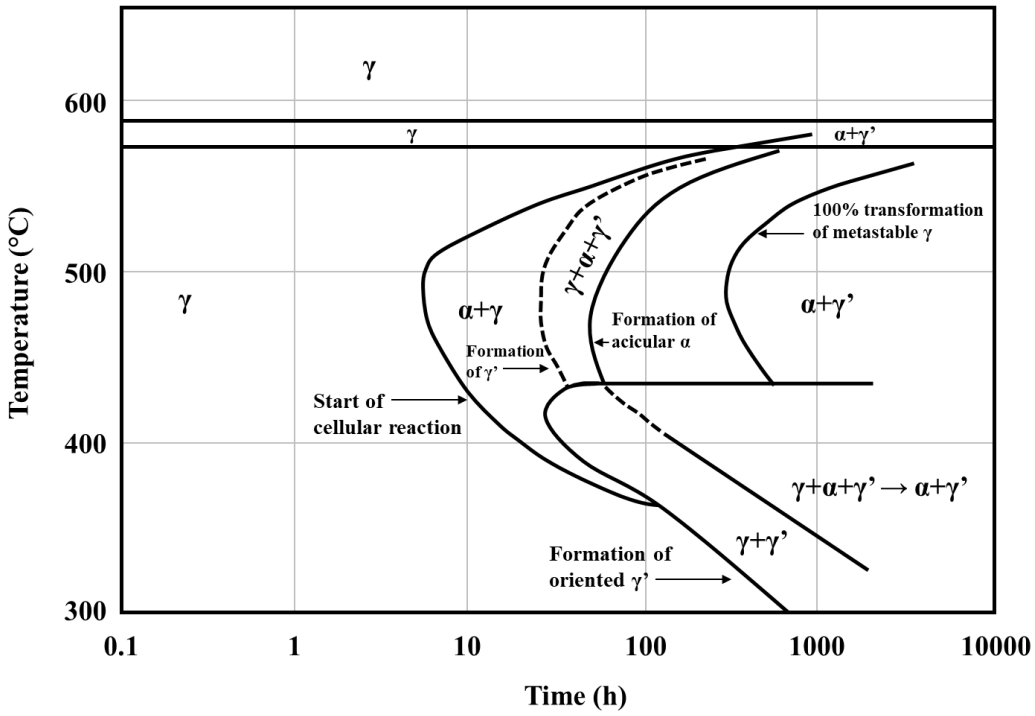

Figure 4. U10Mo alloy T-T-T diagram [31].

The decomposition of the γ phase, however, has been somewhat divisive in the literature describing the γ to α+γ' transformation, particularly regarding the kinetics of the transformation; the onset of decomposition has been reported in times ranging from less than 1 h [45] to as much as 30 h [30, 46] in U10Mo alloys. Throughout these early studies on the decomposition of γ-U10Mo, the transformation has mostly been discussed as typical eutectoid decomposition, however, discontinuous or cellular precipitation was suggested in low-Mo alloys [47, 48] and more recently in U10Mo alloys [49]. While the eutectoid transformation occurs via simultaneous nucleation and growth of the equilibrium phases (α+γ' in this case), the discontinuous precipitation reaction occurs discontinuously, growing with a moving reaction front [50] and containing lamellae of α, γ, and γ'. While these microstructures can be similar in appearance, the discontinuous precipitation microstructure also includes a compositionally different variant of the

initial matrix phase (γ in this case). In some cases, the compositionally different matrix phase remains metastable, and the initial discontinuous reaction is followed by a subsequent transformation resulting in the equilibrium microstructure [51, 52]. In the case of γ-U-Mo, an initial metastable discontinuous precipitation reaction results in a lamellar microstructure consisting of γ and one or both of α and γ' depending on composition and temperature [53]. To achieve the final equilibrium microstructure another reaction is required. Existing literature is lacking in the long-term decomposition kinetics and this second reaction is not extensively discussed in the U-Mo system. However, in the U-Nb system the initial metastable discontinuous precipitation is followed by discontinuous coarsening [54]. Discontinuous coarsening is marked by coarsened lamella resulting in a reduction in interfacial energy, and in the case of an initially metastable lamellar structure, the discontinuous coarsened microstructure represents a transformation to the equilibrium phases.

Grain boundaries act as nucleation sites for discontinuous precipitation and coarsening, which grow toward the grain interior following nucleation. However, within the grains alternative transformations take place. In addition to the lamellar microstructures observed following the discontinuous reaction, acicular α and γ' have been observed precipitating within the γ grains in U-Mo alloys [49]. The acicular features form via continuous precipitation, which competes with discontinuous precipitation to lower the free energy by consuming the metastable γ matrix. As a result, local growth of one of these modes of transformation impedes or suppresses the growth of the other due to hard impingement, reduced supersaturation in the matrix, and the Zener pinning effect [55]. Consequently, the decomposition kinetics are not only dependent on composition and temperature, but also on grain size which, until recently [56] has not been incorporated in existing U-Mo decomposition literature.

2.3 Isothermal Reversion Kinetics

Following decomposition, the α+γ' microstructure can be reverted to γ phase above the eutectoid temperature, however, this transformation has not been widely investigated. In contrast, the reaustenization of carbon steels has been extensively investigated and can provide a framework for analyzing γ reversion in U10Mo. In many cases, reaustenization is modeled using the approach proposed by Johnson and Mehl, Avrami, and Kolmogorov to describe isothermal transformations [57-59]. Johnson and Mehl [60], Avrami [61-63], and Kolmogorov [64] approached the problem of crystallization near concurrently and all arrived at the same general model. A generalized form is typically regarded as the Johnson-Mehl-Avrami-Kolmogorov (JMAK) model. The formula defines the transformed fraction of a given volume as equal to the probability of any point within the volume being transformed. Fanfoni and Tomellini [65] provided a brief review of the statistical considerations in deriving this formula.

Considering any circle centered at a random point *c* in a volume with radius *r(t)*, the probability that the circle contains only untransformed volume is defined by Eq. (1)

$$P(r) = e^{-N_0 \frac{4}{3}\pi r^3} \quad (1)$$

assuming nucleation as a Poisson process, where N_o is the density of nuclei, and *r* is radius of the circular cluster. This approach assumes that nuclei are randomly distributed and there is no critical size under which nuclei do not grow. Extending this treatment to a finite space, the generic nuclei density N_o becomes a set of specific nuclei *n*, each with numerical index *i*. Eq. (2) describes the probability of a specific cluster containing strictly untransformed volume.

$$P_i = e^{-n_i \pi r_i^2} \quad (2)$$

As the nucleation events are considered random and independent, the probability of the random point *c* existing in transformed space is then defined by Eq. (3).

$$P = \prod_i P_i = \prod_i e^{-n_i \frac{4}{3}\pi r_i^3} = e^{-\frac{4}{3}\pi \sum_i n_i r_i^3} \tag{3}$$

By definition, the probability of any random point to be transformed is equivalent to the transformed fraction of the volume. As such, the transformed fraction can be written in the form of Eq. (4)

$$P = V = 1 - e^{-\frac{4}{3}\pi \sum_i n_i r_i^3} = 1 - e^{-V_e} \tag{4}$$

where V_e is the extended volume, representing the volume transformed if overlap were not considered. With the assumptions of constant nucleation and spherical growth, the extended volume can be written as Eq. (5)

$$V_e = \frac{4}{3}\pi \dot{N} G^3 t^4 \tag{5}$$

where $\dot{N}$, G, and t are the nucleation rate, growth rate, and time, respectively. In the case of no new nucleation (site saturation), the extended volume is defined by Eq. (6)

$$V_e = \frac{4}{3}\pi N G^3 t^3 \tag{6}$$

where N is the number of preexisting nuclei.

In cases where the transformation is not dictated by constant nucleation and growth of spherical particles, however, the application of Eq. (5) or (6) into Eq. (4) is not justified. Some common deviations are derived to include the treatment of non-spherical or transient growth rates. Wert and Zener [66] proposed a model that considers the "interference factor" which leads to slower growth near the end of transformations. The assumptions in this model include site saturation and diffusion controlled growth. However, as the particle diameter approaches the

interparticle spacing, the diffusion fields interact, leading to hindered growth. Whelan [67] also proposed a model in which the growth rate decreases with time. His model is used to describe the diffusion controlled dissolution of a spherical particle. In this model, the concentration, *C*, is given as a function of time, *t*, and distance, *r*, from a supersaturated particle into the equilibrium matrix by Eq. (7) [68]

$$\Delta C(r,t) = \frac{(C_i - C_e)R}{r} erfc\left(\frac{r-R}{2\sqrt{Dt}}\right) \qquad (7)$$

where C_i and C_e are interface and equilibrium concentration, respectively. The interface concentration is given by the solvus at the given temperature from the phase diagram, *R* is particle radius, *r* is distance from the particle, and *D* is the interdiffusion coefficient. A schematic representation is shown in Figure 5. The solid lines represent the initial state while the dashed lines represent a time *t* after dissolution begins.

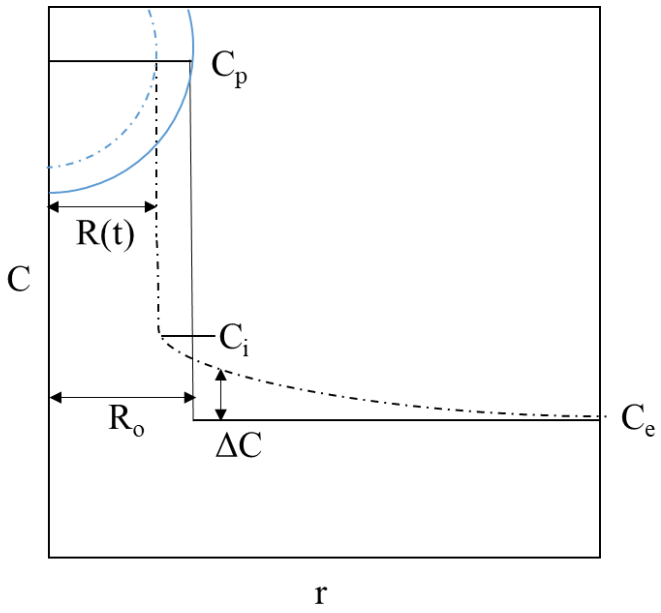

Figure 5. Schematic representation of spherical dissolution, indicating particle concentration (C_p), interface concentration (C_i), matrix/equilibrium concentration (C_e), concentration at a given point (ΔC), initial particle radius (R_o), and particle radius as a function of time ($R(t)$).

The balance of solute flux at the interface and solute lost from the precipitate can be written as Eq. (8)

$$-4\pi R^2\left(C_p - C_i\right)\frac{dR}{dt} = -4\pi R^2 D\left(\frac{\delta \Delta C}{\delta r}\right)_{r=R} \tag{8}$$

where C_p is the solute concentration in the particle. Substituting Eq. (8) into Eq. (7) gives Eq. (9)

$$\frac{dR}{dt} = -\frac{kD}{2R} - \frac{k}{2}\sqrt{\frac{D}{\pi t}} \tag{9}$$

where k is defined by Eq. (10).

$$k = \frac{2(C_i - C_e)}{C_p - C_i} \tag{10}$$

Eq. (9) has no general analytical solution, though a solution can be approximated using only the steady-state portion or regarding the steady-state portion as a constant. Integration of the transient portion of Eq. (9) leads to Eq. (11), which is appropriate for short times as the steady-state part is not treated in this integration. R_i is the initial particle radius.

$$R = R_i - \frac{kDt}{2R_i} - \frac{k}{\sqrt{\pi}}\sqrt{Dt} \tag{11}$$

Zuo *et* al. [69] have suggested an alternative analytical approach to Eq. (9) in which *dR/dt* is separated into 2 parts; r_s and r_t to represent the steady-state and transient parts, respectively, as functions of time. R_s and R_t represent the total contributions of the steady-state and transient portions, respectively. In this case, the steady-state and transient parts are defined by Eq. (12) and Eq. (13), respectively. The total decrement to the radius is thus defined by Eq. (14) and is the sum of the steady-state and transient decrements, per Eq. (15). The total radius dissolved is equivalent to the initial radius of the particle, and is equal to the sum of the steady-state and transient dissolution, per Eq. (16)

$$\frac{dr_s}{dt} = \frac{kD}{2(R_s - r_s)} \tag{12}$$

$$\frac{dr_t}{dt} = \frac{k}{2\sqrt{\pi}}\sqrt{Dt} \tag{13}$$

$$r_d = R_o - R \tag{14}$$

$$r_s + r_t = r_d \tag{15}$$

$$R_s + R_t = R_o \tag{16}$$

where r_d is the total decrement of the radius as a function of time and R_o is the total radius dissolved. If the particles completely dissolve, R_0 is equal to the initial particles radius. With this approach, the individual contributions of the steady-state and transient portions can be approximately integrated to Eq. (17) and Eq. (18), respectively.

$$r_s = R_s - \sqrt{R_s^2 - kDt} \tag{17}$$

$$r_t = \frac{k}{\sqrt{\pi}}\sqrt{Dt} \tag{18}$$

Substituting Eqs. (17) and (18) into Eq. (15) gives a general solution for r_d.

$$r_d = R_s - \sqrt{R_s^2 - kDt} + \frac{k}{\sqrt{\pi}}\sqrt{Dt} \tag{19}$$

However, while R_s can be fitted experimentally, it is not always readily available. For a more readily observable solution, let t_e represent the time for r_d to reach R_o. In this case, Eq. (19) becomes Eq. (20).

$$R_o = R_s - \sqrt{R_s^2 - kDt_e} + \frac{k}{\sqrt{\pi}}\sqrt{Dt_e} \tag{20}$$

From Eq. (15) and Eq. (16), the steady-state and transient contributions can be resolved into Eq. (21) and Eq. (22), respectively, where t_e is defined by Eq. (23). As the definition for R_s in Eq. (21) contains the term R_s, it is better defined by Eq. (24)

$$R_s = R_s - \sqrt{R_s^2 - kDt_e} \tag{21}$$

$$R_t = \frac{k}{\sqrt{\pi}}\sqrt{Dt_e} \tag{22}$$

$$t_e = \frac{R_o^2}{kD\left(1 + \sqrt{\frac{k}{\pi}}\right)^2} \tag{23}$$

$$R_s = \frac{1}{1 + \sqrt{\frac{k}{\pi}}} R_o \tag{24}$$

which leads to the final, generalized approximation for *R* in Eq. (25).

$$R = \sqrt{\frac{k}{\pi}}\left(R_s - \sqrt{kDt}\right) + \sqrt{R_s^2 - kDt} \tag{25}$$

Eq. (25) can be used to provide *R(t)* to calculate V_t, representing transformed volume for a particle, per Eq. (26).

$$V_t = N\frac{4\pi}{3}(R_o^3 - R^3) \tag{26}$$

The extended transformed fraction, x_e, can then be used in Eq. (4) for JMAK analysis, per Eq. (27).

$$x_e = \frac{R_o^3 - R^3}{R_o^3} \tag{27}$$

However, x_e clearly exists exclusively between 0 and 1, leading to a transformed fraction only between 0 and $1\text{-}e^{-1}$ per Eq. (4). As such, the transformed fraction is proportionally modified, along with the time, to exist from 0 to 1 using time-scaling. Scaled variables are denoted with subscript *m*. The resulting expressions for modified time and modified transformed fraction are

$$m = \frac{1}{1 - e^{-1}} \tag{28}$$

$$t_m = mt \tag{29}$$

$$f_{tm} = mf_t = m(1 - e^{-x_e}) \tag{30}$$

The approach proposed by Zuo *et* al. [69] has exhibited good agreement with experimental data [70, 71].

In some alloy systems, discontinuous precipitation and dissolution has led to grain refinement, suggesting that thermal cycles may be designed to induce recrystallization [52, 72, 73]. However, this phenomenon has not been investigated in the U-Mo system. Grain growth literature in γ-U(Mo) solid solution is limited, though coarsening has been observed during fabrication [37, 74, 75]. The grain growth in γ-U solid solution alloys has been described using Eq. (31), proposed by Beck *et* al. [76-78],

$$D(t)^n - D_o^n = Kt \tag{31}$$

where *D(t)* is grain size as a function of time, D_o is initial grain size, *t* is time, *n* is the grain growth exponent, and *K* is the grain growth coefficient, where *n* is typically ~2 for normal growth and *K* follows an Arrhenius relationship with temperature, described by Eq. (32)

$$K = K_o e^{\frac{-Q}{k_B T}} \tag{32}$$

where K_o is the pre-exponential factor, *Q* is activation energy, k_B is the Boltzmann constant, and *T* is temperature. In γ-U-Mo alloys, the pre-exponential has been reported ranging from 7.66 x 10^6 to 4.63 x 10^{10} $\mu m^2/s$ and the activation energy ranging from 172 to 272 kJ/mol [79, 80]. Understanding grain growth phenomenon following decomposition and γ reversion can provide insight into how fabrication of the fuel plates affects the grain structure, and subsequently, irradiative swelling.

2.4 Fuel Plate Fabrication

The U10Mo fuel is first fabricated by arc melting. Enrichment facilities provide high purity HEU, so it must first be down-blended with naturally occurring uranium which contains only about 7 at. % fissile isotopes [81]. The mixture is then arc melted with 10 wt. % Mo, flipping and re-melting several times to promote homogeneity. The alloy coupon is then filed to remove sharp edges and chemically cleaned in a solution of water and nitric acid before encapsulating the foil in the AA6061 cladding [82].

The hot isostatic press (HIP) process was developed by Battelle Memorial Institute in order to generate diffusion bonding between nuclear fuel elements [15, 83, 84]. HIP relies on elevated temperature and pressure to consolidate material and can produce high density isotropic parts. The HIP process for monolithic fuels was first used with U-Mo alloys varying from 7 to 12 wt. % in AA6061 cladding [15]. Good bonding was reported after 90 minutes at 560°C and 104 MPa, however, significant growth of the interaction layer between the fuel and cladding was observed. A Zr diffusion barrier was proposed [13, 14] and co-rolled with the fuel foil in a stainless steel can prior to HIP, which resulted in an interaction layer of only 1-2 μm after HIP. The co-rolling procedure includes 20 to 30 hot-rolling passes at 650°C to reduce the thickness of the U10Mo/Zr coupons, after which the stainless steel hot-rolling can is sheared off and the coupon undergoes cold-rolling to promote adhesion. A schematic illustrating the overall fabrication process is shown in Figure 6.

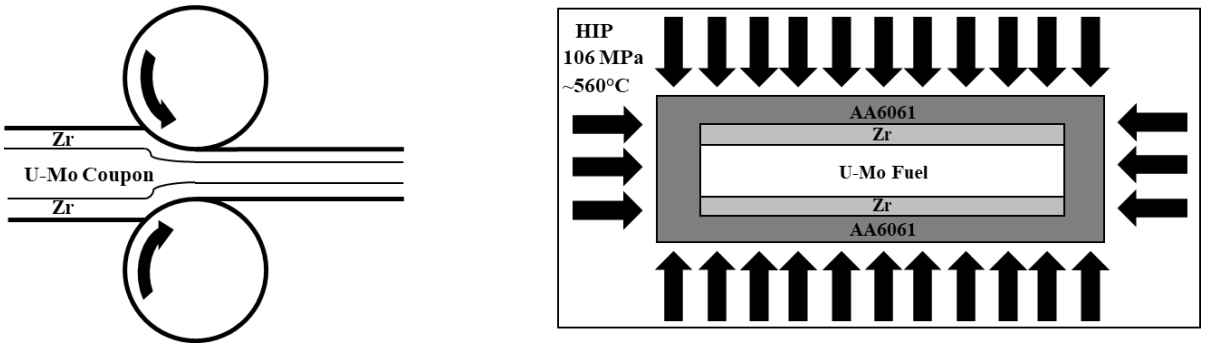

Figure 6. Schematic illustration of the co-rolling and HIP operations typically used in fabricating monolithic fuel plates.

Per the binary U-Mo phase diagram, shown in Figure 3, the equilibrium structure of U-Mo alloys at room temperature is α+γ' [85], suggesting that with sufficient time, the γ phase will decompose. Time-temperature-transformation (T-T-T) diagrams indicate that the transformation is hindered by the addition of Mo [30-32, 86] and processing techniques must be optimized to minimize decomposition. The rolling and HIP processes are performed at or above the eutectoid temperature, but some decomposed regions have been observed in the fuel plates after fabrication [16]. It was later determined that the extent of decomposition did not increase with increased hold time at 560°C during HIP, but increased when the HIP temperature was lowered to 540 or 520°C. Decreased ramping/cooling rate also resulted in further decomposition during HIP [87]. HIP was conducted at 580°C for 1.5 h and the extent of decomposition did not dramatically change, suggesting that the fuel decomposed mostly during cooling. Prolonged hold times at elevated temperatures (>560°C) led to a reduction in the amount of decomposition but the interaction layers between the diffusion barrier, fuel, and cladding experienced rapid growth as a result. The HIP time and temperature were thus selected as 1.5 h and 560°C, respectively [87, 88].

2.5 LEU Monolithic Fuel Plate Characterization Studies

Section 2.5 was originally published in *Defect and Diffusion Forum.* Newell, R., Mehta, A., Park, Y. J., Keiser Jr, D. D., & Sohn, Y. H. (2017). Interdiffusion, reactions, and phase transformations observed during fabrication of low enriched uranium monolithic fuel system for research and test reactors. *Defect and Diffusion Forum,* vol. 383, pp. 10-16. *[89]*.

2.5.1 γ-U10Mo Decomposition.

The U10Mo alloy serves as the fuel; its behavior is paramount to irradiation performance. The desired microstructure of the alloy consists of only metastable γ solid solution. Consequently, various alloy and fuel plate characterization studies have been conducted to investigate the stability of the γ phase. Initial kinetic studies of U-Mo alloy transformations were aimed at generating reliable time-temperature-transformation (T-T-T) diagrams [30-32]. Using information from the T-T-T diagrams, the initial fabrication procedure was tailored to retain the stability of γ. Following initial fabrication, several parameters could be isolated and investigated for their independent effects on γ-phase retention. The variables in the HIP process include holding temperature, holding time, and ramping/cooling rate. The relationships between each variable and the kinetics of γ decomposition were investigated by Park *et* al. [87] using fuel plates fabricated with varying values for each parameter. It was found that as ramping/cooling rate increased, the extent of decomposition decreased. Additionally, as holding time increased (at a constant temperature of 560°C), the extent of decomposition remained unchanged. Finally, as holding temperature increased, the extent of decomposition decreased, however, the increased temperature resulted in increased growth of $(Al,Si)_3Zr$ between the diffusion barrier and cladding.

Though the extent of transformation changed with holding temperature and ramping/cooling rate, the characteristic mechanism did not; the transformation from γ to α+γ' originated at grain boundaries and penetrated into the γ matrix via lamellar growth. Jue *et* al. [16] also observed lamellar decomposition at the grain boundaries but reported additional decomposed areas over 100 μm in length along the rolling direction. The elongated decomposed areas may correspond to low Mo regions that resulted from chemical banding along the rolling direction; per the T-T-T diagram, lower Mo concentration promotes accelerated decomposition of the γ phase. The banding may be a result of using inhomogeneous as-cast ingots in rolling.

The effects of post-rolling heat treatments were analyzed by Jue *et* al. [90], and it was found that the homogeneity of the U10Mo fuel increased with respect to composition as annealing temperature increased, i.e. the extent of chemical banding decreased. Additionally, the fuel experienced increased grain growth with increased heat treatment temperature, and the grain morphology transitioned from elongated to equiaxed. However, excessive growth of the U10Mo/Zr interaction layer was observed with post-rolling heat treatment. Homogenization heat treatment at 1000°C prior to rolling also led to reduced variation in Mo content throughout the fuel but was not reported to have any effect on grain size and morphology after rolling [90].

Several carbides and oxides have also been observed in the U10Mo fuel [16, 87, 91]. These inclusions have not been reported to affect the overall decomposition of γ-U10Mo but may have some deleterious effects on fuel integrity due to distinct differences in mechanical properties. The inclusions are assumed to originate during the casting process [92, 93] and the quantity observed in the fuel did not change after HIP. The UC and UO_2 inclusions constituted about 1.5 vol. % of the fuel alloy [91] and are highlighted in Figure 7.

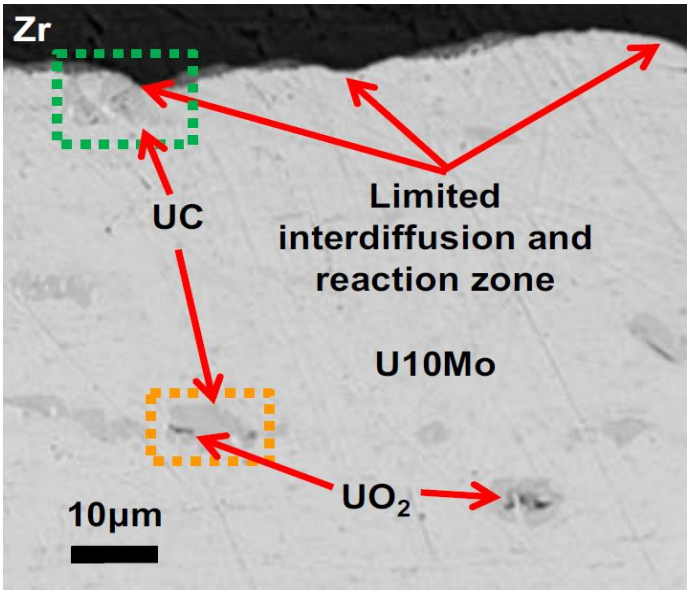

Figure 7. Anomalous microstructure showing UC and UO_2 inclusions in U10Mo alloy (orange box), as well as UC and limited interdiffusion regions near the U10Mo/Zr interface (green box).

2.5.2 Interdiffusion and Reactions with U10Mo Fuel.

In monolithic fuel plates, the U10Mo fuel is in direct contact with the Zr diffusion barrier on its top and bottom surfaces, and with the AA6061 cladding around its uncoated edges. These areas are subject to metallurgical interactions during rolling and HIP operations. The interaction between U10Mo and Zr is expected to be limited, because Zr was selected as a potential diffusion barrier in part due to its sluggish interaction with U10Mo [13, 14]. The rate of reaction was studied with a series of diffusion couples [13, 14] and the growth rate of the interaction layer between U10Mo and Zr was found to be 10^3 times lower than that of U10Mo and Al in diffusion couples. Perez *et* al. [94] characterized the interaction between U10Mo and Zr in HIP plates, and identified a 2 μm layer of UZr_2, a 0.5 μm 2-phase region of γ-U solid solution and UZr_2, a 50 nm layer of Zr, and a layer of Mo_2Zr that ranged from a few nm to 250 nm, resulting in a total thickness of

about 3-4 μm. The total thickness of the interaction layer reported by Jue *et* al. [16] was slightly less at roughly 1 μm.

Fission gas bubbles have been observed to coalesce at the interface during irradiation, resulting in porosity, swelling, and eventually delamination at very high fission density (9.5×10^{21} fissions/cm^3) [25]. So, the interaction between U10Mo and Zr should be relatively limited and homogeneous. However, some anomalous features have been observed at the interface [91]. Inclusions similar to those observed in the U10Mo matrix were also observed near the U10Mo/Zr interface, including UC and UO_2 as well as some areas of limited interaction. The inclusions were not observed to change with time or temperature, though the areas of limited interaction were observed to decrease with increased HIP temperature.

Park *et* al. [88] analyzed the growth of the U10Mo/Zr interaction layer with respect to changes in holding time and temperature during the HIP process, and found that the thickness did not significantly change with temperature up to 580°C up to 90 minutes or with hold time up to 345 minutes at 560°C. Jue *et* al. [90] performed a series of post-rolling heat treatments (without HIP), and the thickness of the interaction layer between U10Mo and Zr increased to 3.2 μm after 1 h at 650°C and to 27.1 μm after 1 h at 850°C.

Though the diffusion barrier was implemented to minimize contact between the U10Mo and AA6061, these materials still interact at the uncoated edges of the U10Mo fuel. Evidence from post-irradiation examinations [95, 96] and diffusion couple studies [97, 98] indicate that the interface between fuel and cladding is weak and prone to cracking. Prior to the application of a diffusion barrier, this interaction was extensive and promoted fission gas bubble coalescence at the interface, leading to delamination at an average fission density of only 2.4×10^{21} fissions/cm^3

[95]. In monolithic HIP plates using Zr diffusion barriers, the uncoated U10Mo/AA6061 interfaces did not undergo substantial interaction during fabrication [16].

2.5.3 Interdiffusion and Reactions with AA6061 Cladding.

The contact between the Zr diffusion barrier and AA6061 cladding also experiences metallurgical interaction during HIP. This area was investigated by Perez *et* al. [99], in which four layers were identified between the cladding and diffusion barrier: $(Al,Si)_2Zr$, $(Al,Si)Zr_3$, $(Al,Si)_3Zr$, and $AlSi_4Zr_5$. The thickness of the interaction layer was reported as less than 1-2 μm, corroborated by Jue *et* al. [16] and Park *et* al. [88]. However, with HIP hold temperature increased to 580°C, the length of the interaction increased to above 2 μm after 90 minutes. The thickness increased to a lesser extent with increased holding time at 560°C [88].

2.6 Irradiation Behavior

Following fabrication, the fuel plates are placed into high-power reactors and irradiated. High-power reactors can reach up to 10^{22} fissions/cm^3 and typically operate around 150 to 300°C [100]. Per the phase diagram shown in Figure 3, the equilibrium microstructure of U10Mo is α+γ'. However, low temperature irradiation has been shown to induce a phase transformation from α+γ' to γ via irradiation-induced diffusion given sufficient fission rate [101-104]. The irradiation-induced diffusion coefficient, D_R, is defined as a function of the fission rate, *Bu*, by Eq. (33), where $(D_R)_1$ and $(Bu)_1$ are constants with values of 1.14 x 10^{-18} cm^2/s and 5.25 x 10^{12} fission/cm^3-s, respectively, for a U-9 wt. % Mo alloy [103].

$$D_R = \frac{(D_R)_1}{(Bu)_1} Bu \tag{33}$$

The thermally induced diffusion coefficient is well defined as a function of temperature per the Arrhenius relationship and is described using Eq. (34). The pre-exponential factor D_O and activation energy Q for interdiffusion in U10Mo are 0.77 x 10^{-2} cm^2/s and 182 kJ, respectively [105]. R is the ideal gas constant, and T is absolute temperature.

$$D_T = D_o \exp\left(-\frac{Q}{RT}\right) \tag{34}$$

If the thermal and irradiation-induced diffusion coefficients are set equal to one another such that no phase transformation occurs, the critical fission rate can be solved as a function of temperature for the U10Mo alloy. The relationship is shown in Eq. (35).

$$Bu = \frac{(Bu)_1}{(D_R)_1} * D_o \exp\left(-\frac{Q}{RT}\right) \tag{35}$$

At a given temperature, if the fission rate is above the critical value, radiation-induced diffusion dominates (i.e. $D_R > D_T$) and the alloy tends to transform to γ, while if the fission rate is below that critical value, thermally-induced diffusion dominates (i.e. $D_T > D_R$) and the alloy tends to transform to α+γ'. This concept is shown graphically in Figure 8. The critical fission rate is shown as a function of temperature via the blue line. If the irradiation conditions are above that line, the α+γ' to γ transformation can be expected, while if the conditions fall below the critical fission rate, the fuel can be expected to decompose from γ to α+γ'.

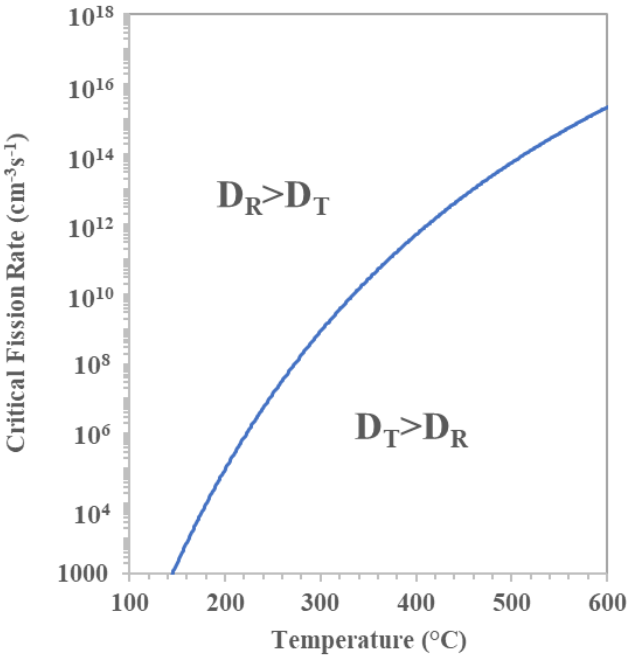

Figure 8. Critical fission rate as a function of temperature for U-9 wt. % Mo alloy.

Understanding the microstructure of the fuel prior to irradiation is critical to predicting its irradiation behavior in terms of swelling. As described in previous sections, decomposed α+γ' can exhibit unpredictable and anisotropic swelling, while irradiation of the γ phase results in predictable and isotropic behavior. In fact, the swelling of a fuel consisting completely of the γ phase can be modeled by considering the accommodation of fission gases within the fuel [106]. The gas atoms that result from fission of U atoms can be stored within the fuel in a variety of ways: (1) in solution within the γ lattice, (2) in a network of bubbles within the γ grains, termed intragranular gas bubbles, or (3) in coalesced bubbles along the γ grain boundaries, termed intergranular gas bubbles. The overall swelling of the fuel plate can be considered as the sum of these three modes of swelling [107], which is described using Eq. (36).

$$\frac{\Delta V}{V} = \frac{c_g a^3}{4} + \frac{4\pi}{3}\left(r_b^3 c_b + R_b^2 C_b^2 \frac{6}{d_g}\right) \qquad (36)$$

In Eq. (36), $\Delta V/V$ represents the volume change due to swelling. The first term on the right side of the equation represents swelling due to gas bubbles in solution, where c_g and a are the concentration of fission gas atoms and the lattice parameter of the fuel, respectively. The two terms in the parentheses represent the swelling due to intra- and intergranular fission gas bubbles; r_b and c_b are radius and concentration of intragranular gas bubbles, respectively, while R_b, C_b, and d_g are the radius of intergranular bubbles, concentration of intergranular bubbles, and diameter of γ grains, respectively. The size and concentration of the gas bubbles has been investigated and modeled as a function of irradiation time, temperature, and fission rate [107]. Evident from Eq. (36), the γ grain size plays an important role in the overall swelling of the fuel plates. However, there is a lack of literature reporting how the grain size and morphology are affected by processing of U-Mo alloys. More specifically, there is an absence of investigation into how γ decomposition and subsequent reversion changes the grain distribution and microstructure in the reformed γ phase.

2.7 Modeling and Simulation of LEU Monolithic Plates

The behavior of a fuel plate during operation is a product of the behavior of its constituents and efforts are ongoing to predictively model and simulate fuel plate behavior throughout fabrication and irradiation. Beginning with fabrication, the thermo-mechanical response to HIP has been analyzed as it relates to the cooling rate of the fuel plates following HIP, but without regard to the Zr diffusion barrier or the interfacial phases that result from metallurgical interactions during fabrication [108]. Furthermore, simulation has been carried out to investigate the response of HIP-bonded fuel plate assemblies to elevated temperature, evaluating the thermo-mechanical response after fabrication using finite element analysis [109]. However, the authors of the studies

state that the reliability of the modeled behavior is dependent on the availability and accuracy of mechanical property data, which is scarce [109]. Further development of accurate mechanical property data could be used to improve modeling and simulation of rolling [110, 111], HIP, and irradiation [112] leading to improvements in the fabrication and performance of LEU monolithic fuel plates.

CHAPTER 3: EXPERIMENTAL DETAILS

3.1 Material Procurement and Preparation

All the uranium used in this study was depleted. Prototypic fuel plates were fabricated using depleted uranium (DU) and experimental Zr diffusion barriers. The plates were received at UCF labeled with a series of alphanumeric identifiers, i.e., DUM9XX. DUM911, DUM912, DUM913, and DUM914 have EP Zr diffusion barriers. The electrolyte solution for plating Zr is a molten salt bath, typically containing ZrF_4, LiF, and NaF, and the process is described in further detail by Coffey *et* al. [113]. DUM915 and DUM916 contain PS diffusion barriers. The fabrication process is detailed by Cummins *et* al. [114]. DUM926, DUM927, DUM941, and DUM942 contain RB diffusion barriers, and have been fabricated per the conventional co-rolled fuel plate fabrication process [15]. Following Zr diffusion barrier application, all fuel plates were clad in AA6061 via HIP. The fuel plates were then mounted, sectioned, and polished for metallographic examination.

The DU and DU alloys for the remaining studies were arc melted at Idaho National Laboratory and shipped to the University of Central Florida. Any other material (diffusion couple metals, consumables, etc.) was purchased from commercial vendors. The metals were supplied as rods which were sectioned into disks using a low speed diamond saw and subjected to various heat treatments (described in the following section). The disks were polished using 400, 600, 800, and 1200 grit silicon carbide polishing pads, followed by woven polishing pads impregnated with 6, 3, and 1 μm diamond paste. The final polishing was done with 0.04 μm colloidal silica solution. Following these polishing steps, the disks were scratch-free and ready for imaging.

Disks for diffusion couple experiments were also sectioned then polished using 400, 600, 800, and 1200 grit silicon carbide grinding pads. After grinding, the disks were clamped together in stainless steel jigs using three screws. Alumina spacers were placed between the disks and jigs to prevent contamination from the jigs. An illustration of a diffusion couple assembled in a jig is shown in Figure 9. The diffusion couple systems were selected based on relevance to the monolithic fuel system; intermetallic compounds and solid solutions not readily available for indentation in HIP plates were intentionally fabricated in diffusion couples for nanoindentation. The selected systems include Al-Zr, U-Zr, U10Mo-Zr, and U-Mo solid solution. Following fabrication of the diffusion couples, they were sealed in evacuated quartz tubes along with Ta foil as an oxygen getter, as shown in Figure 10, and heat treated. After the diffusion couples were heat treated, they were mounted using epoxy, cross-sectioned, and polished for examination.

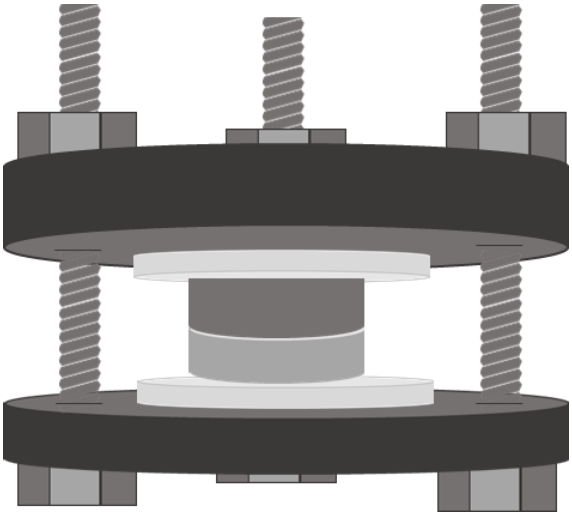

Figure 9. Schematic illustration of diffusion couple setup.

Figure 10. Assembled diffusion couple sealed in evacuated quartz tube.

3.2 Heat Treatments

After the U10Mo alloy rods were received, they were homogenized in a tube furnace at 800°C for 96 hours. The homogenized rods were then sectioned using a diamond saw. The sectioned disks were then used for either recrystallization heat treatments or diffusion couples. For isothermal phase transformation experiments, the disks were decomposed from γ to α+γ' at 500°C. For γ reversion experiments, decomposed disks were then isothermally annealed at 570, 580, or 590°C. The γ grain growth experiments were done at higher temperatures (600, 650, 700°C) to promote accelerated grain growth.

In diffusion couple experiments, heat treatment times and temperatures are typically determined based on known kinetics from literature. For diffusion-controlled growth of an interaction layer in a diffusion couple, the growth rate is described using the parabolic growth constant. Published parabolic growth constants are used to estimate the length of the layer according to the prescribed annealing times and temperatures. The desired length of the interaction layer in a diffusion couple should be large enough for EDS and indentation analysis, (i.e. >~5 μm),

but not large enough to potentially interfere with the assumed infinite-infinite boundary conditions. The phases that were indented in fuel plates and diffusion couples are shown with their fabrication conditions in Table 1.

For all heat treatments, the samples were placed inside quartz tubes which were then sealed using a propane torch. The sealed capsule was then evacuated to 2×10^{-5} torr or better. The vacuum sealed capsule was placed in the furnace for the heat treatment, after which the sample was cooled by immediately immersing in water and breaking the capsule (quenching), removing from the furnace and allowing to cool in air (air cooling), or turning off the furnace and allowing the sample to cool inside (furnace cooling).

Table 1. Experimental matrix for indentation of phases relevant to monolithic fuel plates

Phases	**Sample type**	**Description**	**References**
$(Al,Si)_3Zr$	HIP fuel plate	HIP'ed at 560ºC for 3 hours	[88]
Al_3Zr	Diffusion couple	Al vs. Zr annealed at 425ºC for 720 hours	This study
UZr_2	Diffusion couple	U vs. Zr annealed at 580ºC for 360 hours	This study
Mo_2Zr	Diffusion couple	U10Mo vs. Zr annealed at 800ºC for 480 hours	[13]
α-U	Diffusion couple	U vs. Zr annealed at 580ºC for 360 hours	This study
γ-U(Mo)	Diffusion couple	U vs. Mo annealed at 1000ºC for 24 hours	[105]
γ-U(Mo)	Diffusion couple	U vs. U10Mo annealed at 1000ºC for 96 hours	This study
UC	HIP fuel plate	HIP'ed at 560ºC for 3 hours	[88]

3.3 Crystal Structure and Microstructure Characterization

3.3.1 Microscopy and Image Analysis

Sample microstructures were examined using a 30 keV scanning electron microscope (SEM), equipped with backscatter electron (BSE), secondary electron (SE), and x-ray detectors. The x-ray detector was used for x-ray energy dispersive spectroscopy (EDS) for semi-quantitative compositional analysis, including point-and-shoot, area, and line scans. For finer features, a 300 keV transmission electron microscope (TEM) was used. The TEM is also equipped with an EDS detector and can provide crystal structure information via selected area electron diffraction (SAED). Samples for TEM were prepared with a 30 keV focused ion beam (FIB) using the in situ lift out technique, by which a small wedge of sample is removed from the area of interest and welded to a copper grid for TEM examination.

Optical microscopy was used for imaging fuel plates and heat treated disks. For the fuel plates, bright-field images were taken along the length of the sample and stitched together to form overall images of the entire fuel plates. The scale of the images was calibrated using a calibration slide and the Motic software supplied with the camera. Following calibration, the thickness of the Zr diffusion barriers was measured at roughly 450 μm intervals. Following the measurements along the entire fuel plate, average thickness and standard deviation was calculated for the Zr diffusion barrier of each fuel plate. A sample image with Zr barrier thickness measurement is shown in Figure 11.

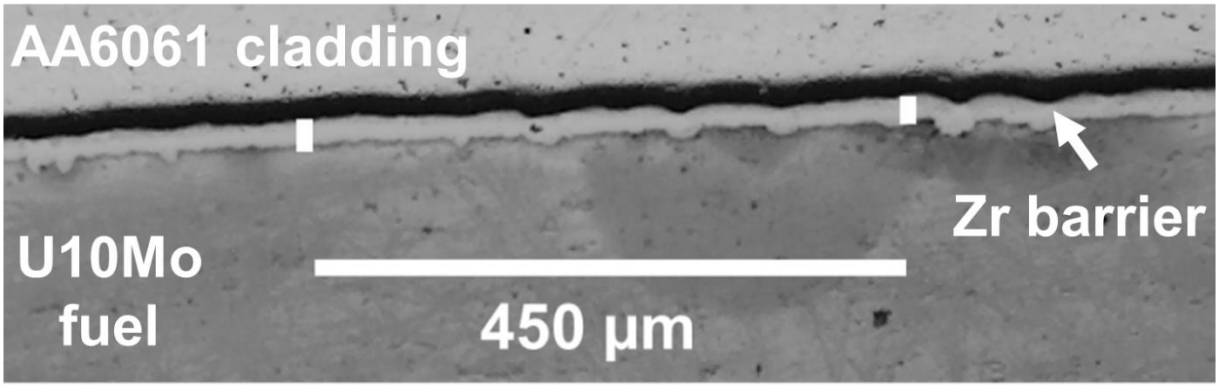

Figure 11. Sample micrograph with Zr diffusion barrier thickness measurement performed on DUM913.

The standard deviation, however, does not best represent the uniformity of the diffusion barrier thickness; the values are dominated by average thickness. Instead, the squared coefficient of variance (CV^2) is used to represent the uniformity of the diffusion barrier thickness, as it represents a normalized variance accounting for the average. The CV^2 is defined by Eq. (37).

$$CV^2 = \left(\frac{standard\ deviation}{average\ thickness}\right)^2 \tag{37}$$

Optical microscopy was also employed to analyze the grain size of heat treated U10Mo disks. Immediately following polishing, the disks are highly reflective and uniform, absent of any orientation-based contrast. However, after ~48 h exposure to ambient conditions, the grains oxidize and contrast develops when viewed using a polarizing filter. The grain size was then analyzed using the procedure outlined in ASTM Standard E112 [115]. The resulting average grain size represents the observed diameter on a two-dimensional cross-section rather than the true average grain diameter in three dimensions. As a result, the measured diameter can be multiplied by a proportionality constant of 1.78 to more accurately represent three-dimensional tetrakaidekahedral grains [116, 117].

3.3.2 X-ray Diffraction

The crystal structure of samples was analyzed using x-ray diffraction (XRD) with voltage and current of 45 keV and 40 mA, respectively. The diffractometer uses a copper source with a characteristic x-ray wavelength of 1.54 Å. The scan was performed with a step size of 0.033° and a 2θ range of 30 to 120°. The dwell time was selected to allow over 10000 counts to collect at the highest intensity peak. The patterns were then analyzed using HighScore Xpert Plus software. The patterns obtained from disks containing α, γ, and γ' were deconvoluted using the built-in peak identification and fitting tools. The peaks were able to be manually identified using the peak locations from the JCPDS database for α and γ', and experimental data from homogenized γ-U10Mo. The reference peaks are shown in Figure 12. The peak fitting tool was then used to refine the simulated peak shapes and intensities until they coincided with the experimental data. The scan for a single phase could then be simulated using only its respective peaks. Using relative intensities of the highest intensity peaks, the amount of each phase could then be estimated.

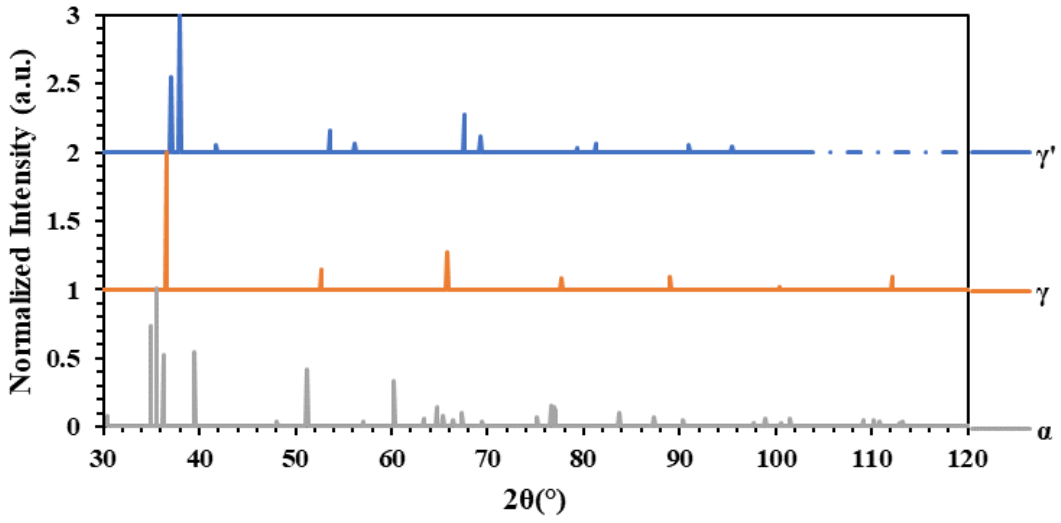

Figure 12. Reference patterns for constituent phases in decomposed and recrystallized U10Mo disks. The dotted line in the γ' pattern indicates no data available above 105°.

In some instances, phases and features of interest exist on small scales and their crystal structure must be investigated using SAED. Using this technique, local crystal structures can be identified by the diffraction of the electron beam in TEM. The resulting pattern can be indexed and compared with powder diffraction files to accurately identify the lattice structure and spacing [118].

3.4 Nanoindentation Technique

Mechanical assessment was performed using a nanoindenter equipped with a Berkovich tip. The indentation was performed under constant-loading conditions, with a peak load of 8000 μN. The loading and unloading curves were then analyzed using Oliver and Pharr's method [119, 120] to determine reduced modulus and hardness. Accordingly, the hardness is dependent on the area function and peak load based on the relationship in Eq. (38)

$$H = \frac{P}{A_C} \tag{38}$$

where H, P and A_c refer to, respectively, hardness, peak load, and contact area, which is a function of the contact depth. Reduced modulus is dependent upon the initial slope of the unloading curve and the contact area, as expressed by Eq. (39)

$$E_r = \frac{\sqrt{\pi}}{2}\frac{S}{A_C} \tag{39}$$

where E_r is the reduced modulus and S refers to the initial slope of the unloading curve. The reduced modulus can then be used to calculate the elastic modulus per relationship in Eq. (40)

$$\frac{1}{E_r} = \frac{1-\nu_i^2}{E_i} + \frac{1-\nu_s^2}{E_s} \tag{40}$$

where E_r is reduced modulus of the sample, E_i and E_s are elastic modulus of the indenter and sample, respectively, and ν_i and ν_s are Poisson's ratio of the indenter and sample, respectively. For a diamond indenter tip, ν_i and E_i are 0.07 and 1140 GPa, respectively.

Prior to indentation testing, the area function was calibrated by performing 100 indents on a fused quartz standard with loads varying from 100 to 10,000 μN in 100 μN increments. With known values for reduced modulus and hardness, the constants in the polynomial area function in Eq. (41) could be tuned to accurately describe the contact area resulting from the tip used in this study.

$$A_C = C_O h_c^2 + C_1 h_c + C_2 h_c^{\frac{1}{2}} + C_3 h_c^{\frac{1}{4}} + C_4 h_c^{\frac{1}{8}} \qquad (41)$$

Subsequently, the electrostatic transducer constants were tuned by performing an indentation axis calibration indent in air. Indentation arrays were then systematically arranged to indent points of specific composition with statistical confidence. For compositions that exist in large, continuous quantities, >50 indents were performed. On phases with varying composition, arrays were designed to collect data as a function of composition. As such, an indentation array was typically composed of N x 5 indents, where N represents the number of discrete compositions examined. After indentation arrays were performed, erroneous points (indents on inclusions, erroneous data due to excessive noise) were removed from statistical analyses.

CHAPTER 4: ZIRCONIUM DIFFUSION BARRIER MICROSTRUCTURES

The fuel plates received at UCF we examined via SEM and general microstructures of each diffusion barrier are shown in the BSE micrographs in Figure 13. Major differences in the samples are diffusion barrier thickness and thickness variation, inclusions, porosity, cracking, interface microstructure, and fuel microstructure. The fuel exhibits some chemical inhomogeneity and elongated grains in DUM926, DUM927, DUM941, and DUM942, but none in the remaining samples. The BSE micrographs in Figure 14 show the fuel region in samples DUM915 and DUM941 and are representative of the remaining samples. The banded regions of high and low brightness in DUM941 indicate inhomogeneous composition along the rolling direction, leading to localized decomposition in bands relatively lean in Mo. The rolling process also leads to elongated grains, resulting in the carbide and oxide stringers observed along the rolling direction. The fuel in DUM915 exhibits no inhomogeneity and the carbides and oxides appear distributed along the equiaxed grain boundaries and the fuel in the remaining EP and PS samples exhibit similar microstructure. The remaining differences are described in more detail in the following sections.

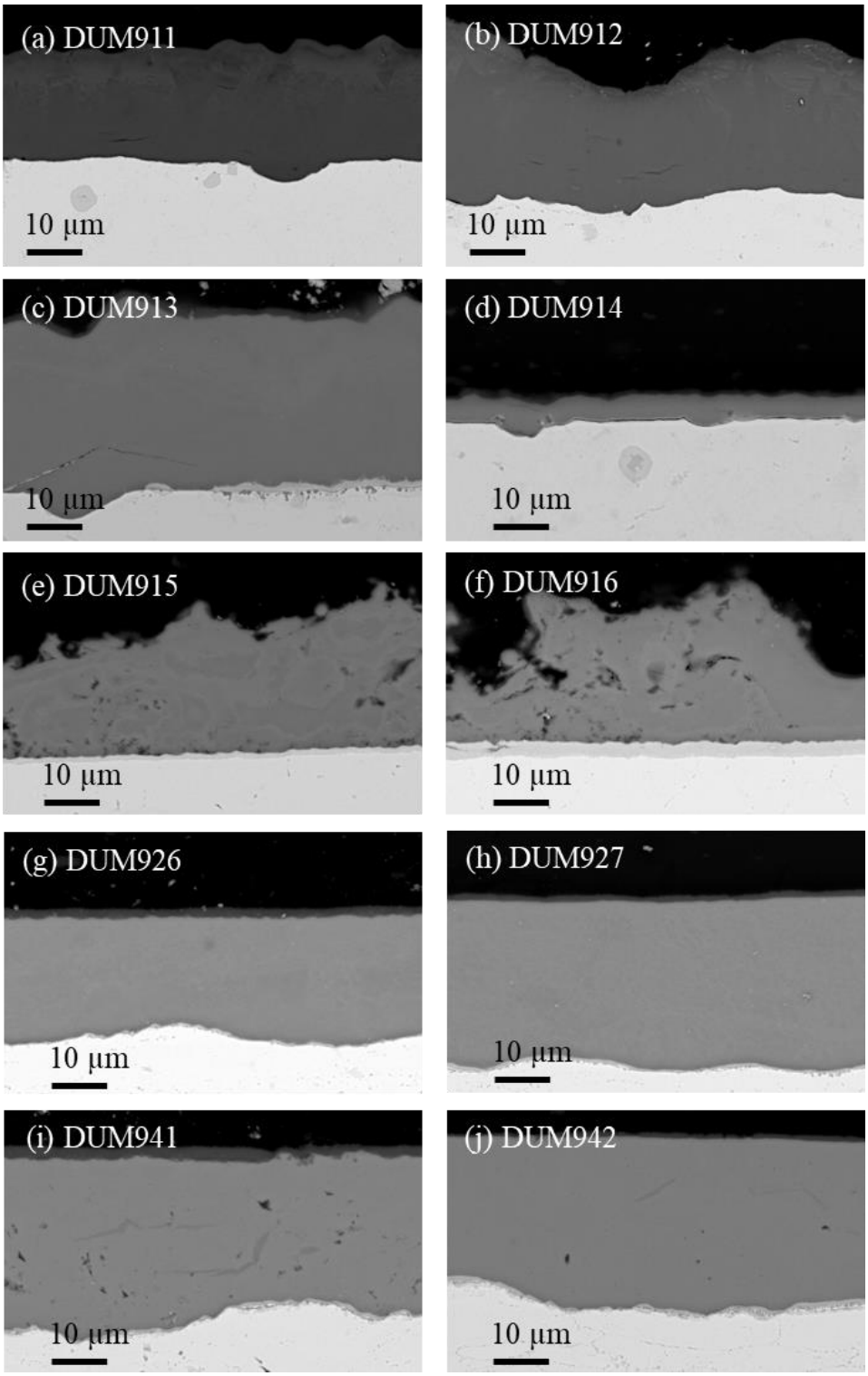

Figure 13. BSE micrographs showing the general microstructure of each diffusion barrier examined in this study.

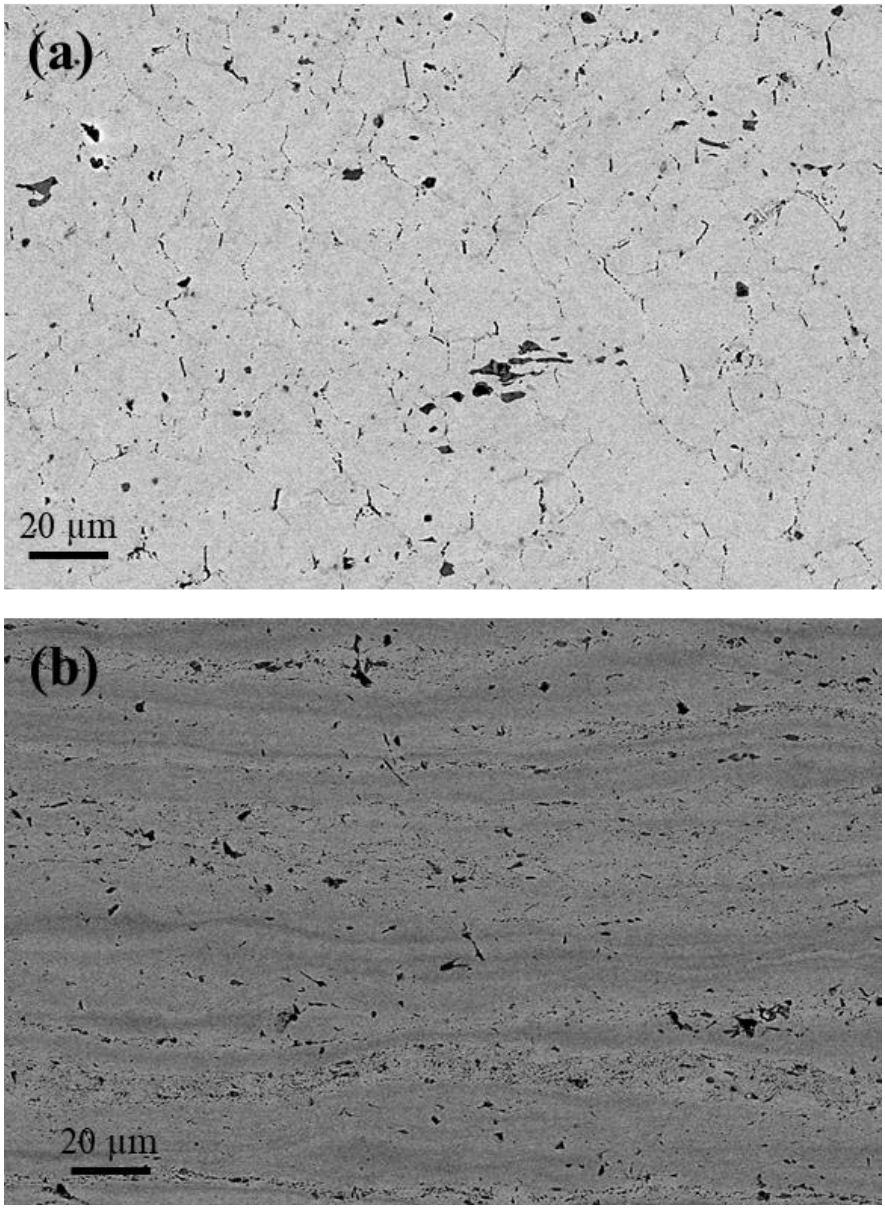

Figure 14. BSE micrograph showing (a) homogeneous and (b) inhomogeneous fuel microstructure in DUM915 and DUM941, respectively.

The thickness of each sample was measured and is shown in Figure 15a with error bars representing standard deviation. The thicknesses of the PS and RB diffusion barriers closely resemble the nominal thickness of 25 µm, while the EP samples exhibit generally lower thickness. Figure 15a also shows that the CV^2 of the RB samples are relatively low in comparison to the

remaining samples (EP and PS), indicating more uniform thickness. In DUM914, the EP process led to a thin diffusion barrier that ultimately delaminated along the majority of the fuel-barrier interface, as shown in Figure 16. The delamination may have occurred during the cutting operation prior to mounting the sample for examination but is regardless indicative of a weakly bonded interface in comparison to the remaining samples.

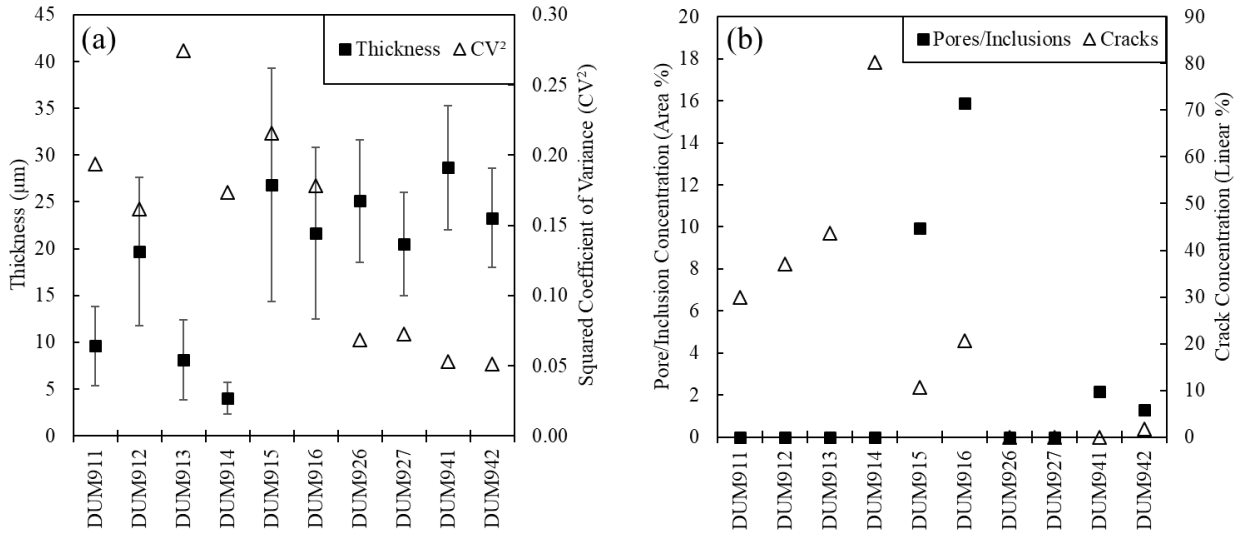

Figure 15. (a) Average thickness and thickness CV^2 and (b) concentrations of defects (inclusions and porosity) and cracks in Zr diffusion barriers.

Figure 16. Optical micrograph showing delamination along the fuel-barrier interface in DUM914.

The percentages of the diffusion barriers containing porosity and inclusions were measured and are shown in Figure 15b. Only samples DUM915 and DUM916 exhibited significant porosity, and they also exhibited the highest concentration of distinguishable inclusions. Based on the EDS

maps in Figure 17, the major inclusions are large regions of U and Mo enrichment, which are evident throughout the length of the barriers.

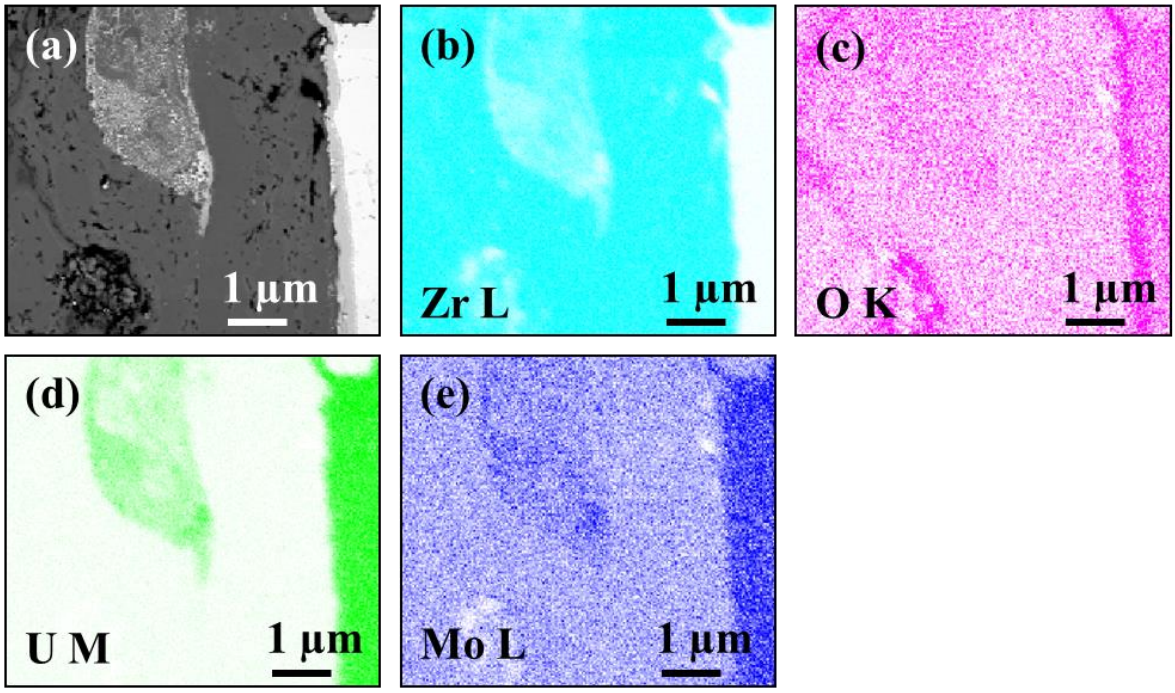

Figure 17. (a) BSE micrograph and corresponding elemental maps for (b) Zr, (c) O, (d) U, and (e) Mo, demonstrating U and Mo enrichment at the inclusion in the DUM 916 diffusion barrier.

As these inclusions were not reported prior to AA6061 cladding [17], they are assumed to form as a result of the HIP operation. In the as-sprayed condition, the diffusion barriers in the mounted samples contained porosity that was filled with epoxy and thus assumed interconnected. During HIP, the closure of these pores must occur via transport of the surrounding material as a result of the elevated temperature and pressure. The inclusion of fissile material within the diffusion barrier could give rise to mechanical instability as a result of radiative swelling outside of the constrained fuel foil and should be taken into consideration when evaluating the PS process for Zr diffusion barriers.

Several inclusions were also observed in DUM941 and DUM942, an example of which can be seen in the BSE micrograph in Figure 18a. These inclusions did not exhibit any detectable composition difference with SEM EDS analysis and were thus investigated using TEM. The TEM bright-field micrograph in Figure 18b shows the area outlined in Figure 18a, and SAED patterns were taken from the matrix (M) and inclusion (I) phases. Figure 18c and d show the SAED patterns corresponding to the α-Zr matrix (M) and δ-$ZrH_{1.5}$ [121] inclusion (I), respectively.

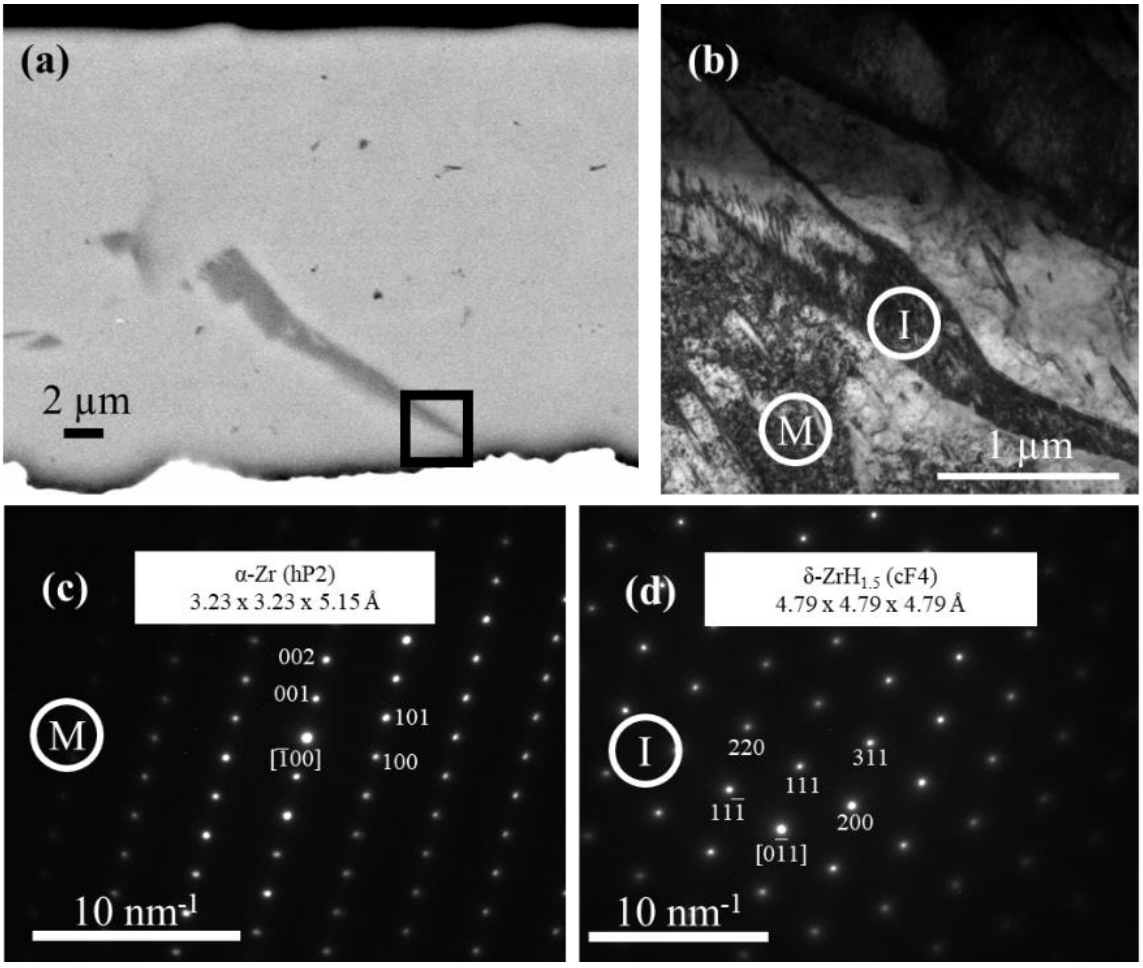

Figure 18. (a) BSE micrograph showing inclusion in DUM941 Zr barrier. The black rectangle indicates the area taken for the (b) bright-field TEM micrograph of the barrier and inclusion. (M) and (I) indicate the areas selected for SAED of the (c) Zr matrix and (d) $ZrH_{1.5}$ inclusion, respectively.

Cracking was primarily observed in samples with EP diffusion barriers (DUM911, DUM912, DUM913, and DUM914) and was minimal in the remaining samples. The extent of cracking in all samples is shown on the secondary axis in Figure 15b. The large extent of cracking in EP samples implies that the Zr layer may be embrittled as a result of its fabrication in these samples. Indentation testing revealed that the hardness of the EP Zr barriers is relatively high in comparison to the other types of diffusion barriers, and the hardness and reduced modulus are shown in Table 2 in comparison with a commercial purity Zr disk. Using a Poisson ratio of 0.04 [122] to calculate the Young's Modulus found in DUM912, the value of 133 GPa closely resembles the value of 130 GPa reported for δ-$ZrH_{1.5}$ from first principle calculations [122]. A value of 0.3 was assumed for the Poisson's ratio of the barrier in the remaining samples, representing the Poisson's ratio of α-Zr [123]. The results suggest that DUM916 may consist of α-Zr and DUM941 contained a mixture of α-Zr and δ-$ZrH_{1.5}$, with indents occurring on each phase and the obtained modulus representing an average value.

Table 2. Hardness and reduced/elastic moduli determined via nanoindentation of diffusion barriers. α-Zr and δ-$ZrH_{1.5}$ values are included for comparison.

Sample ID (*Sample type*)	Hardness (GPa)	Reduced Modulus (GPa)	Poisson's Ratio	Young's Modulus (GPa)
DUM912 (*EP*)	9.6 ± 1.2	121 ± 7	0.04*	133 ± 7
DUM916 (*PS*)	6.4 ± 1.0	91 ± 7	0.33	87.9 ± 6
DUM941 (*RB*)	2.5 ± 0.2	109 ± 5	0.33	107 ± 4
α-Zr (*disk*)	1.7 ± 0.3	93 ± 4	0.33	89.2 ± 3
δ-$ZrH_{1.5}$ (*calculated*)*	-	-	0.04*	130*

*Data taken from [122].

The BSE micrograph in Figure 19a demonstrates an inhomogeneous microstructure of the diffusion barrier in DUM913. However, no compositional difference was detected using EDS suggesting that the contrast may be a result of low-Z element inhomogeneity. A TEM lamella

containing a region of the diffusion barrier was lifted out of DUM913 and a high-angle annular dark field (HAADF) micrograph of the lamella is shown in Figure 19b. Several SAED patterns were collected throughout the barrier region, each revealing strong peaks consistent with δ-$ZrH_{1.5}$. Figure 19c shows a typical diffraction pattern containing both indexed δ-$ZrH_{1.5}$ peaks and α-Zr peaks (italicized text). Diffraction patterns collected from various regions of the sample primarily exhibited the δ-$ZrH_{1.5}$ structure, indicating limited presence of elemental Zr in the diffusion barrier. The pattern in Figure 19d shows schematically the individual contributions of δ-$ZrH_{1.5}$ (circles) and α-Zr (triangles) to the overall pattern observed.

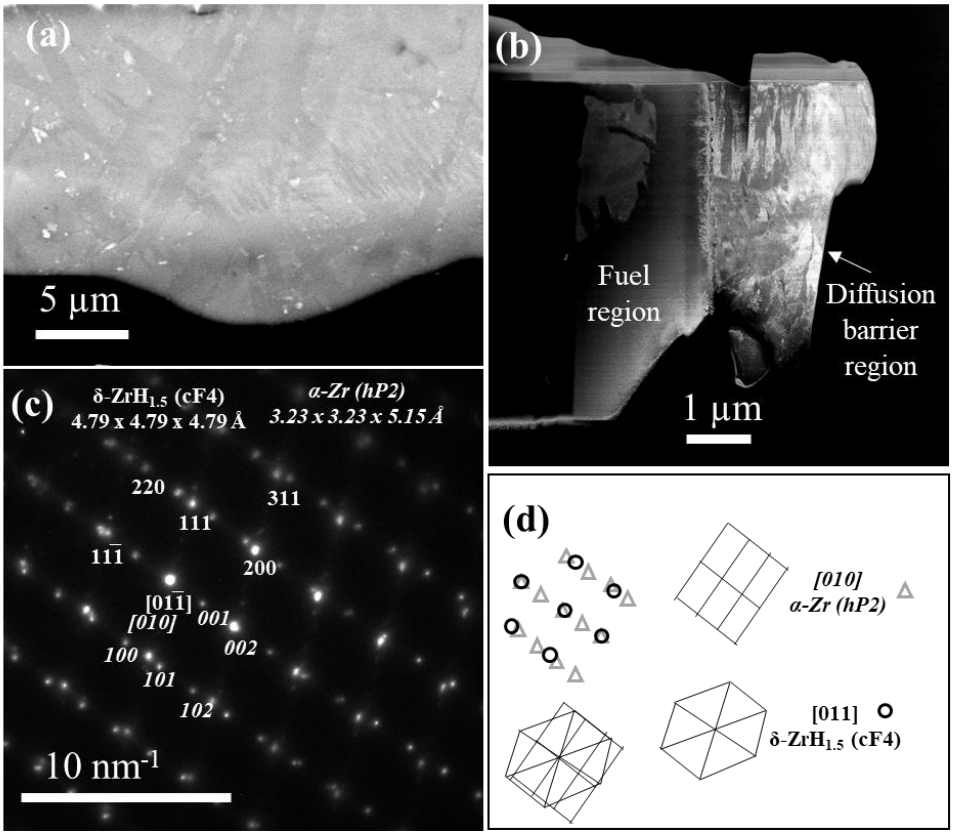

Figure 19. (a) High contrast BSE micrograph showing inhomogeneous diffusion barrier in DUM913. (b) HAADF micrograph of the TEM lamella taken from the fuel/barrier interface. (c) SAED pattern collected from diffusion barrier containing a combination of α-Zr and δ-$ZrH_{1.5}$ peaks, illustrated in (d).

While the diffraction pattern in Figure 19d shows peaks from both α-Zr and δ-$ZrH_{1.5}$, the diffusion barrier consisted primarily of the latter. An SAED pattern typical of the diffusion barrier region is shown in Figure 20, with no evidence of the α-Zr phase.

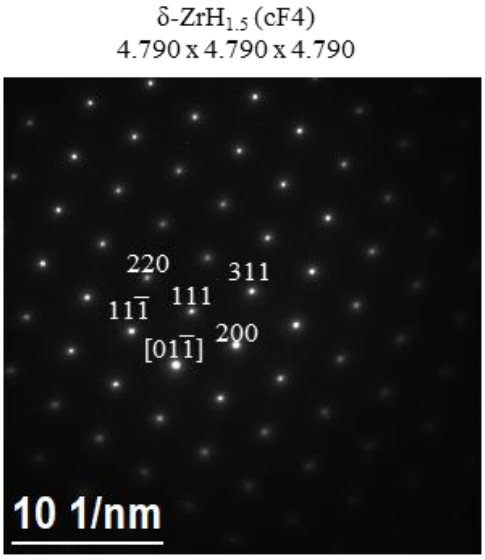

Figure 20. SAED pattern collected from the diffusion barrier region of DUM913, showing δ$ZrH_{1.5}$ peaks and no evidence of α-Zr.

The constituents of the interdiffusion zones between the fuel and diffusion barriers were also investigated using BSE and EDS analysis. The microstructure of interdiffusion zones in samples DUM926, DUM927, DUM941, and DUM942 appeared consistent with those reported in the literature for RB diffusion barriers, likely containing α-U, Mo_2Zr, and UZr_2 [12, 88, 89]. A TEM lamella was lifted from the fuel-barrier interface of DUM941 and is shown in the bright-field micrograph in Figure 21a. SAED patterns were collected at the locations indicated and are representative of (b) γ-U10Mo solid solution, (c) α-U, (d) δ-UZr_2, and (e) α-Zr, as shown in Figure 21.

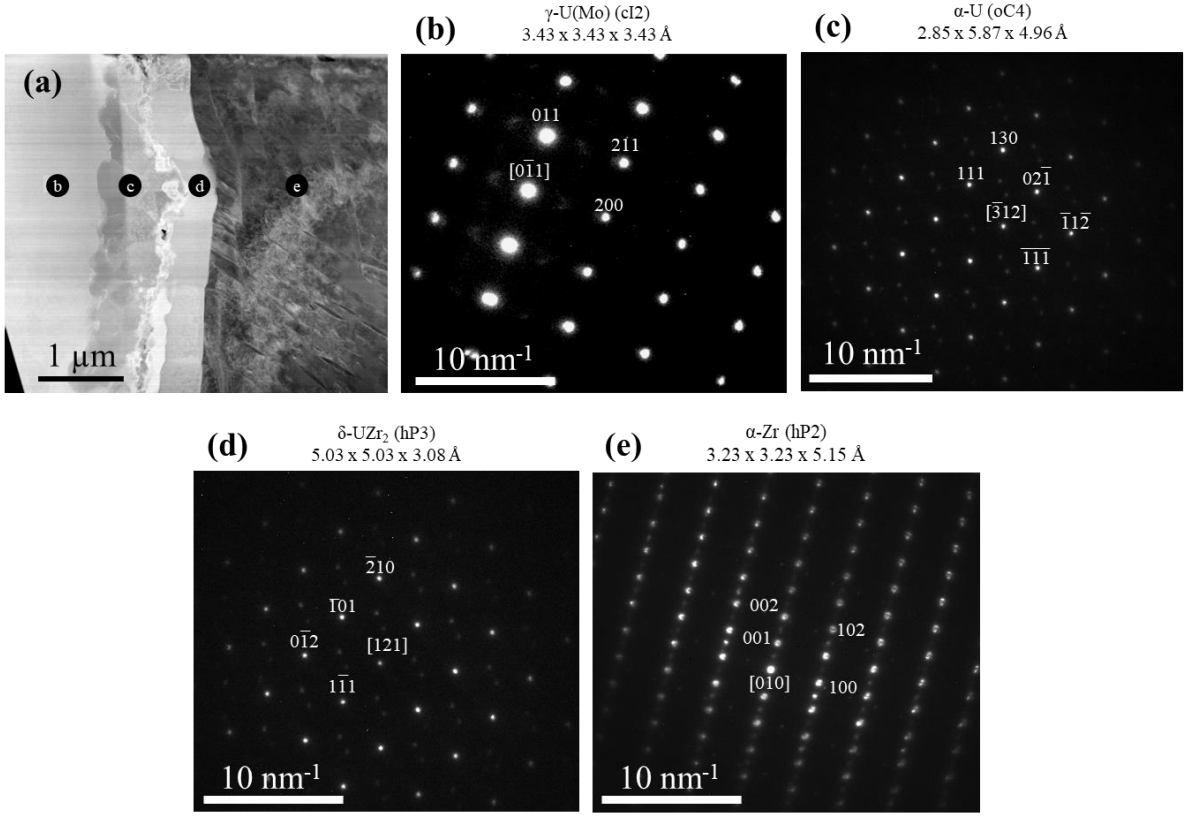

Figure 21. (a) HAADF micrograph and SAED patterns corresponding to (b) γ-U10Mo solid solution, (c) α-U, (d) δ-UZr_2, and (e) α-Zr at the interface of the fuel and diffusion barrier in DUM 941

The interaction layer observed in DUM913 (Figure 22a) was similar in regions where the interaction developed to a few microns in thickness, but the sample also exhibited regions with rather limited interaction (<1 μm). Unlike in the RB samples, however, these highly developed regions in DUM913 contained an additional thin unidentified layer, indicated by the white arrow in Figure 22b. A TEM lamella was fabricated containing from a less-developed interaction region (<1 μm) of the fuel-barrier interface of DUM913, containing only a thin interaction layer. Though the features were smaller in this area, the overall microstructure appeared similar to that of the thicker interaction regions. Point-and-shoot EDS analysis was conducted at the areas indicated by the red circles in Figure 22c, and a representative spectrum is shown in Figure 22d. The EDS

spectra indicated local enrichment of F, likely as a result of the EP process utilizing a molten fluoride-salt bath as the plating electrolyte. The F-enriched layer was thin in the TEM lamella and was thus unable to be investigated using SAED. The remaining EP samples (DUM911, DUM912, and DUM914) exhibited no appreciable interaction throughout their fuel-barrier interfaces.

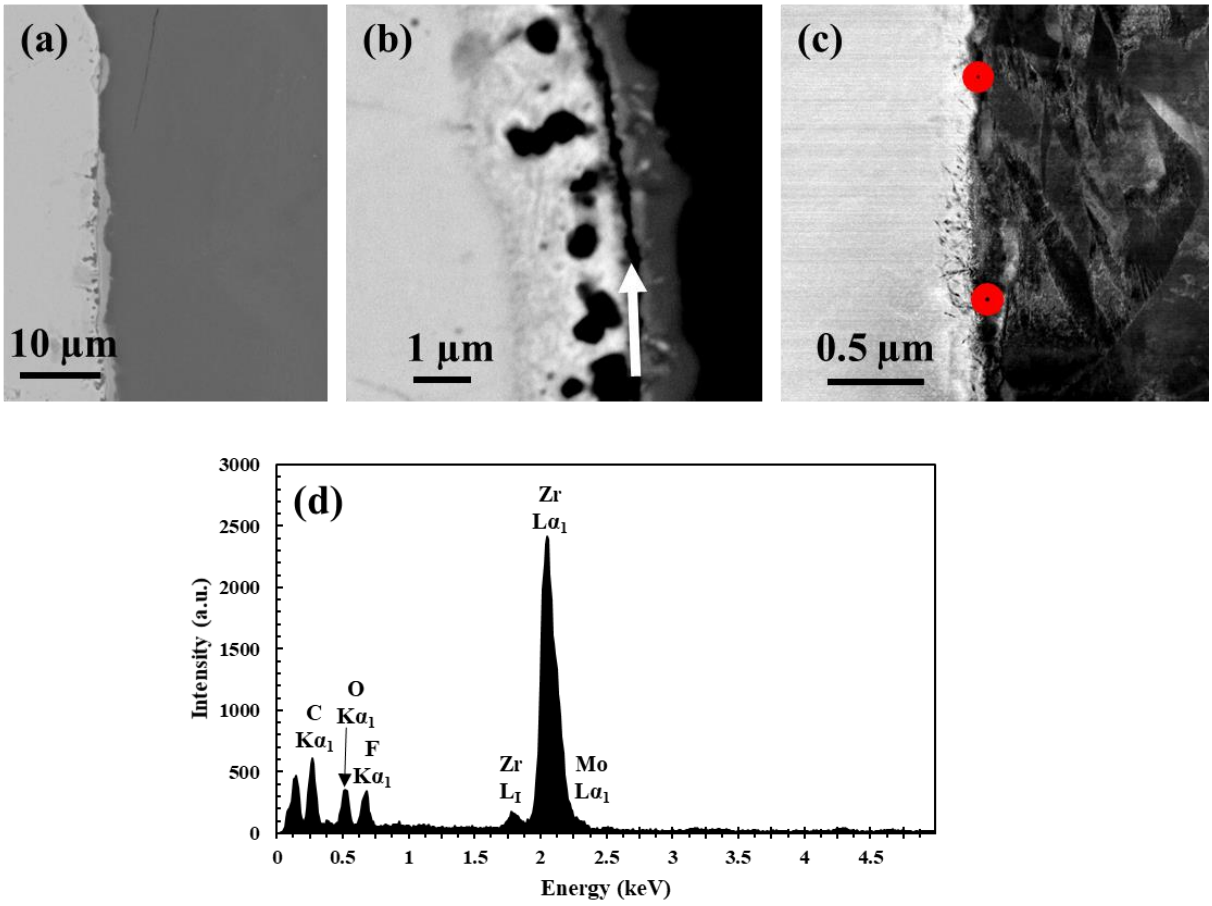

Figure 22. (a) Low- and (b) high-magnification BSE micrographs of the fuel-barrier interface in DUM913. The (c) STEM micrograph and (d) EDS spectrum indicate F enrichment in the layer indicated by the white arrow in (b).

The interaction layer between the fuel and diffusion barriers in DUM915 and DUM916 deviated from the rest of the samples in terms of composition and morphology. The x-ray map in Figure 17c demonstrates local enrichment of O along the interface, and the BSE micrograph and

line scan in Figure 23a and b demonstrate that the O enrichment coincides with one layer (phase) within the interdiffusion zone. A TEM lamella was lifted out of the interface region, and a bright field micrograph is shown in Figure 23c. The SAED patterns and high-resolution TEM with fast Fourier transform (FFT) in Figure 10d-f demonstrate that the fuel, interaction layer, and diffusion barrier are (d) γ-U10Mo solid solution, (e) UO_2, and (f) α-Zr, respectively. Given the similar microstructure in DUM915, it is assumed to contain the same constituents.

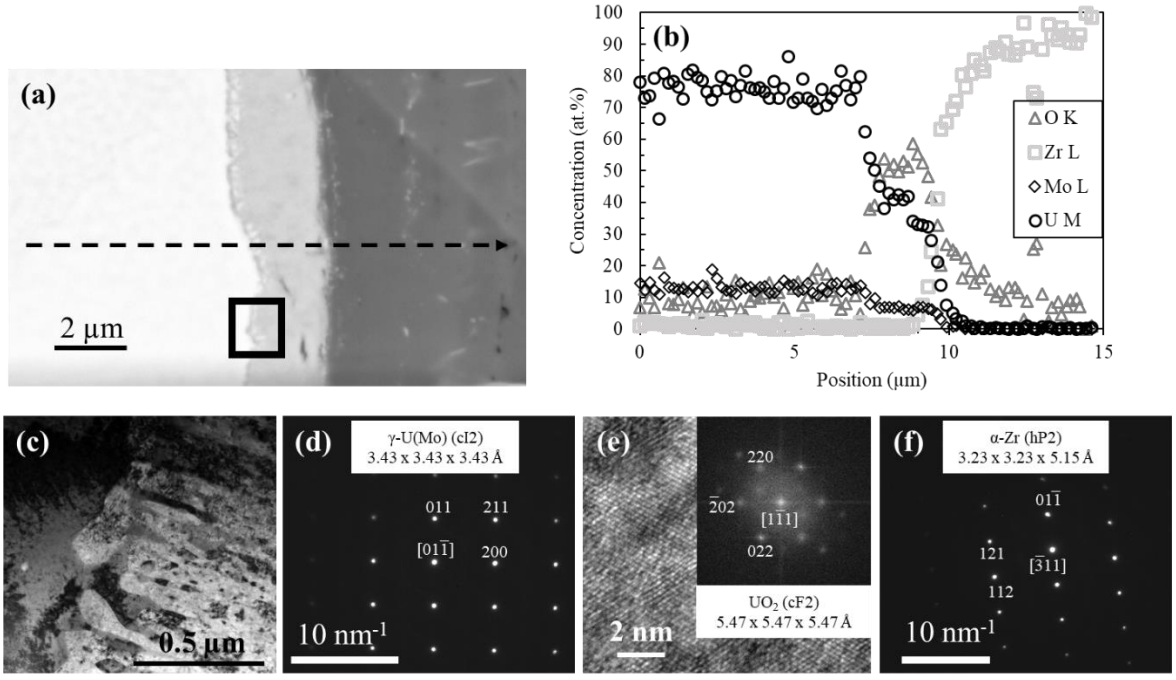

Figure 23. (a) BSE micrograph of the interaction layer between fuel and diffusion barrier in DUM916. The dashed arrow corresponds to (b) the EDS linescan. The box corresponds to (c) the bright-field micrograph containing (d) the γ-U10Mo fuel and (e) the UO_2 layer. (f) SAED taken in the diffusion barrier region indicates α-Zr.

The PS and EP techniques possess the advantage of covering the sheared edges of the U10Mo foil while they remain uncovered following the RB process. Examples of the edge coverage of the PS and EP diffusion barriers are shown in Figure 24. As shown, the sheared edges exhibit Zr coverage, but the interfaces are mostly characterized by non-uniformity and extensive

cracking throughout each sample, with the exception of DUM915 (Figure 24e). While the sheared fuel edges remain uncovered in RB samples, uncovered edges demonstrate tolerable behavior under irradiation conditions [22]. The characteristics of Zr diffusion barriers that resulted from the EP, PS, and RB process suggest that RB may produce the most favorable properties of the candidates investigated.

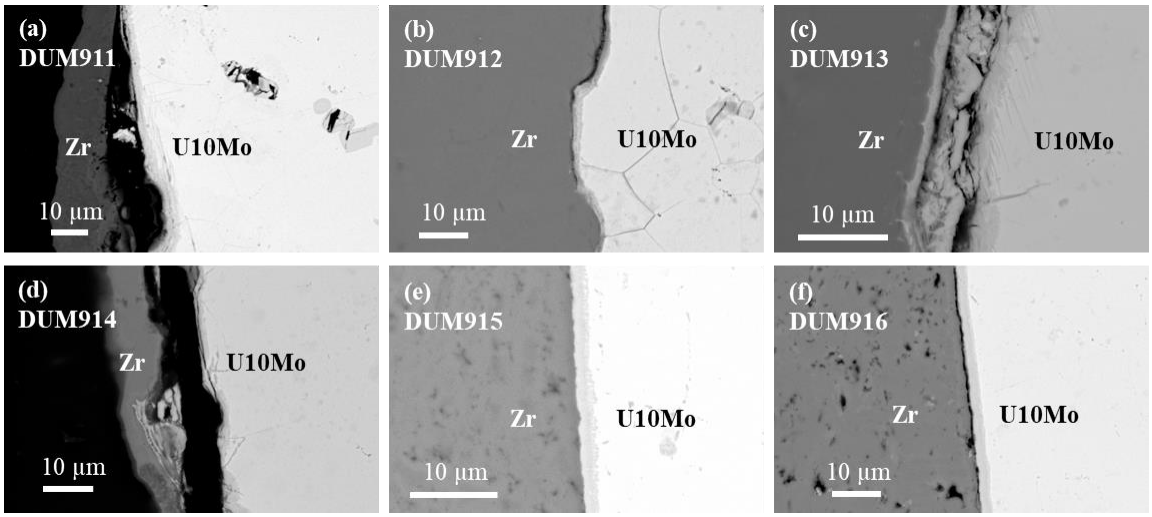

Figure 24. BSE micrographs showing the diffusion barrier coverage on fuel edges of (a) DUM911, (b) DUM912, (c) DUM913, (d) DUM 914, (e) DUM915, and (f) DUM916. DUM911-DUM914 (a-d) have EP diffusion barriers and DUM915-DUM916 (e-f) have PS diffusion barriers.

CHAPTER 5: ISOTHERMAL PHASE TRANSFORMATIONS IN URANIUM-10 WT. % MOLYBDENUM ALLOY

5.1 Homogenized γ-U10Mo

During fabrication and operation, the U10Mo foil undergoes phase transformations from γ to α+γ' and back to γ. To provide an initial condition for investigating these phase transformations, U10Mo disks received at UCF underwent homogenization heat treatment at 800°C for 96 h. The disks were then polished for characterization and analyzed with SEM and XRD. The BSE micrograph in Figure 25 shows the overall microstructure, and the black rectangles indicate several areas where EDS spectra were collected to determine the overall composition. One resulting EDS spectrum is shown in Figure 26 and the results of analysis are shown in Table 3.

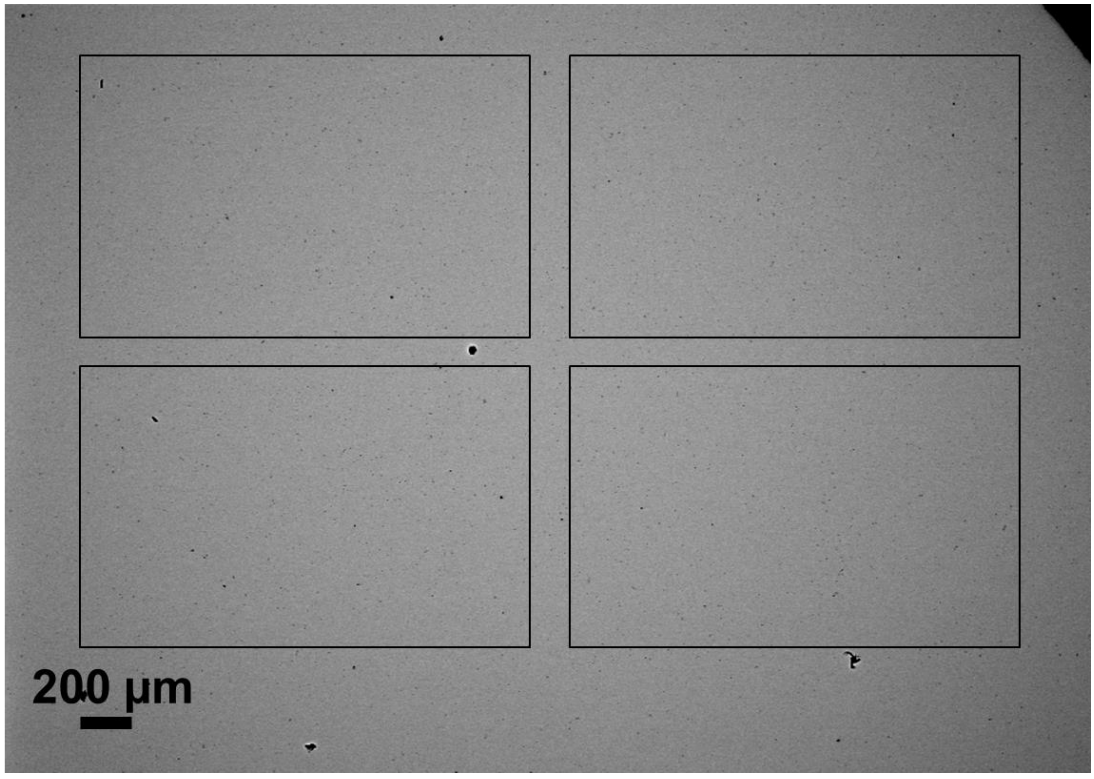

Figure 25. BSE micrograph of U10Mo disk homogenized at 800°C for 96 h. The black rectangles indicate the areas where EDS spectra were collected for composition analysis.

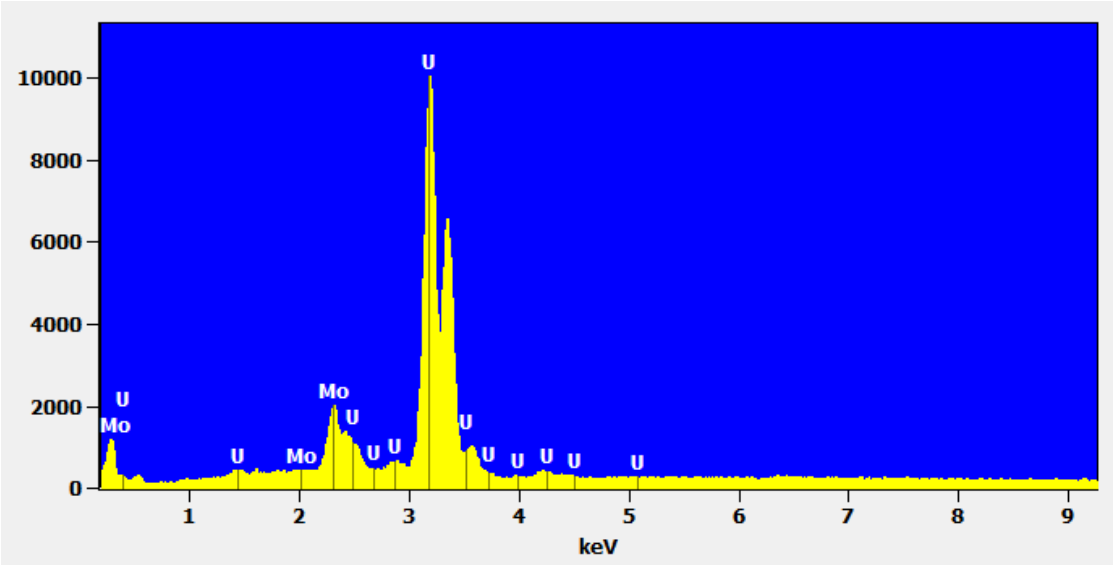

Figure 26. EDS spectrum collected from one of the areas of the homogenized U10Mo disk shown in Figure 25.

Table 3. Overall composition of homogenized U10Mo disks, taken from the areas indicated in Figure 25.

Atom	Weight Percent	Atom Percent
Mo	9.3 ± 0.15	20.3 ± 0.30
U	90.7 ± 0.15	79.7 ± 0.30

The crystal structure of the disks was also analyzed via XRD, and an indexed pattern is shown in Figure 27. The solid line represents the experimental data while the black triangles represent the peak locations and relative intensities according to the γ-U powder diffraction file (PDF). The experimental peak locations deviate from the PDF as a result of substitutional Mo atoms in solid solution. From the experimental peak locations, the precise lattice parameter can be calculated using the extrapolated Nelson-Riley function. The resulting precise lattice parameter is 3.4275 Å, and the calculation is shown graphically in Figure 28.

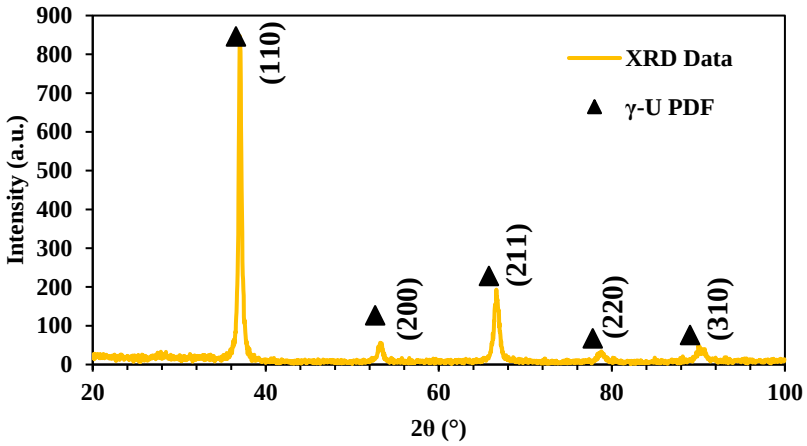

Figure 27. XRD spectrum collected from U10Mo disk homogenized at 800°C for 96 h.

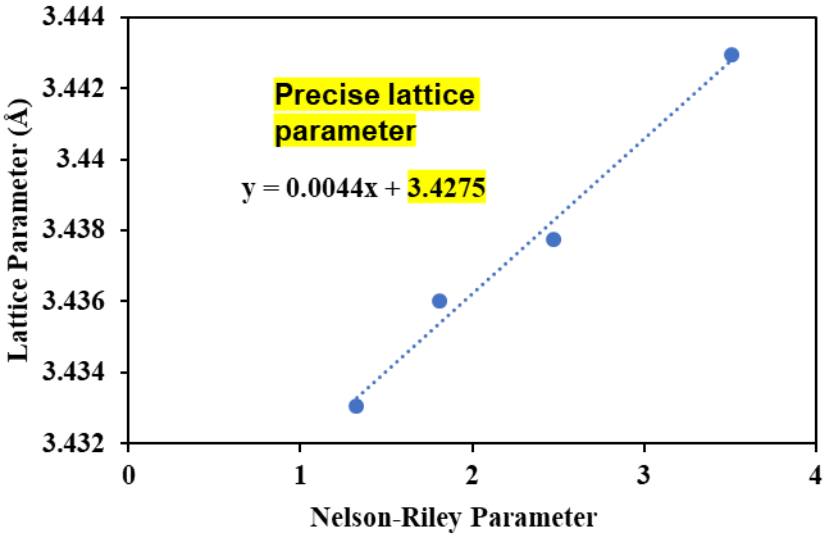

Figure 28. Extrapolated Nelson-Riley function used to calculate the precise lattice parameter of homogenized U10Mo disk.

An exercise to verify the analysis can be done by comparing the values of lattice parameter and composition with those that would result from the composition of U alloyed with 9.3 wt. % Mo (from EDS). Substitution of 9.3 wt. % Mo equates to 20.3% of the γ lattice sites occupied by Mo atoms. According Vegard's rule of mixtures, this would result in a lattice parameter of ~3.44

Å. These results suggest that the disk is without dramatic deviation from the average composition of 9.3 wt. % Mo, and the peak positions identified in this scan will be used in deconvolution of patterns containing γ, α, and γ'.

In some areas of the U10Mo rod, large needle-like inclusions were observed. EDS showed that these inclusions were composed of pure Mo, likely resulting from incomplete melting during casting. Due to the limited availability of U material, these disks were still used in the phase transformation studies. However, microstructural and EDS analysis was carried out far away from these inclusions, where the behavior is assumed not to be affected. An example of the Mo inclusion is shown in Figure 29. The inclusion may appear in XRD spectra taken from the affected disks, and the peak is addressed in the discussion of the results.

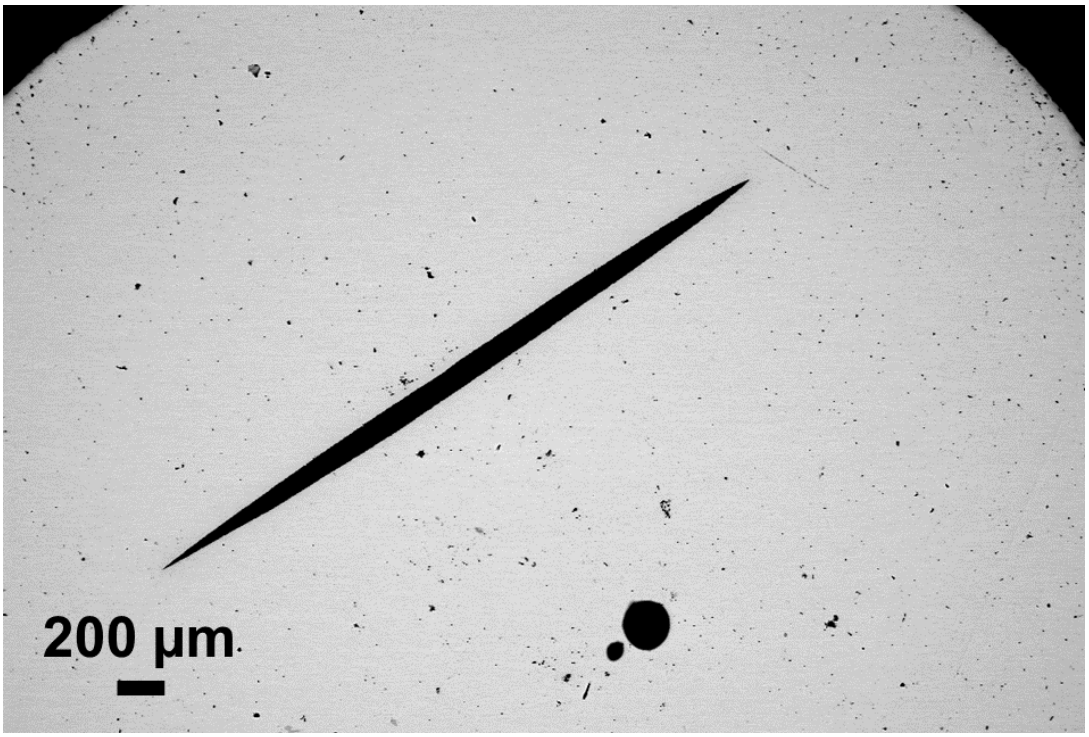

Figure 29. BSE micrograph showing Mo inclusion resulting from incomplete melting during casting of the U10Mo rod.

5.2 Isothermal Decomposition of γ-U10Mo at 500°C

The binary U-Mo phase diagram in Figure 3 indicates that at 500°C, α+γ' is the equilibrium microstructure, and the T-T-T diagram in Figure 4 outlines the decomposition behavior from the initial γ phase microstructure. However, some discrepancy exists among literature regarding γ decomposition in U-Mo alloys. To investigate the possible cause of this discrepancy, as well as to provide a completely decomposed initial condition for experiments investigating γ reversion, U10Mo disks were homogenized then annealed at 500°C.

While the decomposition has been described as classic eutectoid decomposition, recent studies have suggested that the decomposition may be more accurately described using the alternative precipitation mechanisms, which differ depending on temperature [49, 56, 124]. The mechanisms involved are continuous precipitation (CP) and discontinuous precipitation (DP), followed by discontinuous coarsening (DC). To investigate the microstructural evolution in U10Mo alloys, disks were annealed at 500°C from 240 to 1,200 h and water quenched. After 240 h, the microstructure contained morphologies characteristic of both continuous and discontinuous precipitation. The characteristic DP microstructure contains a combination of α, γ, and γ' lamella while the characteristic CP microstructure consists of acicular precipitates in a continuous γ matrix. An example of the interface between a DP colony and the γ matrix is shown in Figure 30. In the γ matrix, acicular precipitates assumed to be CP γ' are evident and are highlighted with red circles in Figure 30a. TEM investigation was carried out on these precipitates and a HAADF-STEM image is shown in Figure 30b. SAED confirmed that crystal structure of the matrix consists of BCC γ, as shown in Figure 30c, while the precipitates were confirmed as tetragonal γ', shown in Figure 30d.

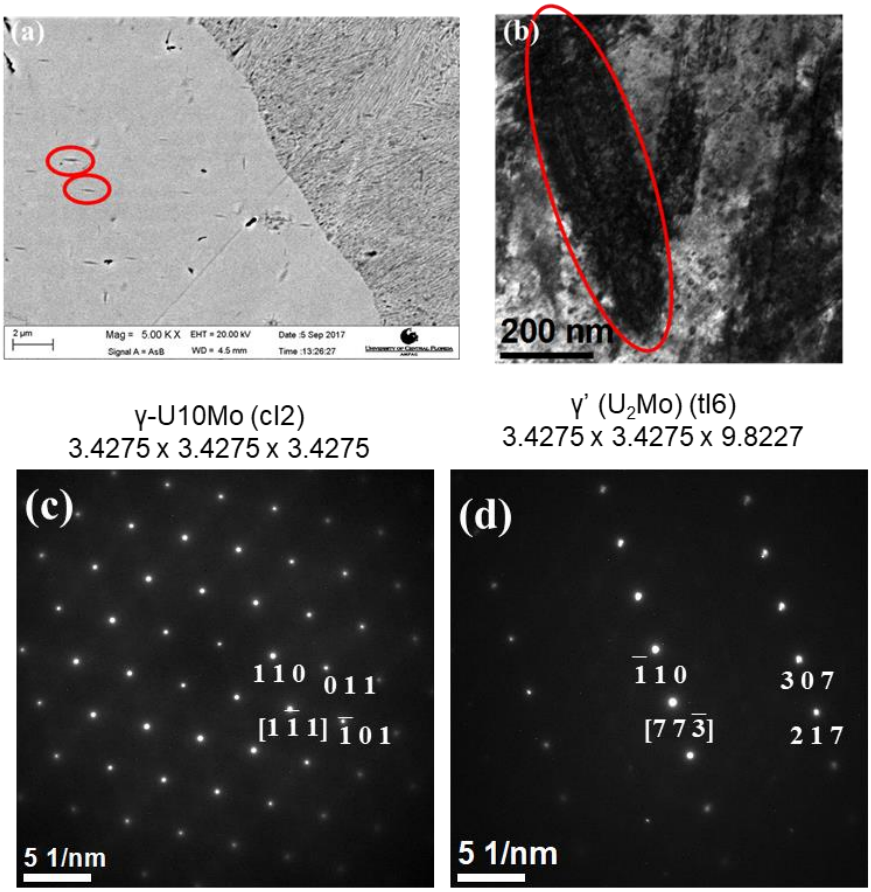

Figure 30. (a) BSE SEM and (b) HAADF-STEM micrographs of U10Mo disk decomposed at 500°C for 10 days. The SAED patterns show that the matrix is BCC γ (c) and the precipitate is BCT γ' (d)

After 480 h at 500°C, the DP colonies continued to grow outward from nucleation sites, consuming most of the γ matrix throughout the disks, as shown in Figure 31. The solid, lighter region labeled untransformed γ in Figure 31 represents untransformed γ matrix amidst the decomposed DP colonies. The CP γ' needles lengthened and thickened within the γ matrix, and the higher magnification BSE micrograph in Figure 32 demonstrates the morphology of the CP needles in the γ matrix.

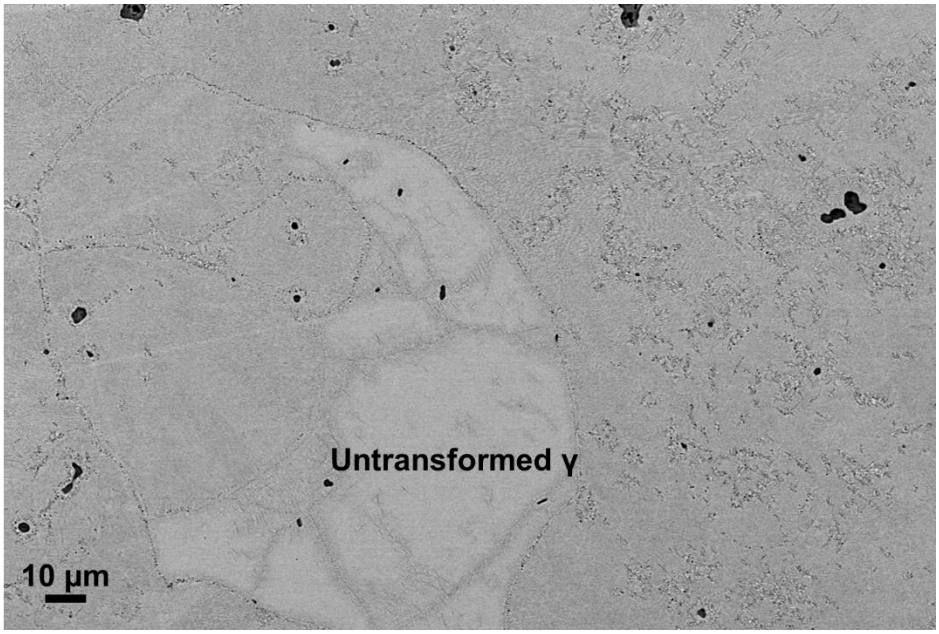

Figure 31. BSE micrograph showing a U10Mo disk decomposed at 500°C for 480 h. The darker, non-uniform regions represent DP decomposed areas while the lighter, solid region represent untransformed γ. CP γ' needles can be seen throughout the untransformed γ matrix.

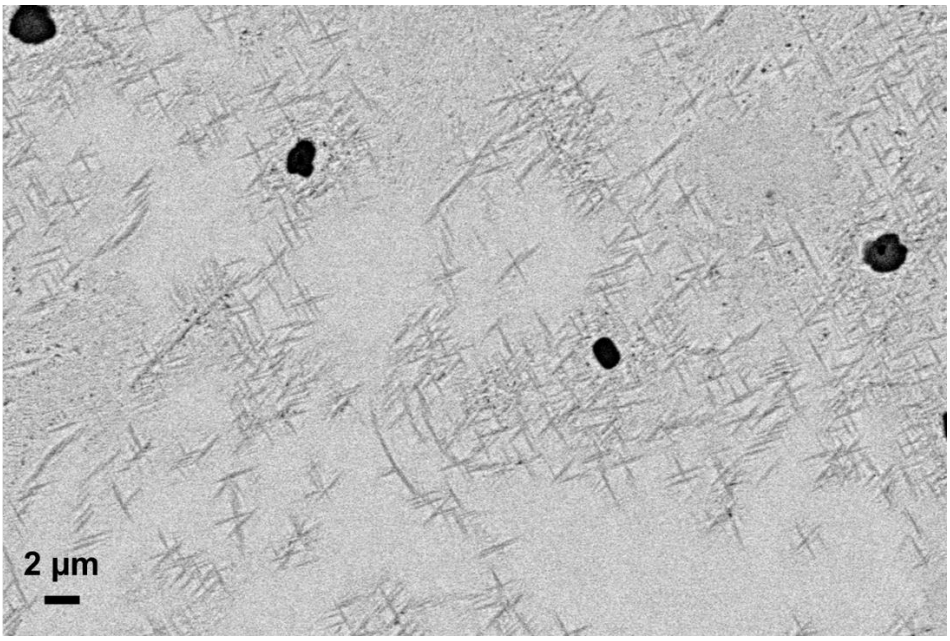

Figure 32. BSE micrograph detailing CP γ' within the untransformed γ matrix.

Following 720 h at 500°C, no large continuous regions of untransformed γ remain. However, the decomposed microstructure remains inhomogeneous; the disks contain a mixture of lamellar and non-lamellar microstructure. Representative BSE micrographs are shown in Figure 33. Figure 33a and b show examples of the lamellar and cellular microstructures, respectively.

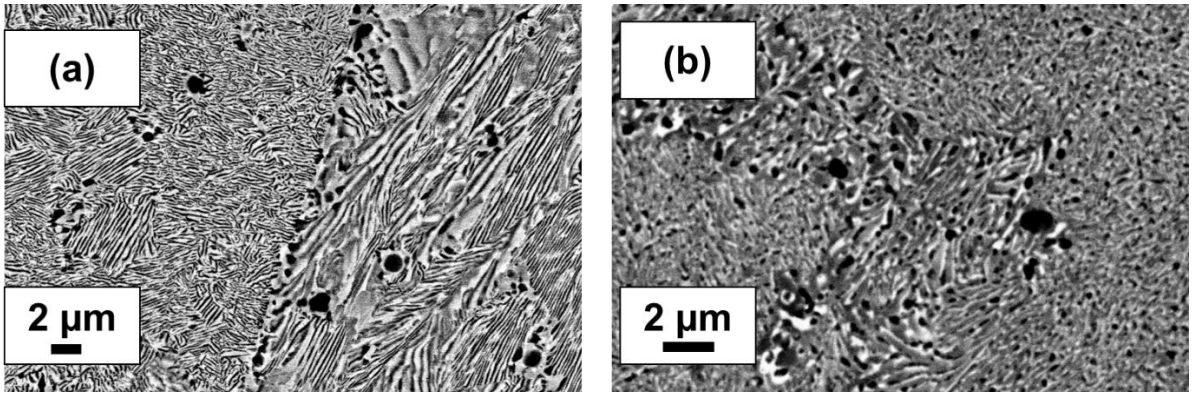

Figure 33. BSE micrographs of U10Mo disk decomposed at 500°C for 720 h demonstrating the (a) lamellar and (b) cellular morphologies of the decomposed α+γ' microstructure.

To identify the crystal structures of the phases present in the disks after 720 h at 500°C, XRD and TEM investigation were carried out. The indexed XRD spectrum is presented in Figure 34. The UC and UO_2 peaks identified are commonly observed in U10Mo disks, and the Mo peak identified is a result of the inclusion shown in Figure 29. A TEM specimen was removed from a lamellar region of the disk and bright-field and HAADF-STEM micrographs are shown in Figure 35a and b, respectively. The SAED patterns in Figure 35c and d confirmed the crystal structures of α-U and γ', respectively.

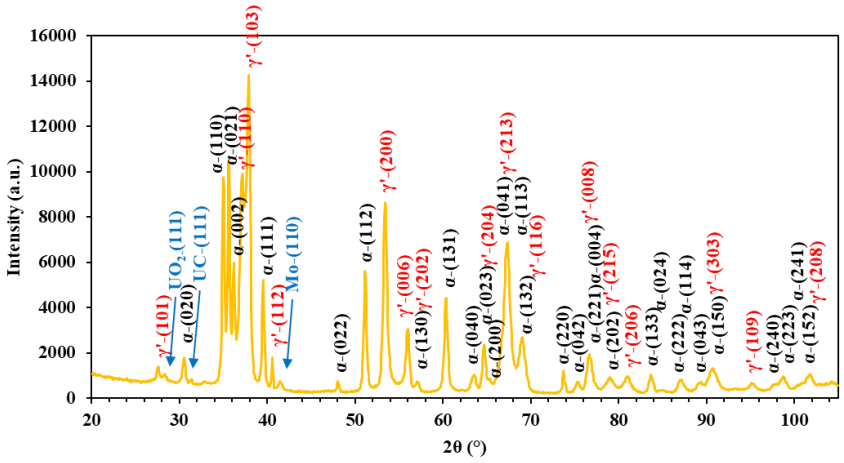

Figure 34. XRD pattern obtained from U10Mo disk decomposed at 500°C for 720 h.

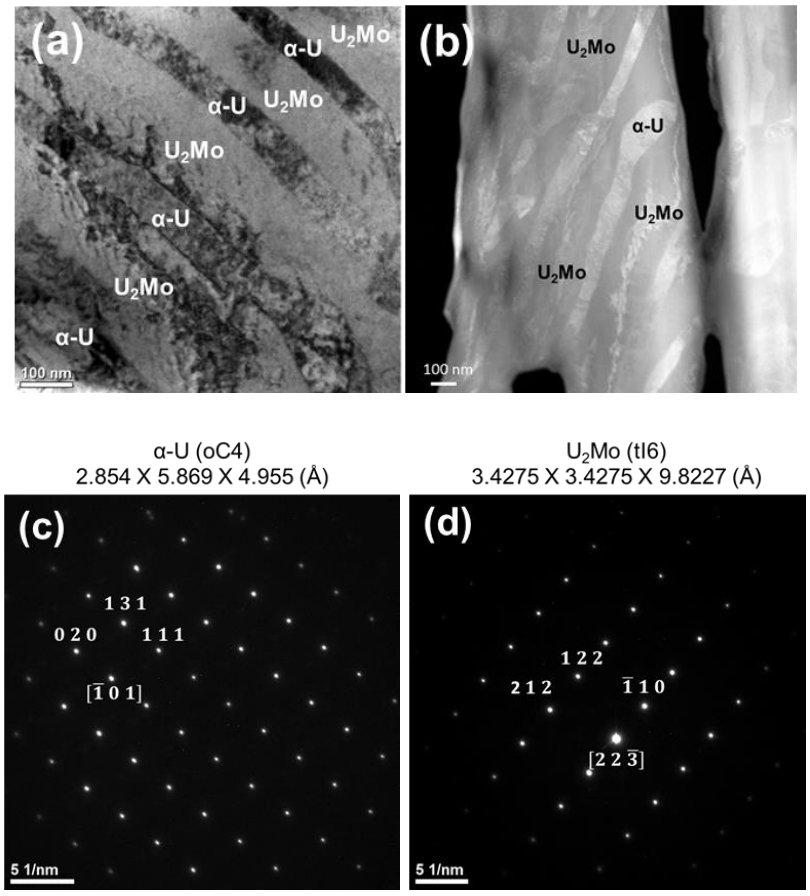

Figure 35. (a) Bright-field and (b) HAADF-STEM micrographs of TEM sample removed from a lamellar region of a U10Mo disk decomposed at 500°C for 720 h. The SAED patterns represent the (c) α and (d) γ' crystal structures.

Heat treatment was carried out at 500°C for 960 and 1200 h to further detail the long-term resulting microstructural evolution in U10Mo disks. After 960 h, coarsened microstructure is apparent along grain boundaries and inclusions, such as carbides and oxides serving as initiation sites, as shown in Figure 36. Further heat treatment to 1200 h results in growth of the DC areas toward the grain interior, as shown in Figure 37. The higher magnification BSE micrograph in Figure 38 shows the characteristic DC microstructure growing from a grain boundary toward the grain interior at the expense of the existing DP microstructure.

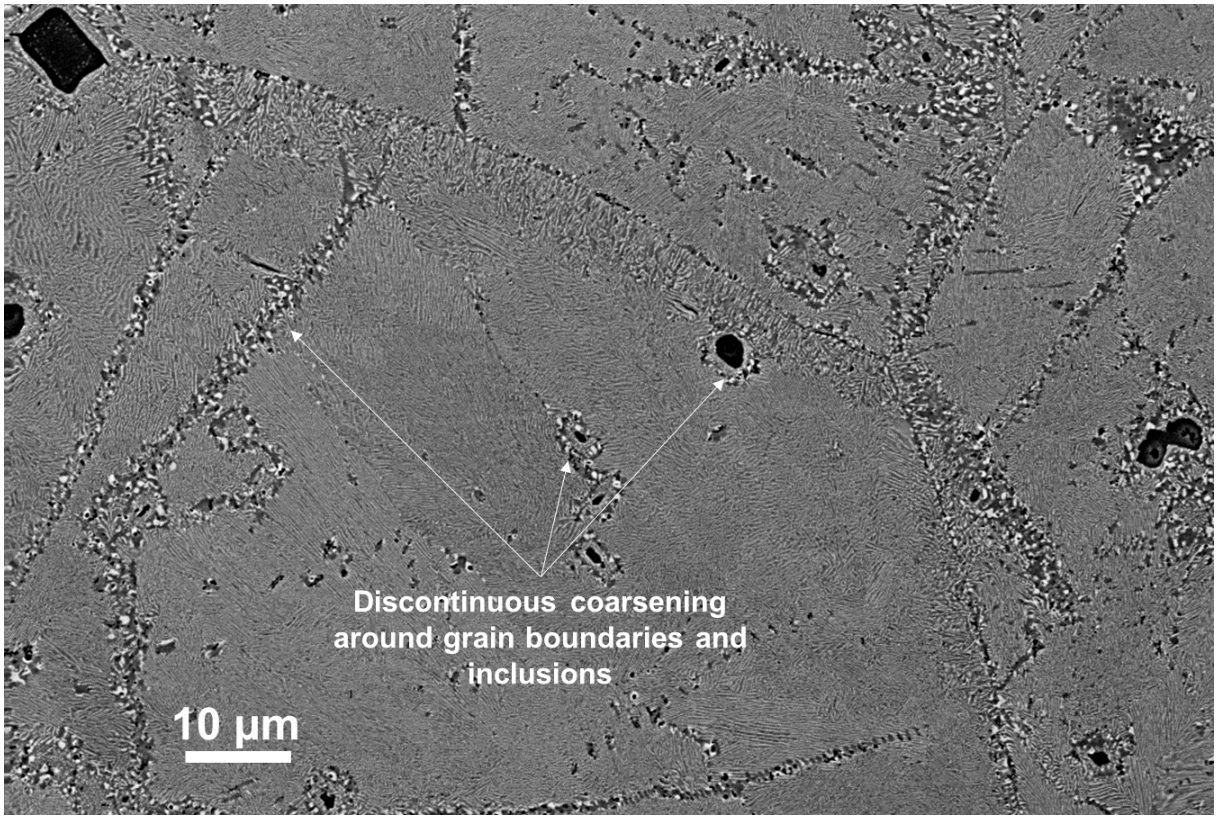

Figure 36. BSE micrograph of a U10Mo disk decomposed at 500°C for 960 h demonstrating the coarsening of α+γ' along initiation sites such as carbides and grain boundaries.

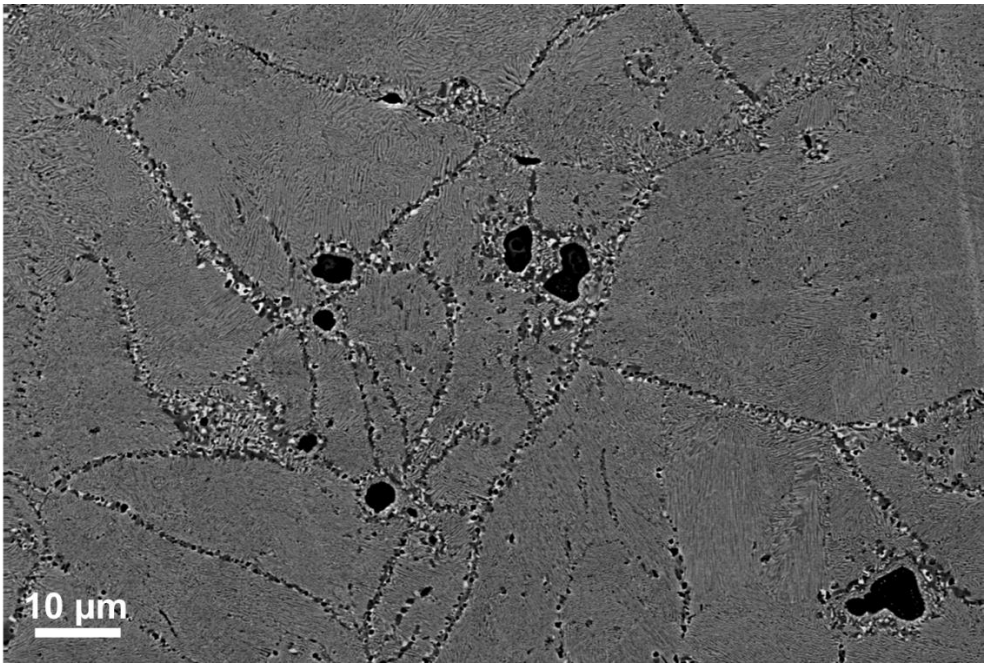

Figure 37. BSE micrograph of a U10Mo disk decomposed at 500°C for 1200 h demonstrating the overall microstructure containing DC features around inclusions and grain boundaries.

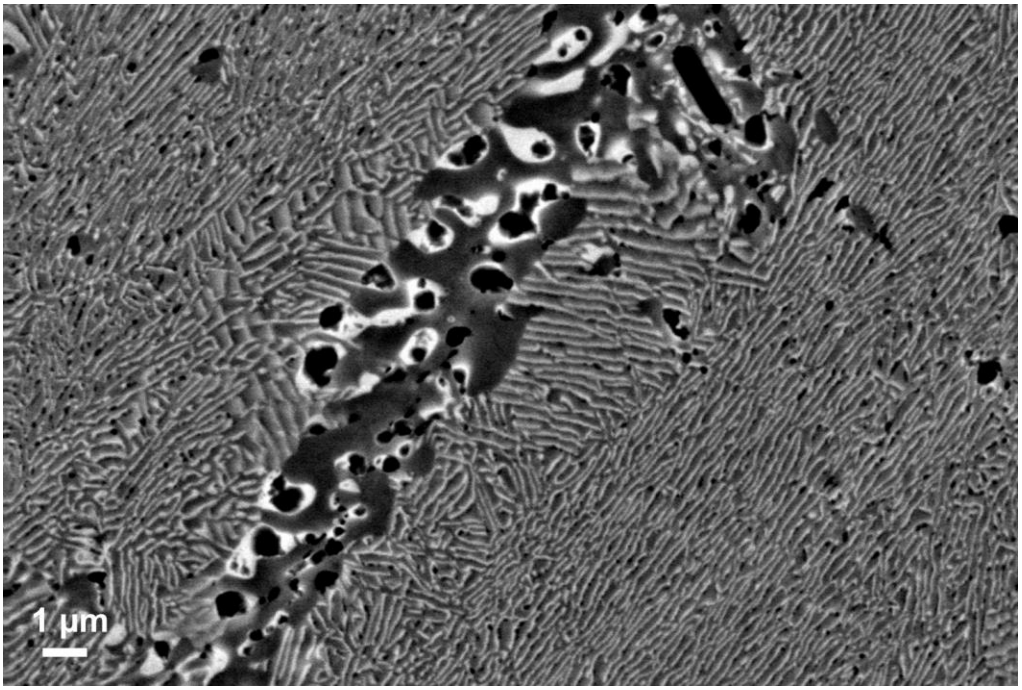

Figure 38. High magnification BSE micrograph demonstrating DC α+γ' microstructure along a grain boundary in a U10Mo disk decomposed at 500°C for 1200 h.

As the U10Mo disks undergo decomposition via CP, DP, and DC, the microstructure remains inhomogeneous even after 1200 h. Consequently, the initial condition for phase reversion heat treatments cannot be selected as a uniform microstructure. As such, 720 h was selected as the initial condition, as after 720 h the continuous γ matrix has been consumed entirely by decomposition products.

5.3 Isothermal Reversion of γ-U10Mo

The reverse $\alpha+\gamma' \rightarrow \gamma$ transformation occurs above the eutectoid temperature 560°C. Given the microstructural evolution in disks decomposing at 500°C, disks decomposed for 720 h were selected as the initial condition for γ reversion investigation. Though the microstructure of the decomposed disks is not uniform, after 720 h the continuous γ matrix has been completely consumed by decomposition products. The BSE micrographs in Figure 33 show that the γ matrix has been consumed by a combination of lamellar and non-lamellar decomposed regions.

After decomposition, several disks were annealed at 570°C for 1, 2, 24, 48, and 96 h. The XRD patterns collected after recrystallization are shown in Figure 39. Utilizing deconvolution and RIR analysis, the amount of each phase in the disks was determined and is presented in Table 4.

Table 4. Results of phase quantification using deconvolution of XRD patterns obtained from U10Mo disks recrystallized at 570°C after decomposition at 500°C for 720 hours.

t (h)	t (min.)	wt. % α	wt. % γ'	wt. % γ
0	0	36.7	63.3	0
1	60	36.2	48.9	14.9
2	120	35.8	26.7	37.4
24	1440	21.2	16.8	62.0
48	2880	3.99	13.1	82.9
96	5760	3.88	4.44	91.7

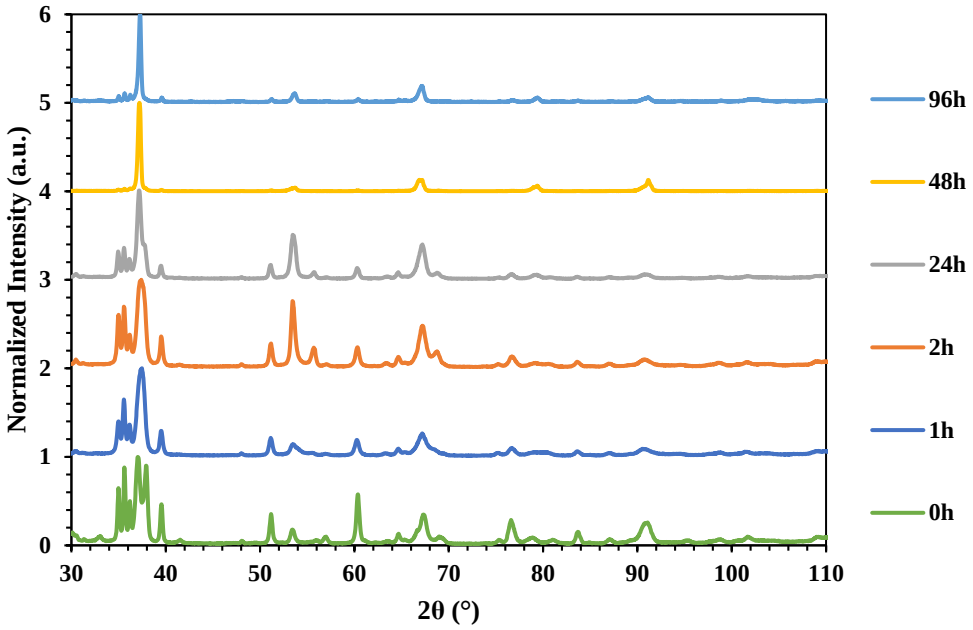

Figure 39. XRD patterns obtained from U10Mo disks decomposed at 500°C and recrystallized at 570°C for the time indicated. 0 h represents the initial decomposed state.

A combinatorial model using JMAK and spherical particle dissolution models is used to describe the overall kinetics of the transformation based on the microstructures observed in the disks. Examples of microstructures that corroborate the use of the classical JMAK and spherical dissolution models are shown in Figure 40. Figure 40a shows a schematic microstructure of grey γ colonies growing in spheres from a matrix of white α and black γ' lamella. The kinetics of this transformation are described using the classical JMAK approach. The schematic in Figure 40b represents the dissolution of spherical particles into a matrix of grey γ, described using the diffusion-controlled dissolution model. The micrograph in Figure 40c depicts round γ regions observed in the disk that appear to grow at the expense of the surrounding α+γ' while the micrograph in Figure 40d shows round particles of α and γ' observed in a γ matrix that may be dissolving in accordance with the spherical particle dissolution model.

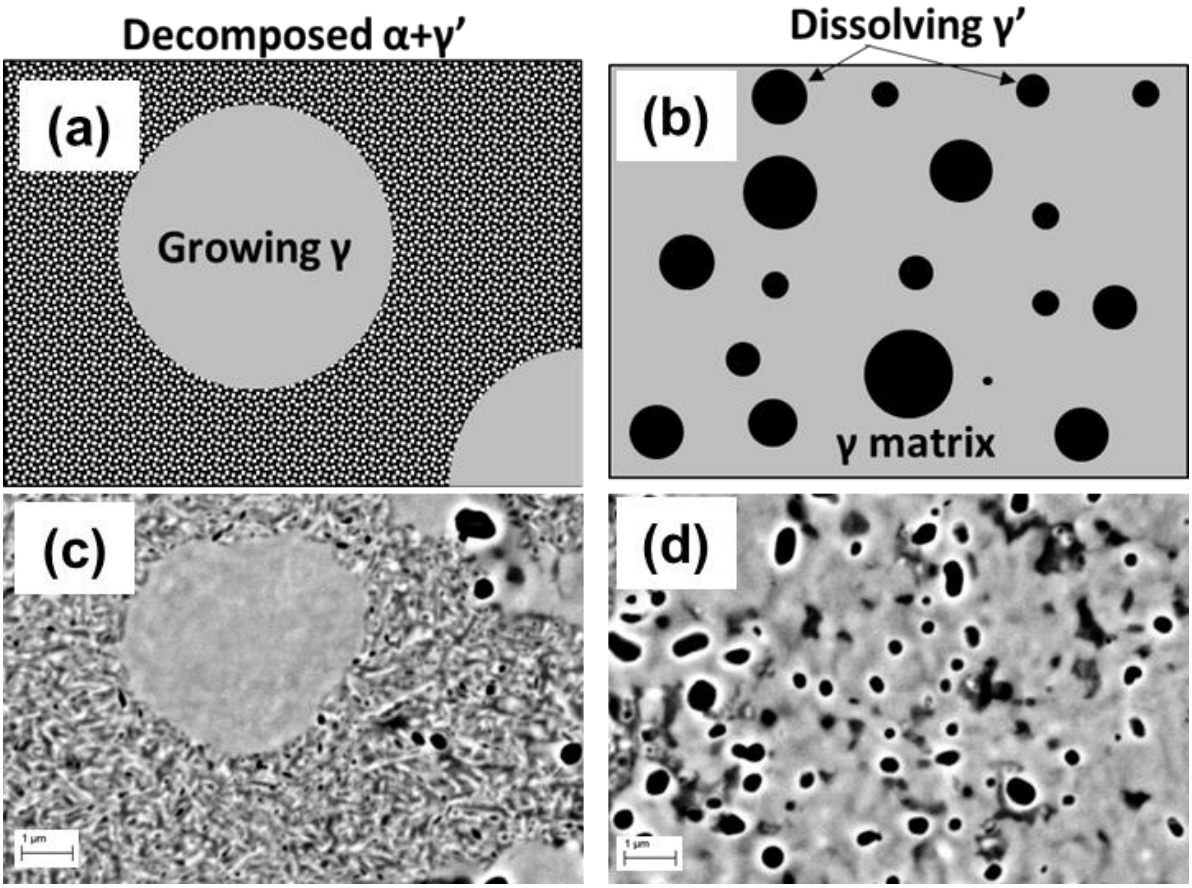

Figure 40. Schematic microstructures and BSE micrographs of (a and c) colonies of γ-U10Mo growing from pearlite and (b and d) spherical particles of α and γ' dissolving into γ-U10Mo matrix.

The micrographs shown in Figure 33 depict fine non-lamellar and coarse lamellar microstructures that may transform via JMAK and spherical particle dissolution, respectively. Using image analysis, it is estimated that the initial decomposed condition is made up of about 50% lamellar and 50% non-lamellar microstructures. From this assumption in conjunction with the assumption of γ growth in the fine microstructure and α+γ' dissolution in the coarser decomposed regions, an overall model is proposed that is constituted of 50% classical JMAK kinetics and 50% spherical particle dissolution. The parameters that contribute to the JMAK portion include nucleation and growth rates, which are typically temperature dependent following

an Arrhenius relationship. However, no data exists on the nucleation and growth rates of γ-U10Mo from the α+γ' microstructure. Consequently, the nucleation and growth rates will be fitted empirically to best fit the data with an Avrami exponent of *n=4*, making the assumption of instantaneous and random nucleation. Additionally, the activation energy used in the Arrhenius relationship is assigned a value of 180 kJ/mol, which is the activation energy for volume interdiffusion in U10Mo [105]. In spherical particle dissolution modeling, the interdiffusion coefficient is taken directly from literature [105], and the concentration variable are taken from the phase diagram; C_e is the equilibrium Mo concentration in γ-U10Mo i.e. 21 at. %, C_p is the Mo concentration in the γ' particles i.e. 33 at. %, and Ci is the interface concetration, represented by the γ solvus line. At 570°C, C_i is approximately 22 at. % Mo.

The resulting overall model as well as contribution of each component are plotted along with the experimental data from XRD analysis in Figure 41.

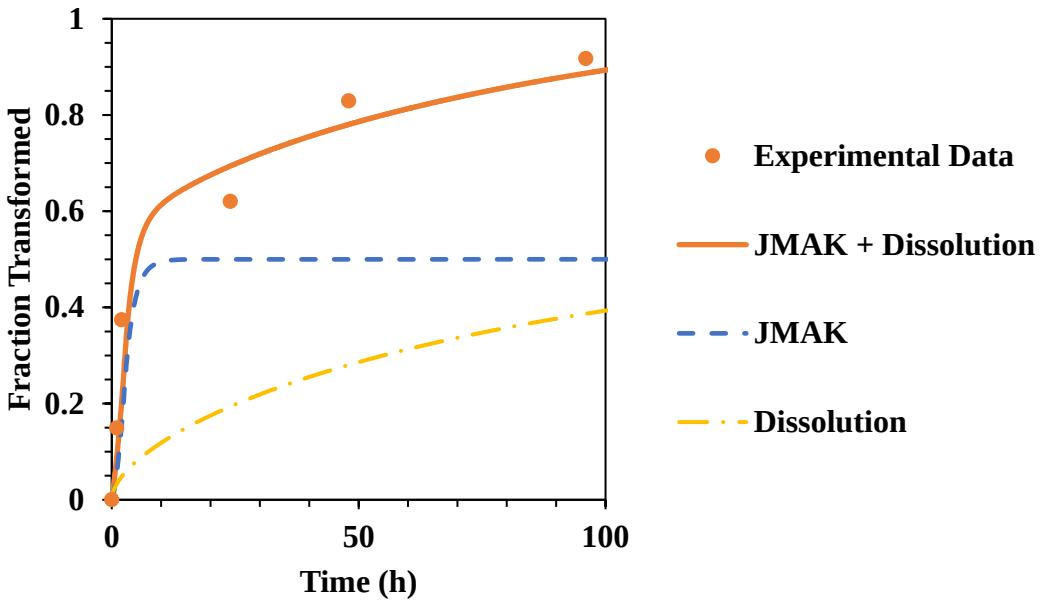

Figure 41. Fraction recrystallized γ as a function of annealing time at 570°C.

The overall modeled behavior appears to describe the data well. The fitted pre-exponential factors for nucleation and growth were fitted at 3 x 10^7 $m^{-3}s^{-1}$ and m/s, respectively. Following the same techniques, samples were annealed at 580°C for times varying from 1 to 24 h, and their respective XRD spectra are shown in Figure 42. To describe the behavior at 580°C, the nucleation rate, growth rate, and interdiffusion coefficient increase per the Arrhenius relationship, and C_i changes per the phase diagram to roughly 24.5 at. % Mo. The experimental results are plotted in Figure 43 along with the results of JMAK and dissolution models, and the results of phase quantification are also shown in Table 5.

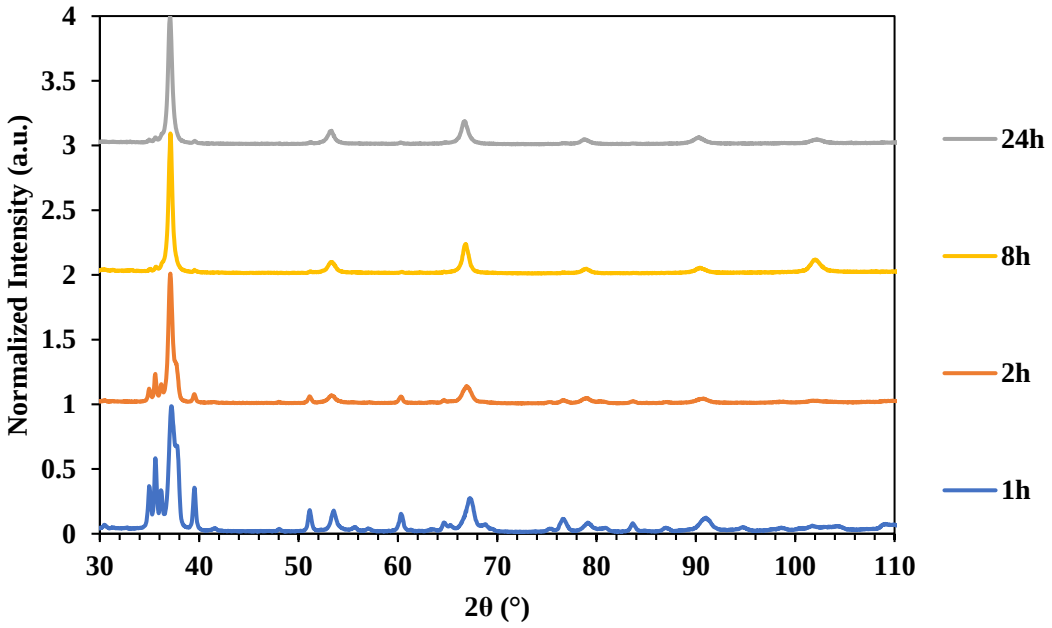

Figure 42. XRD patterns obtained from U10Mo disks decomposed at 500°C and recrystallized at 580°C from 1 to 24 h.

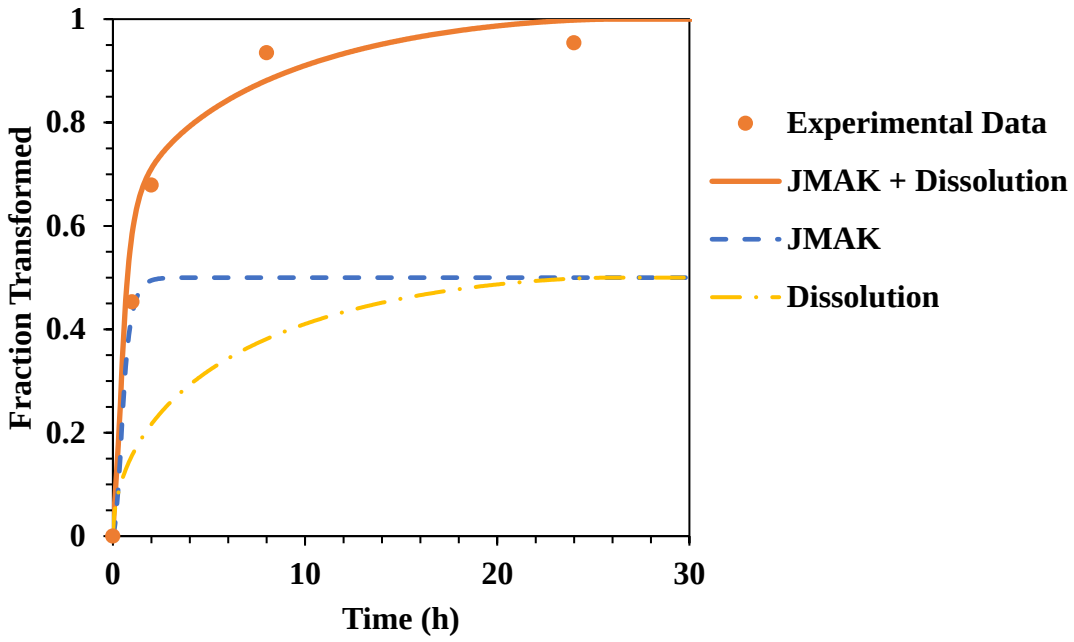

Figure 43. Fraction recrystallized γ as a function of annealing time at 580°C.

Table 5. Results of phase quantification using deconvolution of XRD patterns obtained from U10Mo decomposed at 500°C for 720 hours and recrystallized at 580°C.

t (h)	t (min.)	wt. % α	wt. % γ'	wt. % γ
0	0	36.7	63.3	0
1	60	29.8	24.9	45.3
2	120	16.0	16.0	67.9
8	480	2.34	4.12	93.5
24	1440	2.44	2.14	95.4

At 580°C, the modeled behavior continues to accurately describe the experimental results. The nucleation rate, growth rate, and diffusivity increase with temperature per the Arrhenius relationship and the interface concentration increases per the phase diagram, while remaining variables were unchanged.

The behavior was also investigated as a function of time at 590°C. As the annealing temperature is increased to 590°C, the nucleation rate, growth rate, diffusivity, and interface concentration are further increased, and their increased values are reflected in the modeled behavior. In this case, C_i is increased to 29 at. % Mo. Following heat treatment, the XRD spectra were collected and are shown in Figure 44. The results are shown in Table 6 and the modeled and experimental behavior are shown in Figure 45.

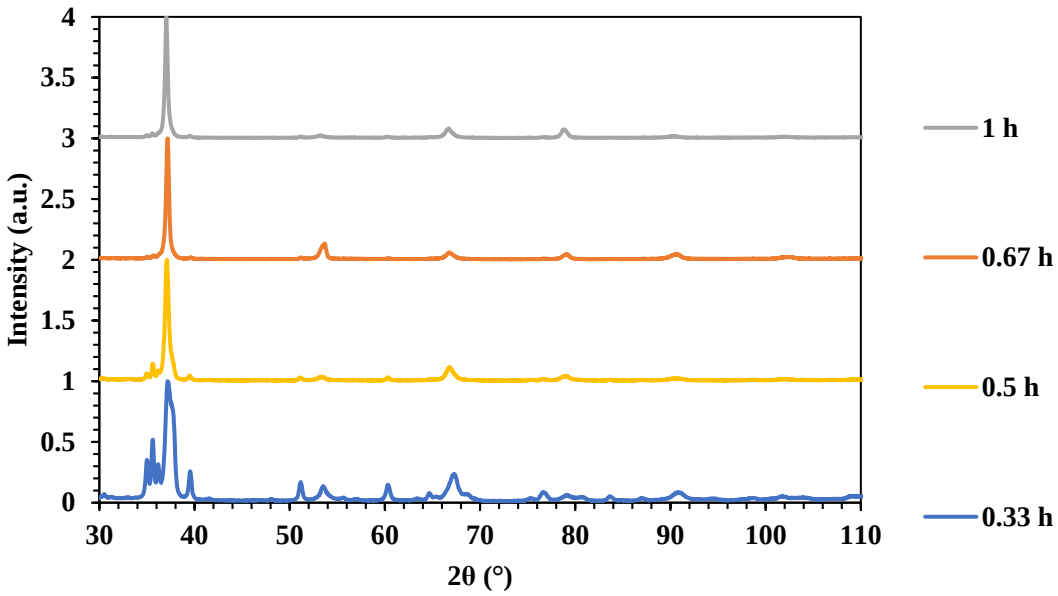

Figure 44. XRD patterns obtained from U10Mo disks decomposed at 500°C and recrystallized at 590°C from 0.33 to 1 h.

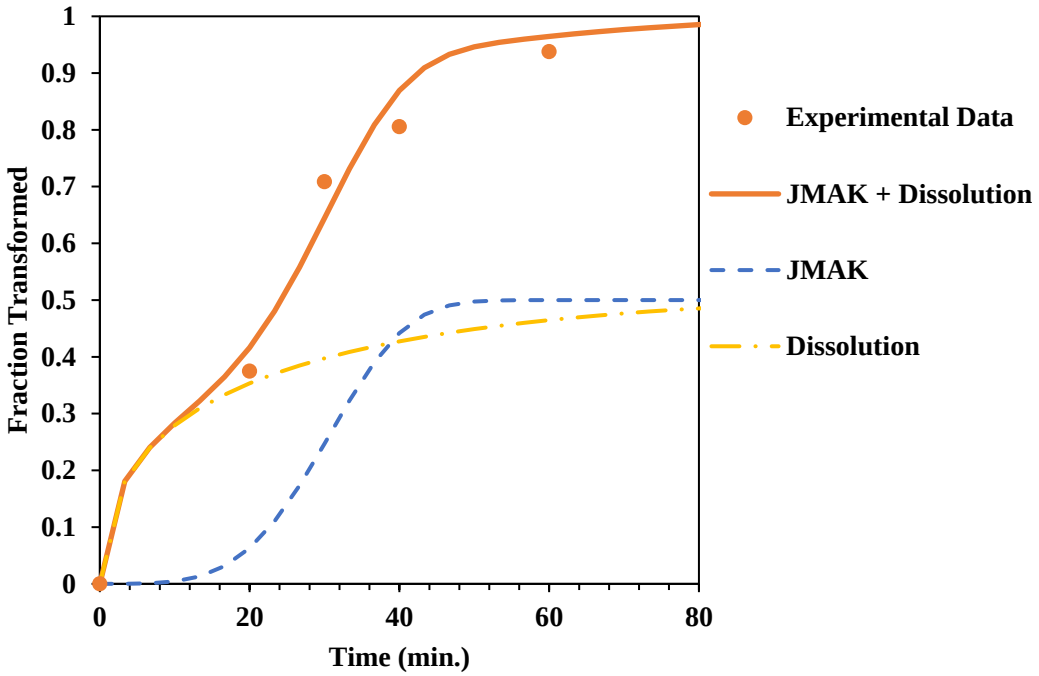

Figure 45. Fraction recrystallized γ as a function of annealing time at 590°C.

Table 6. Results of phase quantification using deconvolution of XRD patterns obtained from U10Mo decomposed at 500°C for 720 hours and recrystallized at 590°C.

t (h)	t (min.)	wt. % α	wt. % γ'	wt. % γ
0	0	36.7	63.3	0
0.33	20	27.6	35.0	37.4
0.5	30	14.9	14.3	70.8
0.67	40	1.6	17.9	80.5
1	60	2.5	3.7	93.8

The good fit at each of the aforementioned temperatures suggests that the provided model is suitable for describing the isothermal transformation from α+γ' to γ as a function of time given the appropriate boundary conditions. In conjunction with decomposition modeling, the phase constitution of the fuel may be approximated as a function of time and temperature throughout fabrication by using the appropriate parameters in the suggested model.

Furthermore, with the appropriate considerations, the approximation may be extended to include irradiation effects. To apply the model, the parameters must reflect the irradiation conditions, including the effects of irradiation temperature and irradiation-induced diffusion. However, irradiation in research and test reactors is typically done at relatively low temperatures (less than ~250°C) [25]. Consequently, with high fission rate/fission density, the conditions lie far above the critical fission rate shown in Figure 8, leading to irradiation-induced diffusion dominating the phase transformations observed in the fuel. As such, the thermal diffusivity is assumed to be negligible and the diffusivity thus applied is D_R, per Eq. (33) rather than D_T from Eq. (34). For modeling the behavior, average operating conditions are approximated using actual irradiation temperature and fission rate of 150°C and 5 x 10^{14} fissions/cm^3·s, respectively [125]. These parameters are reflected in the modeled behavior and compared with the results from heat treatments in Figure 46.

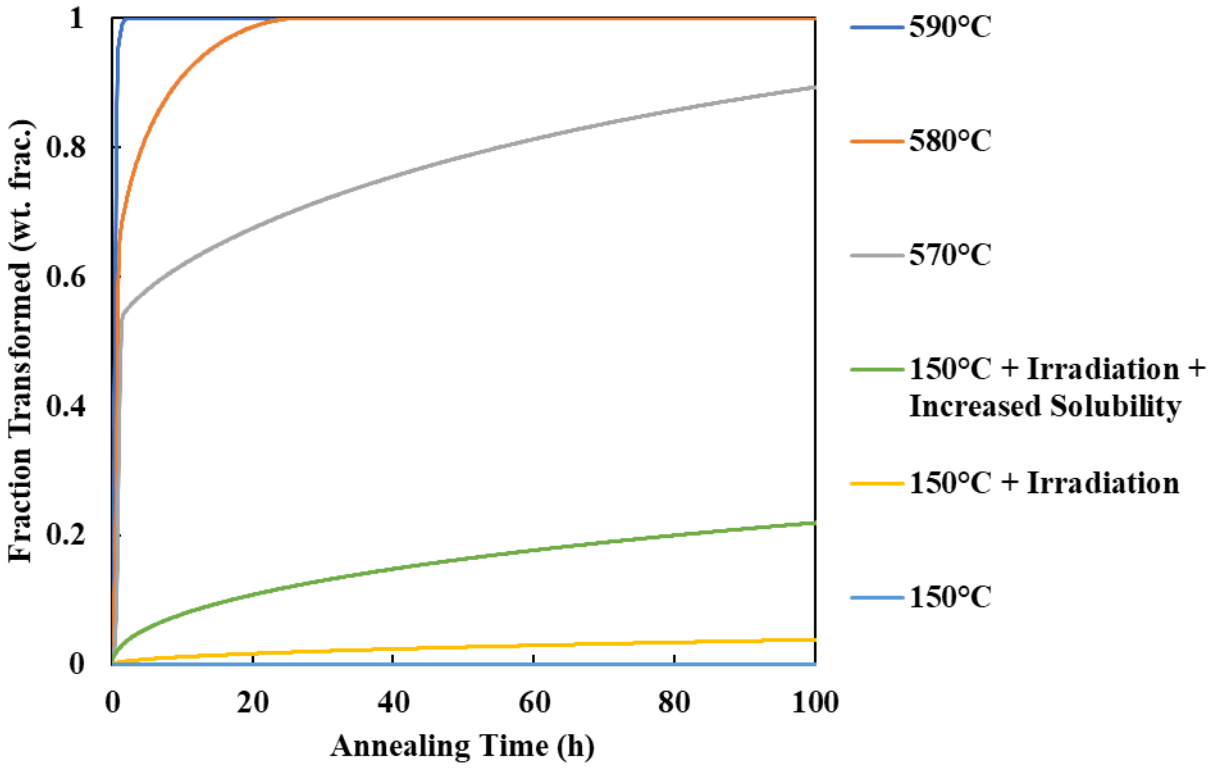

Figure 46. Modeled isothermal transformation kinetics of decomposed α+γ' to γ in U10Mo alloys as a function of time.

The modeled behavior in Figure 46 represents the fitted model for isothermal heat treatments done in this study, as well as an extension of the model to include the effects of low-temperature irradiation. The blue line labeled "150°C" represents the kinetics of the transformation considering only thermal effects, characterized by sluggish behavior. The yellow line labeled "150°C + Irradiation" incorporates D_R under the influence of 5 x 10^{14} fissions/cm^3·s. At 150°C, C_i cannot be directly taken from the solvus in the phase diagram and is thus approximated at only 22 at. %, assuming slight Mo enrichment at the interface compared to the concentration in the equilibrium γ matrix (away from dissolving particles). However, the chemical inhomogeneity after fabrication is still present following irradiation [126], suggesting that the interface concentration

(or Mo solubility limit in γ) may be increased under irradiation. The increased interface concentration is reflected in the green line labeled "150°C + Irradiation + Increased Solubility" in Figure 46, where C_i was increased to 28 at. % Mo. The parameters for each case shown in Figure 46 are summarized in Table 7.

Table 7. Summarized model parameters for reversion of decomposed U10Mo from α+γ' to γ.

T (°C)	N_o ($m^{-3}s^{-1}$)	G_o (m/s)	Q (kJ/mol)	C_e (at.% Mo)	C_i (at.% Mo)	C_p (at.% Mo)	D (m^2/s)
590	$3x10^7$	$3x10^7$	180	21	29	33	7.7×10^{-18}
580	$3x10^7$	$3x10^7$	180	21	24.5	33	5.7×10^{-18}
570	$3x10^7$	$3x10^7$	180	21	22	33	4.2×10^{-18}
150	$3x10^7$	$3x10^7$	180	21	22	33	2.7×10^{-25}
150 + Irradiation	$3x10^7$	$3x10^7$	180	21	22	33	1.6×10^{-14}
150 + Irradiation + Increased Solubility	$3x10^7$	$3x10^7$	180	21	28	33	1.6×10^{-14}

The modeled behavior incorporating irradiation induced diffusivity and increased Mo solubility suggests that the volume fraction transformed back to γ phase approaches 0.15 after about 36 h. The significance of this value (0.15) is that it represents roughly the extent of decomposition observed in the fuel plates following typical fabrication [87]. The results of this model suggest that the decomposed α+γ' may be reverted to γ following 36 h under the specific irradiation conditions.

5.4 Grain Growth in Reverted γ-U10Mo

The structure of the grains following γ reversion remains unknown in the U-Mo system. The size of the grains, however, plays a role in the swelling of the fuel plates during irradiation per Eq (36). To investigate how the grains are affected by decomposition and reversion,

homogenized U10Mo disks were decomposed at 500°C for 720 h then heat treated above the eutectoid temperature. The resulting grain structure will be analyzed and compared with that of the original γ grains following homogenization.

Following homogenization, the U10Mo disks were polished and analyzed with optical microscopy. The average measured diameter was 105.5 μm, and a representative image is shown in Figure 47. The black spots represent impurities, typically carbides, present in the disk.

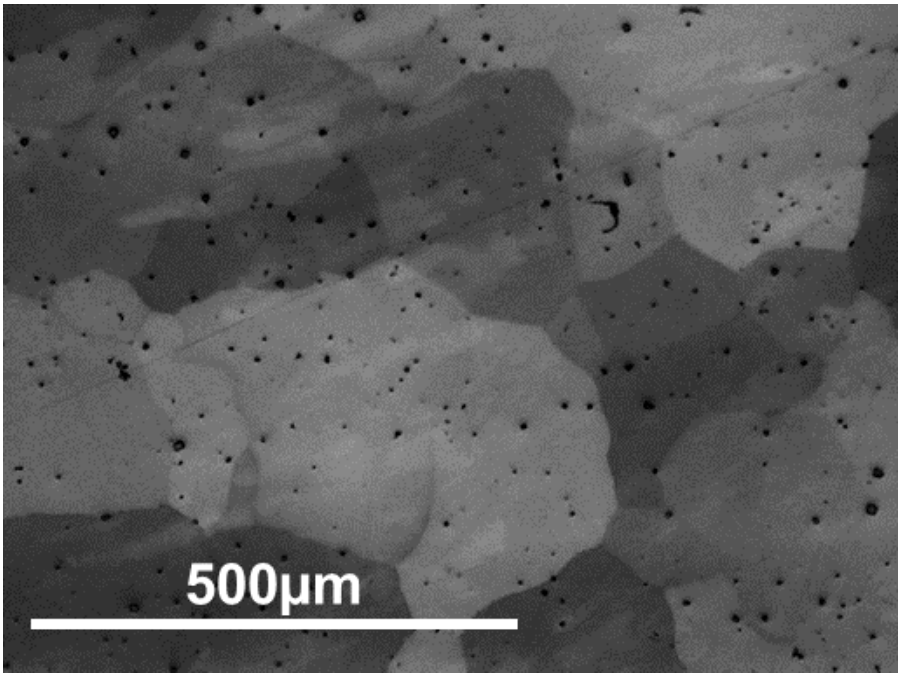

Figure 47. Contrast-enhanced optical micrograph showing the grains in a U10Mo disk homogenized at 800°C for 96 h.

The disks were then decomposed at 500°C for 720 h and subsequently heat treated at 600, 650, or 700 °C for 0.3, 2, and 24 h. Per the previous results, the decomposed microstructure is expected to quickly revert completely to γ. Following heat treatments, the disks were imaged using optical microscopy and the grain sizes were measured. At 700 and 650°C, the initial measured grain size was approximately 105.5 μm, yielding an approximate real grain diameter of 188 μm.

The resulting average grain sizes with standard deviations after heat treatment are shown in Figure 48.

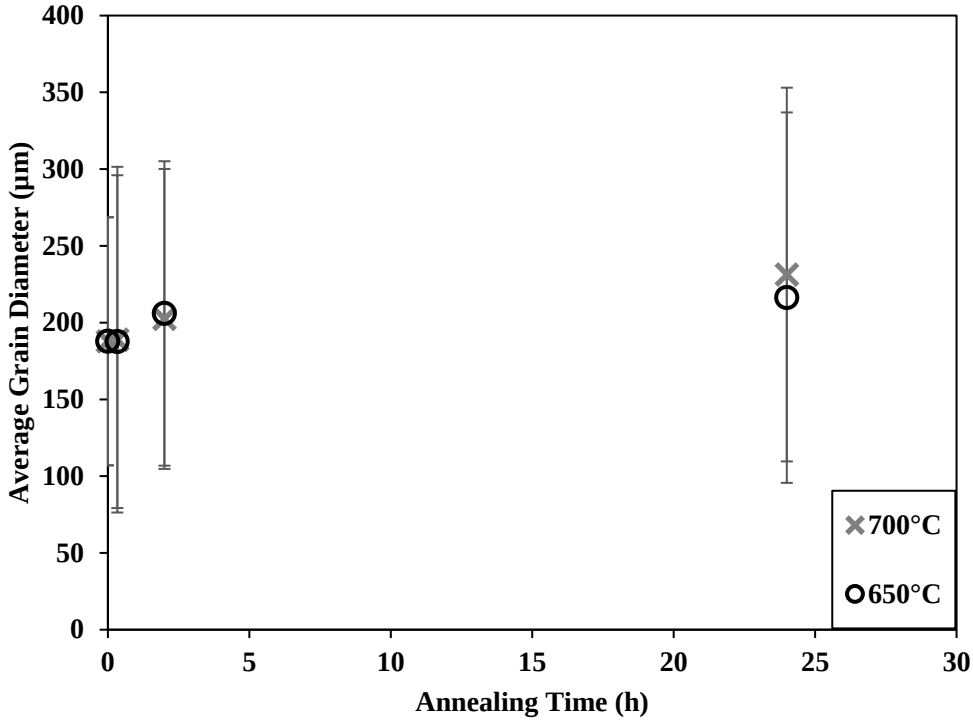

Figure 48. Grain size measurements in U10Mo disks following homogenizing, decomposition, and reversion heat treatment at 650 and 700°C as a function of time. 0 h represents the initial homogenized γ grain size.

It is evident in Figure 48 that the reverted γ grain size after 0.33 h does not significantly differ from that of the homogenized disks at either 650 or 700°C; the average diameter after homogenization is 188 µm compared with 188 and 189 µm following the 0.33 h heat treatment at 650 and 700°C, respectively. Furthermore, the optical micrograph in Figure 49 shows the grain structure in a U10Mo disk following 650°C 2 h heat treatment, revealing a similar grain structure to those observed in the homogenized disks. The dark-field micrograph in Figure 50 was taken at the same location as the bright-field micrograph in Figure 49 and shows the remnants of the

decomposed microstructure with artefacts of the DP boundaries remaining, forming a subgrain network without any orientation-based contrast observed using polarized light. The artefacts result from coarsened features that dissolved relatively slowly compared to the finer features that resulted from initial DP growth. The interfaces between DP colonies served as nucleation sites for DC and the subgrain network that remains is due to undissolved particles that were initially relatively coarse. The BSE micrograph in Figure 51 shows the remaining particles that make up the subgrain network following γ reversion heat treatment.

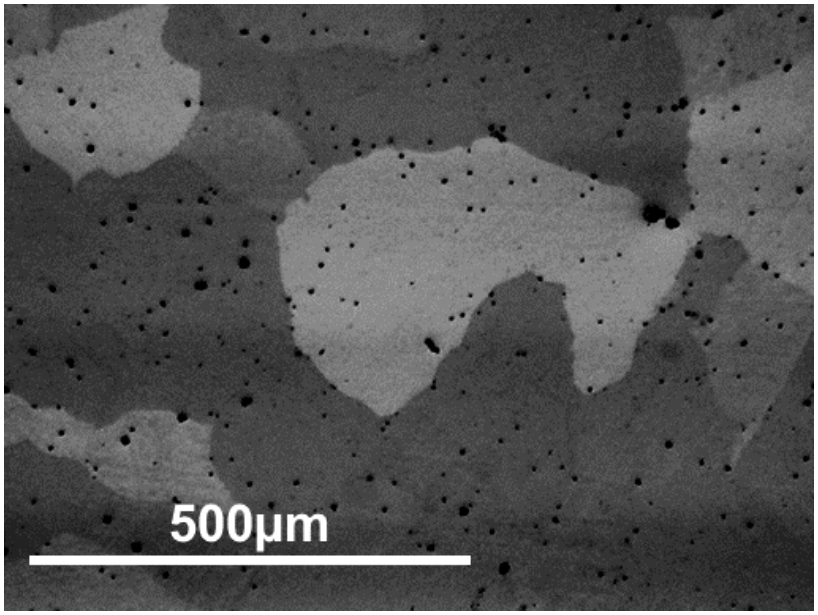

Figure 49. Optical micrograph of U10Mo disk following γ reversion heat treatment at 650°C for 2 h.

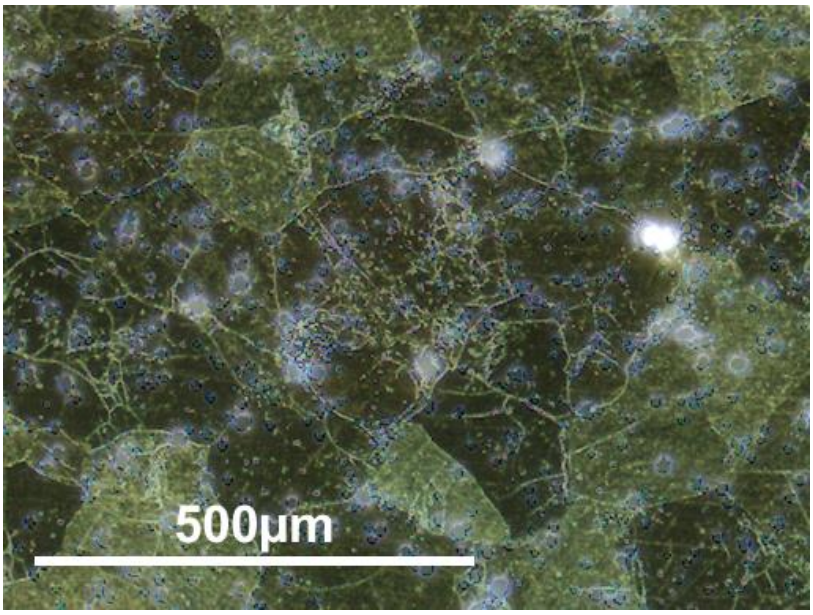

Figure 50. Dark-field optical micrograph of U10Mo disk following γ reversion heat treatment at 650°C for 2 h.

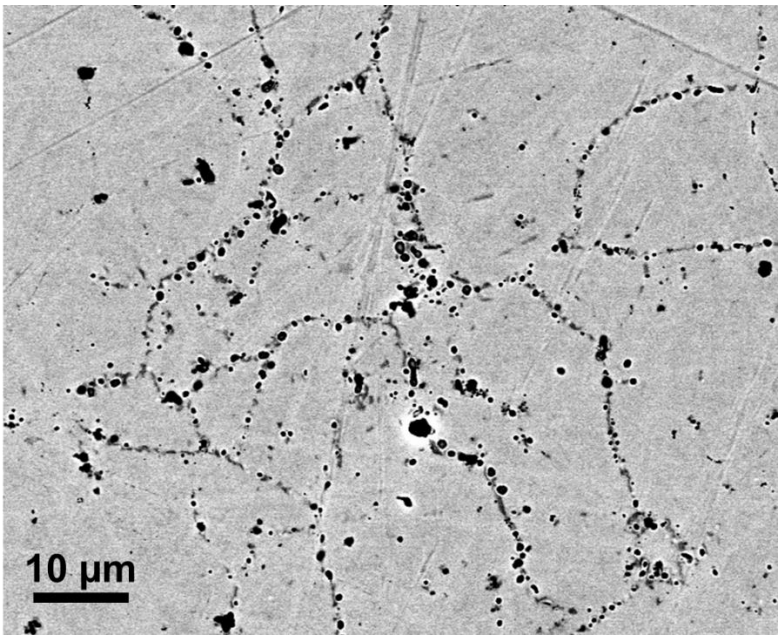

Figure 51. BSE micrograph showing the subgrain network of dissolving particles remaining from DC microstructure at initial DP boundaries.

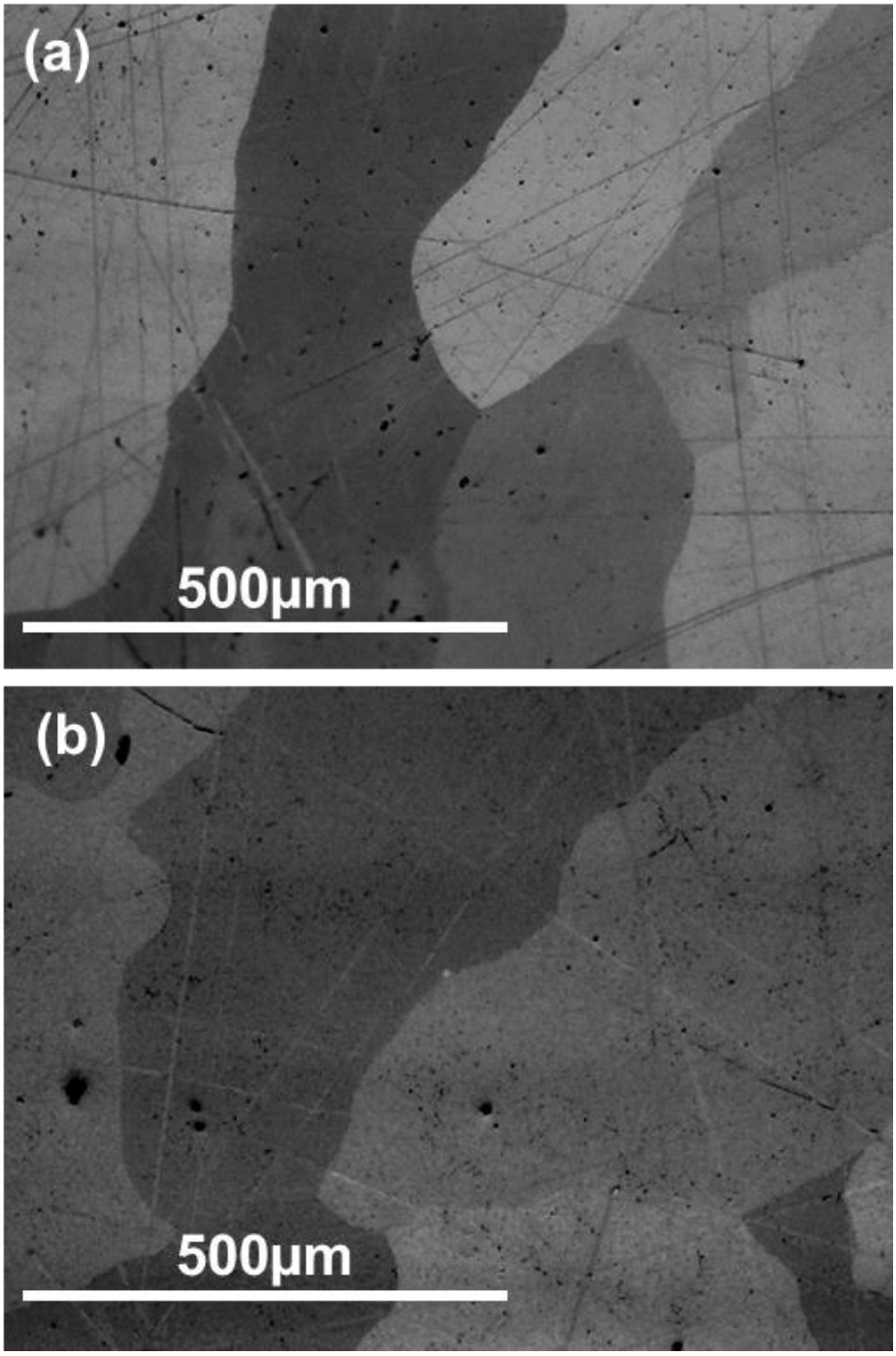

Figure 52. Optical micrograph of a U10Mo disk (a) after homogenization and (b) after decomposition and reversion heat treatment, suggesting that the overall size and morphology of the original γ grains remain unaffected throughout decomposition and reversion.

To investigate the results in a disk with originally large, elongated grains, a separate set of U10Mo disks with larger grains was decomposed and heat treated for γ reversion. Following the reversion heat treatment at 600°C, the optical micrograph in Figure 52 indicates that the γ grains remained large and elongated, demonstrating that the reverted γ grain structure is not significantly refined in comparison to the original γ grains in U10Mo prior to decomposition (in the absence of deformation). Similar grain "memory" has been shown in the Fe-Mn binary system; transformation from the face-centered cubic (FCC) γ phase (austenite) to BCC α (ferrite), then back to austenite results in reversion to the to the original austenite grain structure if the γ→α transformation occurs above a critical temperature around 600-650°C [127].

The grain size can be modeled as a function of time using Eq. (31). Assuming normal grain growth, the grain growth exponent *n* is equal to 2. However, the growth of the large grains observed in the disk heat-treated at 600°C cannot be assessed with any accuracy due to the small number of grains that can be counted. As a result, the grain growth is only modeled at two temperatures in this study: 650 and 700°C. Consequently, the pre-exponential factor and grain growth in Eq. (32) cannot be fitted and well-defined. Consequently, an activation energy is of 172.4 kJ/mol is assumed [79]; this value is similar to the activation energy for bulk diffusion in U10Mo [105]. The pre-exponential factor is then fitted at approximately 6×10^8 $\mu m^2/s$, which falls between the two values reported in grain growth data for U-Mo alloys [79, 80]. The modeled data is shown in Figure 53. The large standard deviations and limited data give rise to uncertainty in the grain growth model and further investigation in necessary to provide an accurate model and description of grain growth in U10Mo.

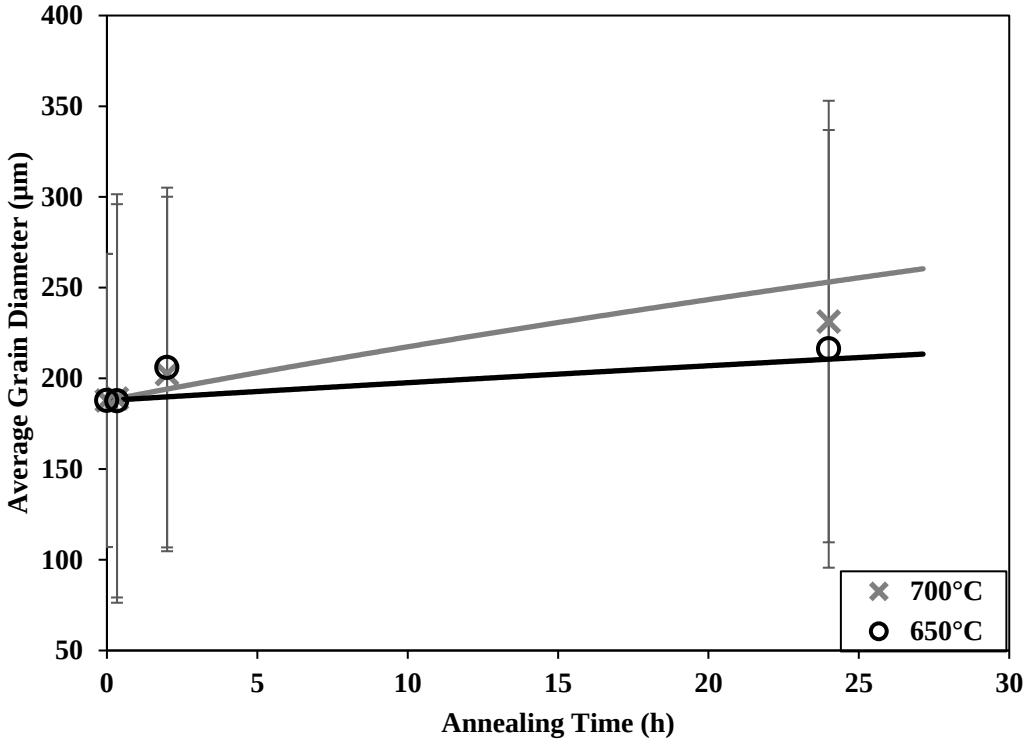

Figure 53. Experimental and modeled grain growth in U10Mo disks annealed at 650 and 700°C.

CHAPTER 6: NANOINDENTATION OF PHASES RELEVANT TO MONOLITHIC FUEL PLATES

Chapter 6 was originally published in *Journal of Nuclear Materials*. Newell, R., Park, Y., Mehta, A., Keiser, D., & Sohn, Y. (2017). Mechanical properties examined by nanoindentation for selected phases relevant to the development of monolithic uranium-molybdenum metallic fuels. *Journal of Nuclear Materials*, vol. 487, pp. 443-452 [128].

During fabrication, the fuel, barrier, and cladding materials interact leading to a variety of reaction products present in the fuel plates. Figure 54 presents microstructure of various phases observed in HIP fuel plate and diffusion couples. For better statistical averaging of mechanical properties, bulk phases were subjected to large numbers of indents. However, as reported in Table 8, only a limited number of indents was possible on the phases that were present as precipitates/discontinuous layers. Thus, for UC, UZr_2, and Mo_2Zr phases, only indents completely and clearly within the phase were included for analysis. Table 8 reports hardness and reduced modulus determined using Eq. (38) and Eq. (39) from the indentation, along with Young's modulus estimated based on Eq. (40). Poisson's ratio for each of the phase required for the estimation of Young's modulus was taken from various references [129-133], while an assumed value of 0.3 was employed for UZr_2 and Mo_2Zr due to lack of data in literature.

Table 8. Hardness, reduced modulus, and elastic modulus for the phases examined.

Phase	***N***	***H* (GPa)**	***E*$_r$ (GPa)**	***v***	***E* (GPa)**	**Ref. *E* (GPa)**	**Ref.**
$(Al,Si)_3Zr$	20	11.4 ± 0.85	173.3 ± 4.71	0.3	183.6 ± 4.30	-	assumed
Al_3Zr	80	11.2 ± 1.28	206.0 ± 15.4	0.18	239.6 ± 15.1	201.8 ~ 210.6	[129, 130]
UZr_2	65	5.4 ± 0.20	126.7 ± 1.9	0.3	128.6 ± 1.73	-	Assumed
Mo_2Zr	15	13.0 ± 1.11	157.7 ± 9.5	0.3	164.7 ± 8.71	-	Assumed
α-U	90	4.7 ± 0.10	169.0 ± 3.2	0.21	187.4 ± 3.07	208	[131]
γ-U(Mo) Solid Solution	1000	2.29 ± 0.11 ~ 4.42 ± 0.21	63.3 ± 3.6 ~ 104.6 ± 3.08	0.35	58.6 ± 3.17 ~ 97.0 ± 3.12	50.1~ 94.7	[132]
UC	12	4.65 ± 0.05	112.8 ± 4.7	0.284	114.2 ± 4.29	243	[133]

The $(Al,Si)_3Zr$ phase developed in the monolithic fuel plate at the diffusion barrier-cladding interface, and had a hardness of 11.6 ± 0.90 GPa and a reduced modulus of 164.0 ± 8.3 GPa, based on indentations shown in Figure 55. It should be noted that the large indents in the AA6061 and Zr surfaces are close together, and were not included in any analysis, as the deformation from one indent may interfere with the adjacent one. The $(Al,Si)_3Zr$ phase in HIP plates has been crystallographically identified previously by Perez *et* al. [99] as tI16.

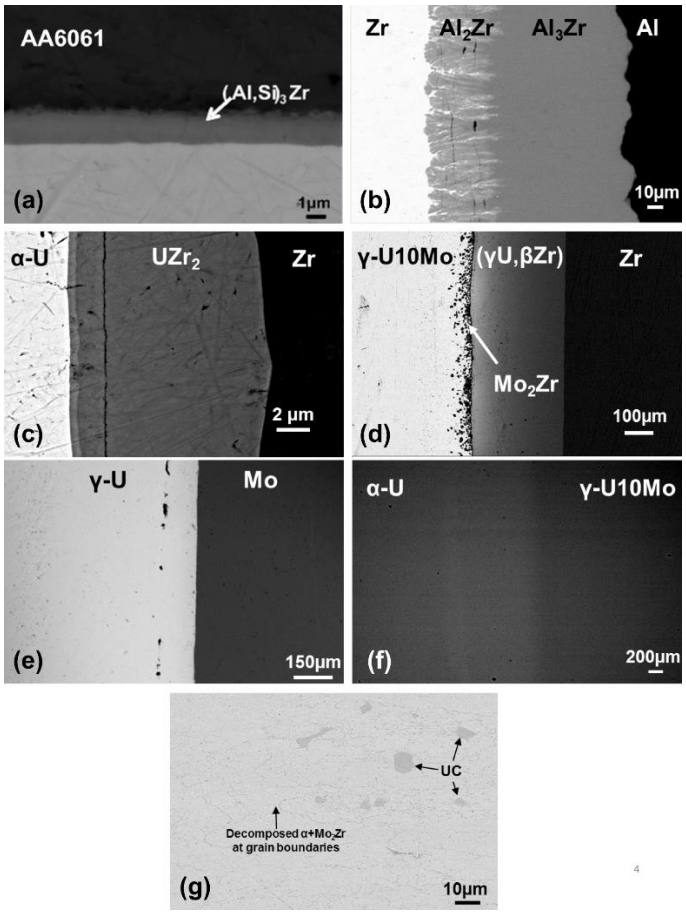

Figure 54. Various phases observed throughout the typical HIP fuel plates. Phases of interest form at interfaces between (a) Zr and AA6061, (b) Zr and Al, (c) α-U and Zr, (d) γ-U10Mo and Zr, (e) γ-U10Mo and Mo, (f) α-U and γ-U10Mo, and (g) within the γ-U10Mo fuel.

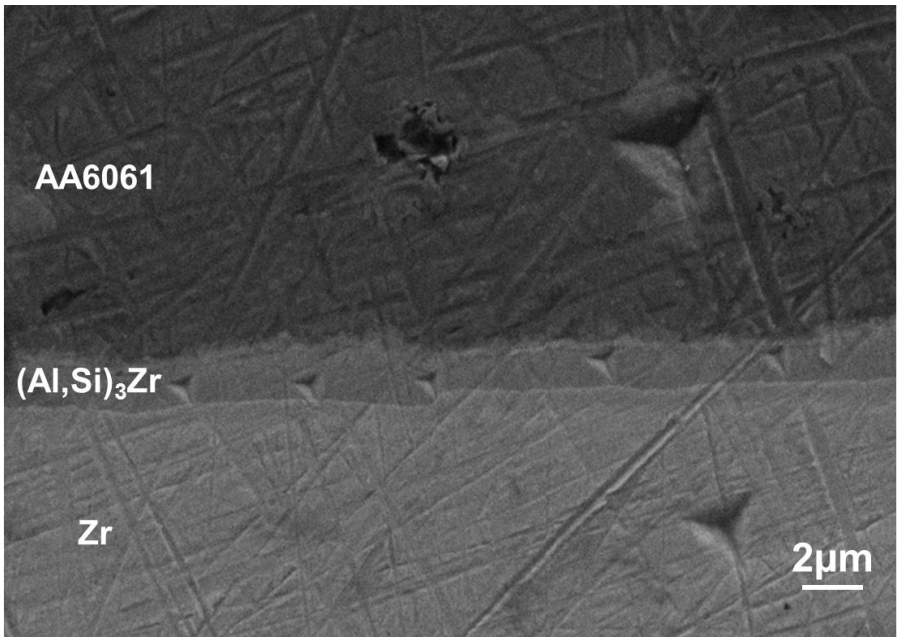

Figure 55. Interdiffusion zone developed at Zr/AA6061 interface, showing indentations on the Al, Zr, and $(Al, Si)_3Zr$ phases.

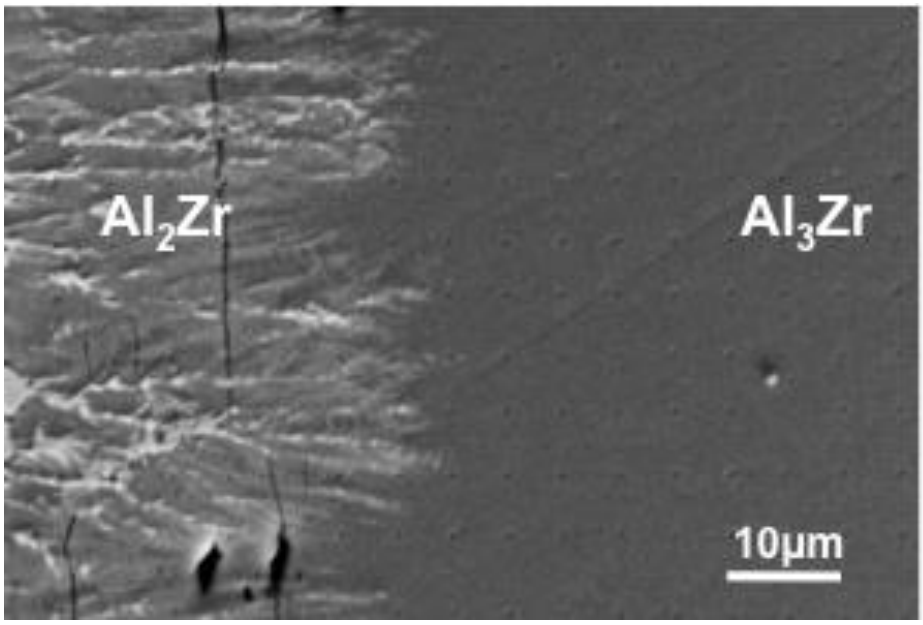

Figure 56. Indentation on Al_3Zr phase developed in Al-Zr diffusion couple annealed at 425°C for 720 h.

Since the $(Al,Si)_3Zr$ phase in the HIP plate sample was relatively thin (< 3 μm), an Al vs. Zr diffusion couple was examined, where the Al_3Zr phase was developed to a thickness of approximately 77.3 μm. According to literature, this phase may exhibit a metastable $L1_2$ crystal structure [134], or a $D0_{23}$ crystal structure, which is described as the stable structure [135-137]. The diffusion couple investigated in this study was annealed at 425ºC and water quenched, producing the stable $D0_{23}$ crystal structure. A hardness of 11.2 ± 1.28 GPa and a reduced modulus of 206.0 ± 15.4 GPa were obtained for the Al_3Zr phase based on indentations shown in Figure 56. The estimated Young's modulus of 206 GPa is close to the 210 GPa determined by first principle calculations [130] as reported in Table 8. Due to inhomogeneous microstructural development, results obtained from the Al_2Zr phase could not be analyzed with any certainty. Both phases are not only potentially relevant in the cladding-diffusion barrier interaction in monolithic fuel plates, but also in lightweight structural materials [129, 138].

A complex interaction occurs between the U10Mo fuel and Zr diffusion barrier. The primary constituents, according to HIP plate characterization, include UZr_2 and Mo_2Zr [99]. The UZr_2 phase developed adjacent to the Zr diffusion barrier although in sizes and quantities too small for reliable and statistically confident indentation results. Consequently, the UZr_2 phase was grown in a diffusion couple and is shown in Figure 57. The crystal structure of UZr_2 is a C32 type structure, following the AlB_2 prototype [139, 140]. Based on indentation presented in Figure 57, a hardness of 5.4 ± 0.20 GPa and a reduced modulus of 126.7 ± 1.9 GPa were obtained for the UZr_2 phase.

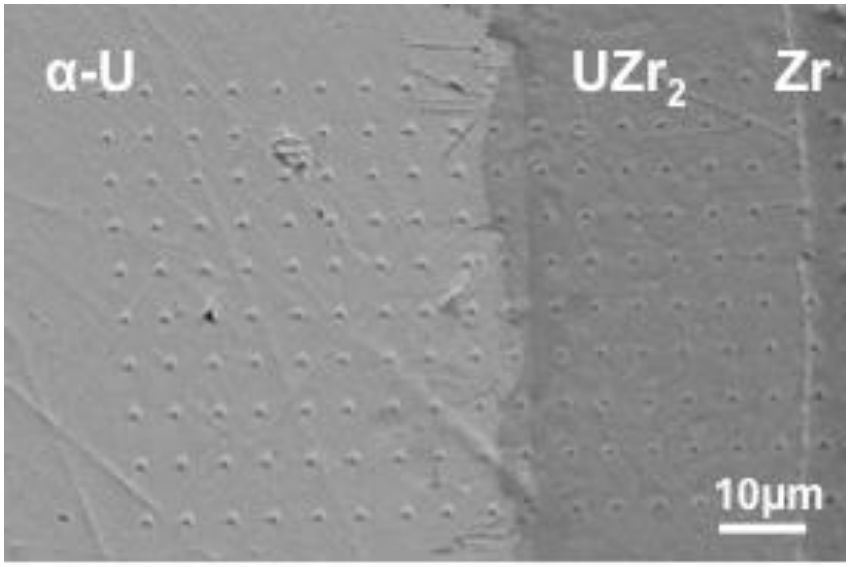

Figure 57. Indentation on α-U and UZr_2 phases developed in U-Zr diffusion couple annealed at 580°C for 360 h.

Due to the interdiffusion and reaction between U10Mo fuel and Zr diffusion barrier, Mo_2Zr and Mo-depleted α-U have been observed to develop at the interface. The Mo_2Zr phase was fabricated in larger amounts in diffusion couples in order to study microstructural evolution and kinetics in the U-Mo-Zr system [141]. Even in diffusion couples, Mo_2Zr phase did not develop into a continuous layer, but indentation was carefully carried out to assess the properties as indicated by the red circles in Figure 58. Mo_2Zr, a C15 Laves phase [142], possessed a hardness of 13.0 ± 1.11 GPa and reduced modulus of 157.7 ± 9.5 GPa as reported in Table 8.

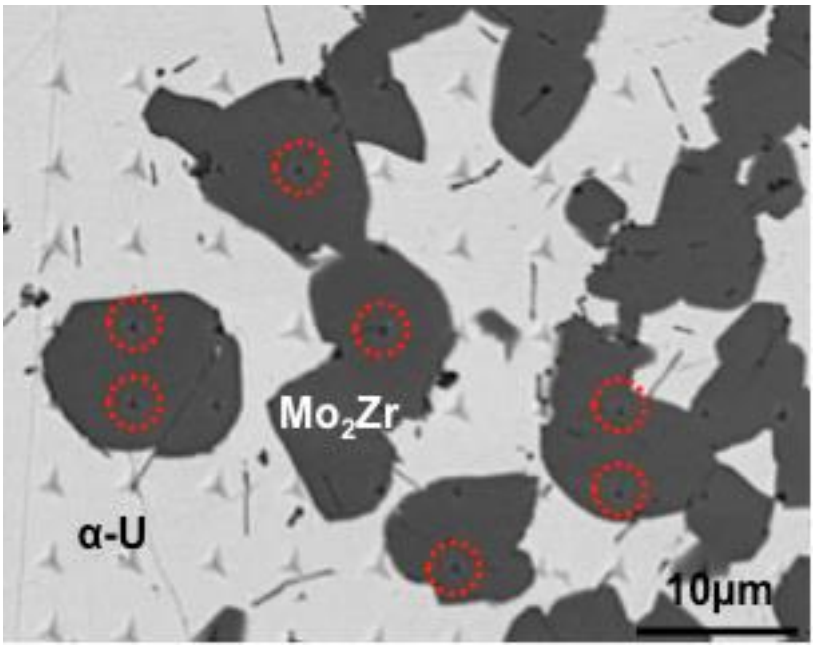

Figure 58. Indentation on Mo_2Zr precipitates that formed in the interdiffusion zone of a U10Mo-Zr diffusion couple annealed at 800°C for 480 h.

With the formation of Mo_2Zr, the Mo-depleted γ-phase transforms to α-U with negligible Mo solubility in the fuel plate samples. In this study, indentation results for the α-U were also obtained from the U vs. Zr annealed at 580ºC for 360 hours, sufficiently away from any interdiffusion and reaction, at the terminal end of U metal. Hardness and reduced modulus of α-U were obtained as 4.7 ± 0.1 GPa and 169.0 ± 3.2 GPa, respectively, as reported in Table 8. Results reported were carefully gathered to avoid any influence of inclusions (e.g., oxide, carbides, etc.) occasionally found in pure U metals. The Young's modulus estimated using Eq. (40) for α-U was lower than that reported by tensile testing [143] by approximately 10%.

From the diffusion couples, U vs. Mo [105] and U vs. U-10 wt. % Mo, indentation testing was carried out as a function of Mo concentration. Composition-dependent Young's modulus and hardness obtained from U vs. Mo diffusion couple through nanoindentation are presented in Figure 59.

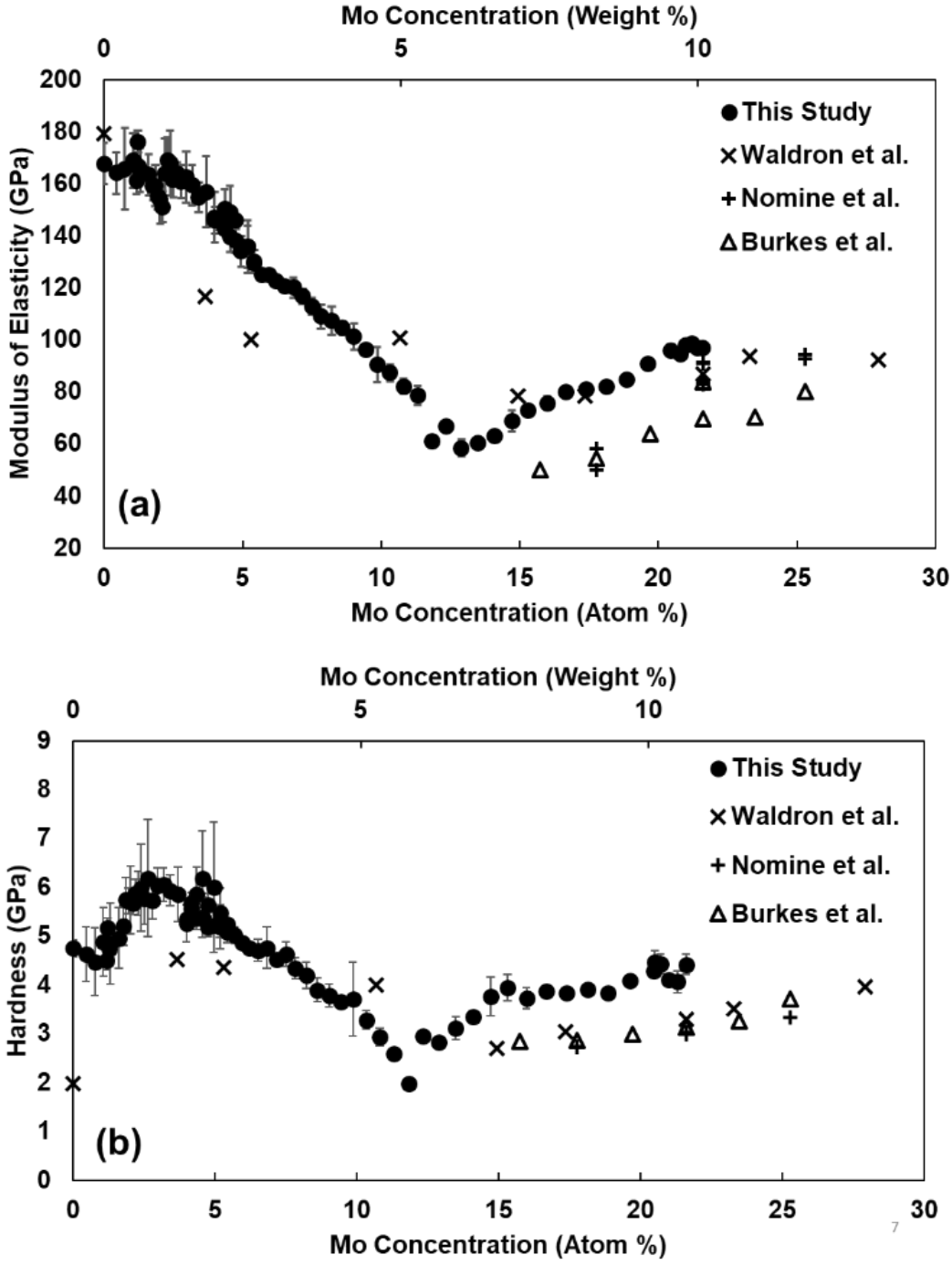

Figure 59. (a) Elastic modulus and (b) hardness of U solid solution as a function of Mo concentration in U-U10Mo diffusion couple annealed at 1000°C for 24 h.

Results from nanoindentation on U vs. U-10 wt. % Mo diffusion couples and U vs. Mo diffusion couples were nearly identical both in magnitude and trend. The properties of U-Mo alloys have been the subject of several investigations [37, 75, 132], and their results are presented in Figure 59 for comparison. The hardness values from literature presented in Figure 59 have been converted from VHN to GPa by multiplying the reported values by 0.0987 [144]. The U-Mo solid solution in the diffusion couple exhibited Young's modulus in good agreement with those observed by tensile testing at several compositions, including 97.0 GPa at 10 wt. % Mo in the diffusion couple compared to 86.9 GPa at 10 wt. % Mo reported by Waldron *et* al. [132].

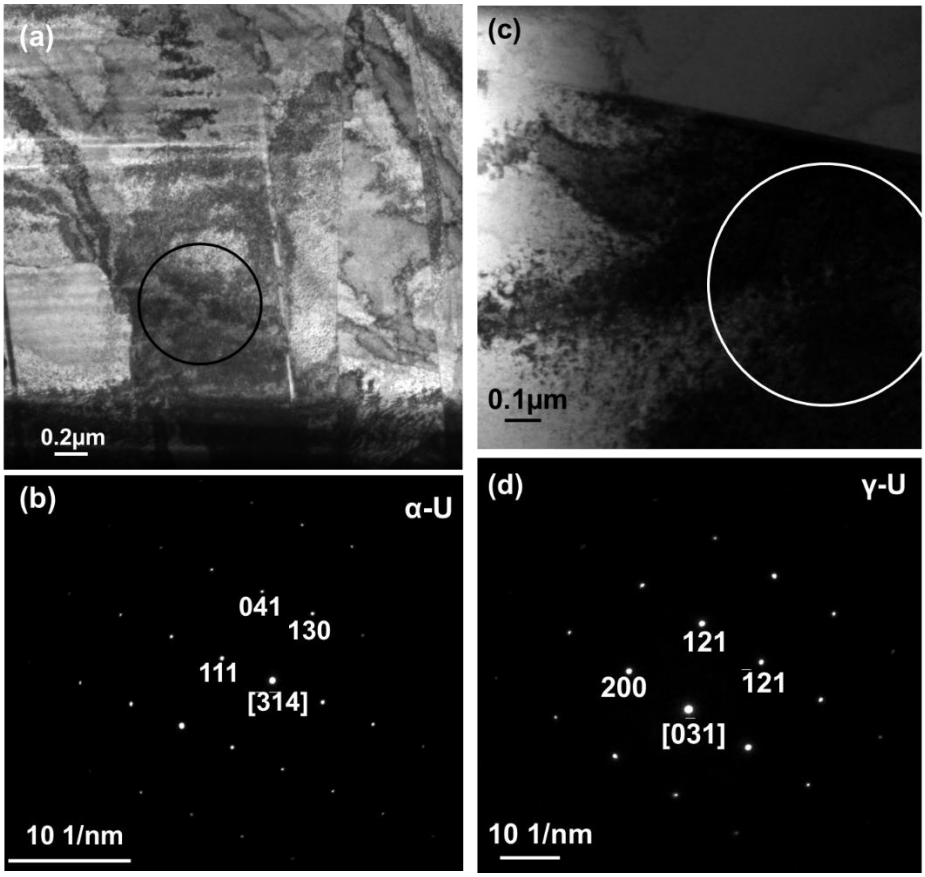

Figure 60. (a) Bright-field micrograph and (b) corresponding SAED pattern from α-U, demonstrating the orthorhombic structure and (c) bright-field micrograph and (d) corresponding SAED pattern from γ-U10Mo, demonstrating the BCC structure.

Young's modulus decreased with an increase in Mo content from 0 to approximately 6 wt. %, and then increased with a further increase in Mo content as shown in Figure 59a. The initial decrease in modulus can be attributed to increasing stabilization of the more compliant γ-phase, as the amount of stabilized γ-phase is expected to increase with increased Mo content. Within the stabilized γ-phase having Mo content higher than 6 wt. %, Mo in substitutional solid solution would lead to increased hardness and modulus as presented in Figure 59. However, this simple phase mixture may not be sufficient in explaining the composition-dependent hardness presented in Figure 59b. While a relative minimum in hardness (~2 GPa) was observed at approximately 6 wt. % Mo similar to the modulus, a relative maximum (~6 GPa) was also observed around 2 wt. % Mo.

Figure 60a and b present a bright-field micrograph and the corresponding SAED from the TEM sample with negligible Mo content (E = 169.3 ± 12.8 GPa and H = 5.72 ± 0.76). The pure U end was completely α, indicating that no γ-phase was retained upon quenching from 1000ºC. At the other terminal end, the TEM sample with the composition of U-10 wt. % Mo consisted entirely of γ-phase, demonstrating that the BCC structure was stabilized completely and no transformation took place upon cooling after diffusion anneal. The γ-phase with the composition of U-10 wt. % Mo had reduced modulus and hardness values of approximately 95 GPa and 4 GPa, respectively, as shown in Figure 59.

Additional samples having approximate compositions of approximately 6 wt. % and 2 wt. % Mo were prepared for TEM analyses. The sample with 6 wt. % Mo, according to Figure 59, corresponds to composition where relative minima in reduced modulus (63.3 ± 3.6 GPa) and hardness (2.29 ± 0.11 GPa) were observed. As shown in Figure 61, TEM analyses demonstrated the presence of BCC γ-phase with additional reflections corresponding to (½ ½ 1) planes. Similar

reflections have been reported as a superlattice structure U_3Mo [145]. The microstructure of the TEM sample with 2 wt. % Mo was complex as presented in Figure 62. As seen by both bright- and dark-field micrographs, needle-like features typical of martensitic transformations were prevalent, which have been observed and documented in the U-Mo system [43, 146-148].

As mentioned, the elastic modulus determined as a function of composition presented in Figure 59 may be mostly attributed to the mixture of phases and variation in compositions within these phases. Figure 63a presents a result from a semi-quantitative analysis carried out to understand the influence of phase mixture and solid solutioning on the composition-dependent Young's modulus observed in this study.

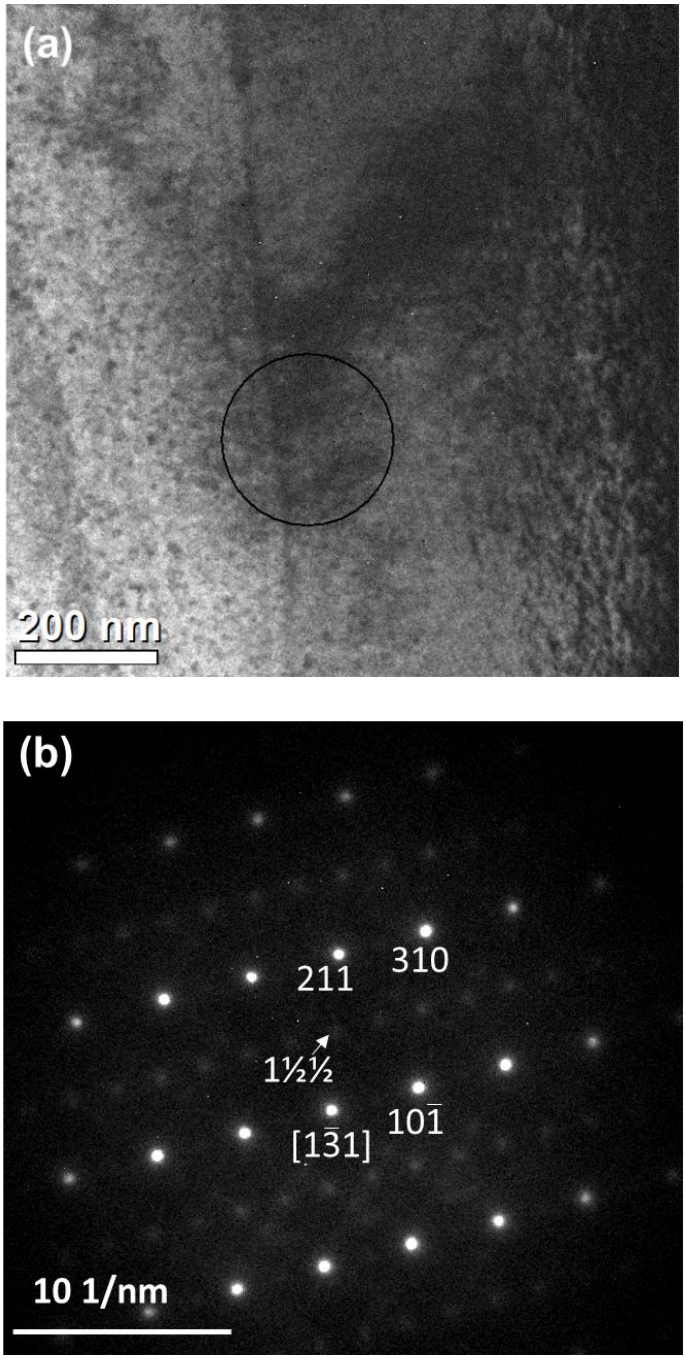

Figure 61. (a) Bright field micrograph and (b) the corresponding SAED pattern from the U-5.4 wt. % Mo sample, exhibiting the BCC structure characteristic of γ-uranium with additional reflections corresponding to (½ ½ 1) planes.

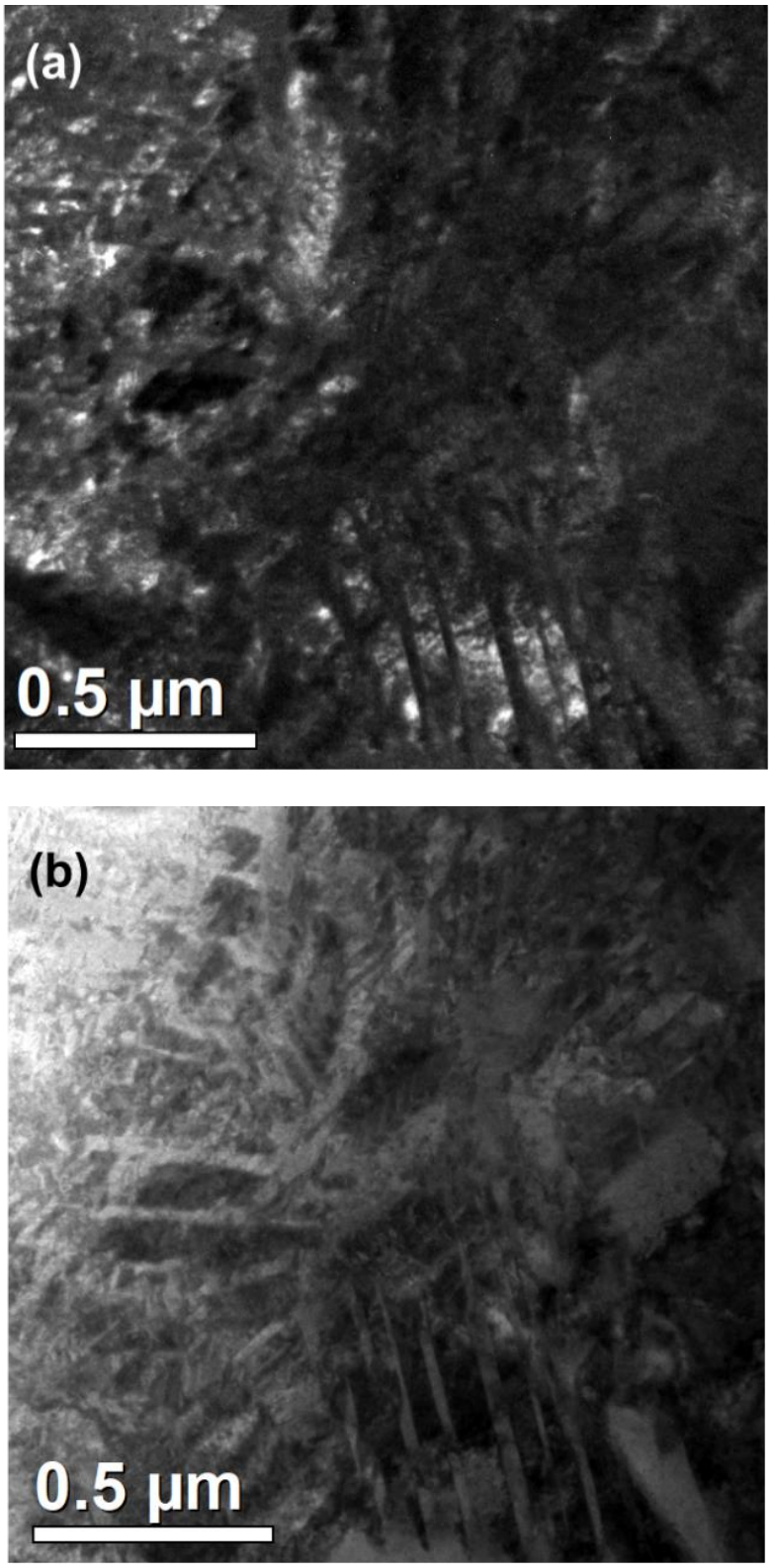

Figure 62. (a) Bright- and (b) dark-field micrographs from the sample with U-2.0 wt. % Mo.

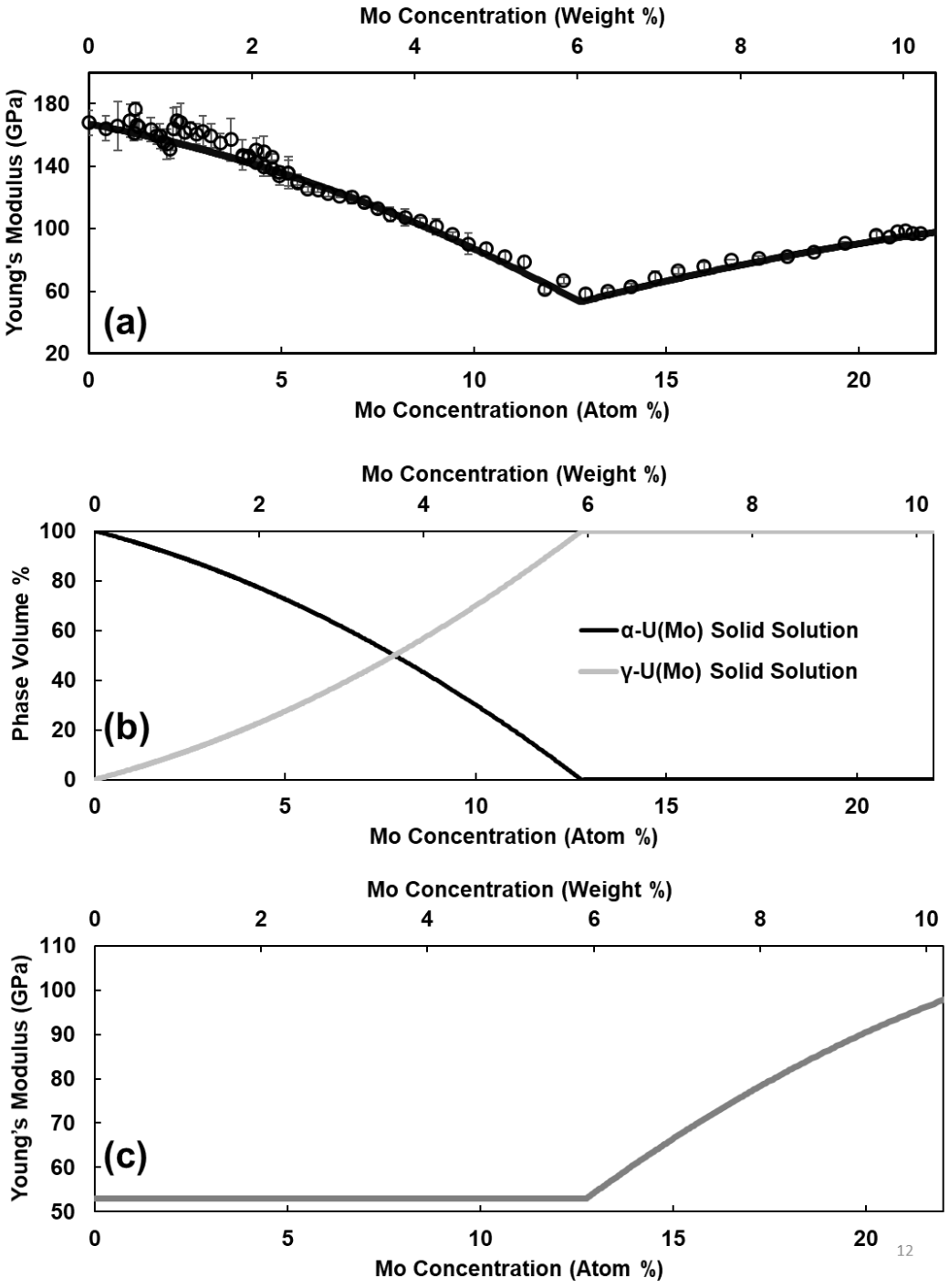

Figure 63. (a) Calculated composition-dependent reduced modulus based on (b) mixture of α and γ-phases and (c) solid solutioning within the γ-phase.

The elastic modulus of α-U can be assumed as a constant value of 180 GPa [132, 149] due to insignificant Mo solubility, less than 1 at. % [36]. For the γ-phase with Mo content less than 6 wt. %, mechanical properties are not readily available from experimentation since the γ-phase is not easily retained at room temperature. The lowest elastic modulus for the γ-phase has been reported as 50.1 GPa at approximately 7 wt. % Mo [75]. This value has been applied as the elastic modulus of γ-phase with compositions at 6 wt. % Mo where a minimum modulus value was observed, and TEM analysis revealed a completely retained γ-phase. The mixture of α and γ phases was modeled as presented in Figure 63b to "best-fit" the composition-dependent Young's modulus as shown in Figure 63a for the composition less than 6 wt. % Mo. For composition with more than 6 wt. % Mo, an increase in modulus was "best-fit" as shown in Figure 63a based on an assumption of solid solutioning within the γ-phase as presented in Figure 63c. While the phase mixture and solid-solutioning may not completely explain the composition-dependence of hardness shown in Figure 59b, agreement presented in Figure 63 is close.

Occasionally, inclusions are found in U10Mo fuel alloys, prominently in the form of uranium carbide (UC) as seen in Figure 54g. Crystallographic identification and their influence on the fuel fabrication were previously reported [23]. Figure 64 presents a typical array of indentations performed on inclusions, and Table 8 reports the hardness (4.65 ± 0.05 GPa) and reduced modulus (112.8 ± 4.7 GPa) determined from indentations that were clearly within the carbide phase. Fine cellular precipitates in Figure 15 are on-set of γ-to-α phase transformation, and not the inclusion phases. Young's modulus for the UC is estimated at 114.2 ± 4.29 GPa which is significantly lower than 243 GPa reported in literature [133, 150, 151]. This difference may arise due to stoichiometric deviation and/or geometric limitation (e.g., indentation on thin or shallow oxide/carbide phase) inherent in indentation testing.

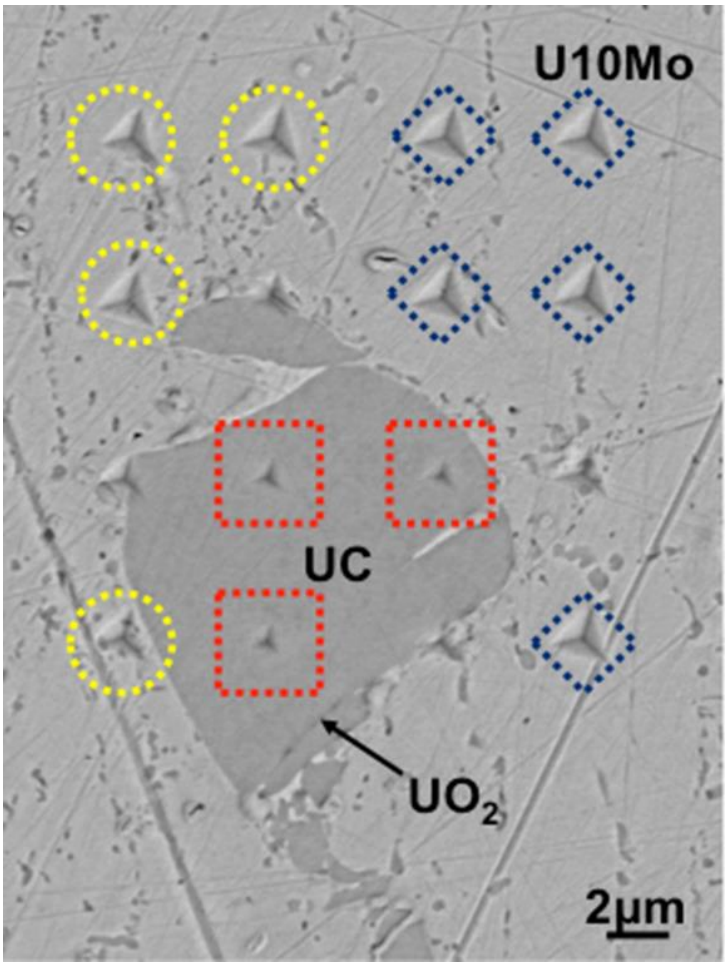

Figure 64. Indentations on U10Mo fuel in monolithic fuel plate (HIP processed at 560°C for 180 minutes), including near decomposed regions and on UC inclusion. The red dotted squares indicate indents on the UC phase, the blue diamonds on the γ-phase, and the yellow circles on a mixture γ and decomposed α and γ'.

CHAPTER 7: SUMMARY AND CONCLUSIONS

7.1 Zr Diffusion Barriers

The physical characteristics of the Zr diffusion barriers are outlined in Table 9. Physical characteristics observed in Zr diffusion barriers fabricated via electroplating, plasma spraying, and roll bonding.. The major differences among samples and groups are described below.

- The samples with RB diffusion barriers displayed the most uniform thickness, as well as the lowest combination of inclusions, pores, and cracks. The RB samples were nearly free of defects but contained a small amount of δ-$ZrH_{1.5}$ inclusions.
- The EP diffusion barriers were largely prone to cracking as a result of a high concentration of δ-$ZrH_{1.5}$ in the diffusion barrier.
- The PS samples exhibited the highest degree of porosity and inclusions.
- The interdiffusion zones between the fuel and RB diffusion barriers were consistent with those found in literature, containing α-U, Mo_2Zr, and UZr_2.
- The EP samples did not exhibit extensive interdiffusion throughout the fuel-barrier interface, however, the well-developed areas were consistent with those in RB samples with additional F-enriched regions observed in EP samples as result of the fluoride-based plating electrolyte.
- The PS samples exhibited an interdiffusion zone that consisted primarily of UO_2.
- The edge coverage of EP and PS samples was largely characterized by cracking and non-uniformity.

Following AA6061 cladding via HIP, the RB diffusion barriers exhibit the least defects of the three application methods investigated here. Their demonstrated history of good performance

coupled with their more homogeneous and predictable microstructure observed in this study support the use of roll-bonding in the fabrication of monolithic LEU fuel plates.

Table 9. Physical characteristics observed in Zr diffusion barriers fabricated via electroplating, plasma spraying, and roll bonding.

Sample ID	Fabrication Method	Thickness (μm)	CV^2	Cracks (Linear %)	Pores/ Inclusions (area %)	Major defect type
DUM911	EP	9.6 ± 4.2	0.19	30.0	0	Cracking
DUM912	EP	19.7 ± 7.9	0.16	37.1	0	Cracking
DUM913	EP	8.1 ± 4.3	0.27	43.6	0	Cracking
DUM914	EP	4.0 ± 1.7	0.17	80.2	0	Delamination
DUM915	PS	26.8 ± 12.5	0.22	10.6	9.9	Pores
DUM916	PS	21.7 ± 9.2	0.18	20.7	15.9	Pores
DUM926	RB	25.1 ± 6.6	0.07	0	0	None
DUM927	RB	20.5 ± 5.5	0.07	0	0	None
DUM941	RB	28.7 ± 6.6	0.05	0	2.2	Hydrides
DUM942	RB	23.3 ± 5.3	0.05	1.7	1.3	Hydrides

7.2 Isothermal Phase Transformations in U10Mo Alloy

U10Mo disks were homogenized at 800°C for 96 h, resulting in a homogeneous microstructure of γ-U10Mo. The disks were subsequently decomposed at 500°C for times ranging from 240 to 1,200 h. The decomposition of γ initiated via two mechanisms: discontinuous or cellular precipitation along grain boundaries and inclusions and continuous precipitation within the grains as γ’ needles. Further annealing at 500°C resulted in lengthening and widening of the CP needles and growth of the DP colonies into the grains. After 720 h, the DP colonies had completely consumed the continuous γ matrix. After prolonged annealing, discontinuous coarsening was observed along grain boundaries, inclusions, and DP colony interfaces. The DC microstructure was characterized by coarsened α+γ’ lamella extending from initiation sites toward the grain interior.

As the continuous γ matrix was consumed after 720 h, this was selected as the initial condition for investigating the kinetics of reversion to a continuous γ microstructure. Decomposed disks were annealed at 570, 580, and 590°C for varying time resulting in the α+γ' → γ transformation. The reference intensity ratio approach was applied to XRD patterns obtained from the heat-treated disks to quantify the amount of γ present. A combinatorial kinetic model consisting of the classical JMAK nucleation and growth and spherical particle dissolution mechanisms was employed to describe the α+γ' → γ transformation as a function of time and temperature. Furthermore, the model was hypothetically extended to include irradiation-induced diffusion to describe the phase reversion that occurs during in-reactor operation.

Following γ decomposition and reversion at 600, 650, and 700°C, the γ grains were analyzed and compared with those of the homogenized disks to determine whether the grains were refined as a result of the heat treatments, as has been reported in other alloy systems following similar phase transformations. The resulting grains in the U10Mo disks, however, were similar in size and morphology to those observed prior to decomposition and reversion heat treatment, suggesting that the grains revert to their original configuration.

7.3 Nanoindentation of Phases Relevant to LEU Monolithic Fuel Plates

Hardness and reduced modulus of several intermetallic and solid solution phases relevant to the fabrication process of monolithic fuel plate were investigated by nanoindentation using HIP'ed fuel plates and diffusion couples. A hardness of 11.2 ± 1.28 GPa and a reduced modulus of 206.0 ± 15.4 GPa were obtained for the Al_3Zr phase from Al vs. Zr diffusion couple annealed at 425ºC for 720 hours. Reduction in hardness, 11.4 ± 0.85 GPa and reduced modulus, 173.3 ± 4.71 GPa was observed for the $(Al,Si)_3Zr$ phase in the HIP plate sample from the interaction of Zr

and AA6061 cladding alloy through HIP at 560ºC for 3 hours. The UZr_2, Mo_2Zr, and Mo-depleted α-U developed due to the interdiffusion and reaction between U-10Mo fuel and Zr diffusion barrier. Hardness of these phases were, in GPa, 5.4 ± 0.20, 13.0 ± 1.11, 4.7 ± 0.10, respectively, and reduced modulus of these phases were, in GPa, 126.7 ± 1.9, 157.7 ± 9.5, 169.0 ± 3.2, respectively. The U-Mo solid solution exhibited decreasing reduced modulus from pure U to approximately 6 wt. % Mo, followed by increasing modulus with increasing Mo content up to 10 wt. %. This behavior was semi-quantitively modeled by mixture of α- and γ-phases from pure U to 6 wt. % Mo, followed by solid solutioning within the γ-phase from 6 wt. % to 10 wt. % Mo. The properties reported for these phases can lead to a better understanding regarding the mechanical behavior of the entire fuel plate and help model the fabrication process and irradiation behavior.

7.4 Overall Conclusions

The data presented in this study can be used to model and improve fabrication of LEU monolithic fuel plates. Through examining the fuel plates following different Zr application methods, the resulting microstructure can be understood prior to HIP, and with the results of various modeling efforts, the microstructure and physical properties of the overall fuel plate can be estimated following HIP. Furthermore, ongoing efforts to model the mechanical response of fuel plates to fabrication and irradiation require accurate input of microstructural and mechanical properties of the constituents of monolithic fuel plates. After modeling and simulation efforts become refined and verified, the operating environment of LEU monolithic fuel plates can be simulated to promote safe and effective operation of nuclear reactors while eliminating the use of weapons-usable HEU in power generation applications.

APPENDIX: LIST OF PUBLICATIONS AND PRESENTATIONS

Journal Publications

1. **Newell, R.**, Park, Y., Mehta, A., Keiser, D., & Sohn, Y. (2017). Mechanical properties examined by nanoindentation for selected phases relevant to the development of monolithic uranium-molybdenum metallic fuels. *Journal of Nuclear Materials, 487,* 443-452.

2. **Newell, R.**, Mehta, A., Park, Y., Sohn, Y., Jue, J., & Keiser, D. (2017). Relating diffusion couple experiment results to observed as-fabricated microstructures in low-enriched U-10wt.% Mo monolithic fuel plates. *Defect and Diffusion Forum, 375,* 18-28.

3. **Newell, R.**, Mehta, A., Park, Y., Keiser, D., & Sohn, Y. (2017). Interdiffusion, reactions, and phase transformations observed during fabrication of low enriched uranium monolithic fuel system for research and test reactors. *Defect and Diffusion Forum, 383,* 10-16.

4. Park, Y., Eriksson, N., **Newell, R.**, Keiser, D., & Sohn, Y. (2016). Phase decomposition of γ-U (bcc) in U-10 wt.% Mo fuel alloy during hot isostatic pressing of monolithic fuel plate. *Journal of Nuclear Materials, 480,* 271-280.

5. Davis, B., Dabrow, D., **Newell, R.**, Miller, A., Schueller, J. K., Xiao, G., Liang, S., Hartwig, K., Ruzycki, N., Sohn, Y., & Huang, Y. (2018). Chip Morphology and Chip Formation Mechanisms During Machining of ECAE-Processed Titanium. *Journal of Manufacturing Science and Engineering, 140(3),* 031008.

6. Park, Y., **Newell, R.**, Mehta, A., Keiser, D., & Sohn, Y. (2018). Interdiffusion and reaction between U and Zr. *Journal of Nuclear Materials, 502,* 42-50.

7. Mehta, A., Eriksson, N., **Newell, R.,** Zhou, L., Shulz, E., Sprowes, W., Betancor, F., Park., Y., Keiser, D., & Sohn, Y. (2018). Phase Transformations and Microstructural Development in the U-10 wt.% Mo Alloy with Varying Zr Content After Heat Treatments Relevant to the Monolithic Fuel Plate Fabrication Process. *Metallurgical and Materials Transaction A,* Submitted.

Conference Presentations

1. Newell, R., Keiser, D., & Sohn, Y., (2016, February). Mechanical properties of materials and phases relevant to monolithic U-Mo fuel system. Materials and Fuels for Current and Advanced Nuclear Reactors V – Fuels IV Symposium, TMS 2016, Nashville, TN.

2. Newell, R., Park, Y., Mehta, A., Keiser, D., & Sohn, Y. (2017, February). Reduced modulus and hardness of uranium-molybdenum solid solution as a function of Mo composition and related phase transformation. Materials and Fuels for Current and Advanced Nuclear Reactors VI – Fuels II Symposium, TMS 2017, San Diego, CA.

3. Park, Y., **Newell, R.**, Mehta, A., Keiser, D., & Sohn, Y. (2017, February). Interdiffusion and reaction between U and Zr. Materials and Fuels for Current and Advanced Nuclear Reactors VI – Fuels II Symposium, TMS 2017, San Diego, CA.

4. Newell, R., Park, Y., Keiser, D., & Sohn, Y. (2018, March). Isothermal transformation kinetics of γ phase from α+γ' phase mixture in U-10 wt.% Mo alloys. Materials and Fuels for Current and Advanced Nuclear Reactors VII – Fuels I Symposium, TMS 2018, Phoenix, Az.

5. Newell, R., Wang, Z., Arias, I., Mehta, A., Sohn, Y., & Florczyk, S. (2018, April). Direct contact cytotoxicity evaluation of CoCrFeNi-based high entropy alloys. SFB 2018, Atlanta, GA.

6. **Newell, R**., Mehta, A., Park, Y., Keiser, D., & Sohn, Y. (2018, October). Microstructural characteristics of Zr diffusion barriers applied via plasma spraying, electroplating, and co-rolling in low enriched U-10 wt.% Mo monolithic fuel plates after HIP. NuMat 2018, Seattle, WA.

REFERENCES

[1] International Energy Agency, *World Energy Outlook 2016*.

[2] International Energy Agency, *World Energy Outlook 2011*.

[3] United States Energy Information Administration, "International Energy Outlook" 2016.

[4] www.rertr.anl.gov, 2017.

[5] International Atomic Energy Agency, *IAEA Safeguards Glossary*. 2002.

[6] G. H. Lander, E. S. Fisher, and S. D. Bader, "The solid-state properties of uranium A historical perspective and review," *Advances in Physics,* vol. 43, pp. 1-111, 1994.

[7] J. L. Snelgrove, R. F. Domagala, G. L. Hofman, T. C. Wiencek, G. L. Copeland, R. W. Hobbs, and R. L. Senn, *The use of U_3Si_2 dispersed in aluminum in plate-type fuel elements for research and test reactors*: Argonne National Laboratory, 1987.

[8] J. P. Durand and Y. Fanjas, "LEU fuel development at CERCA," 1994.

[9] J. L. Snelgrove, G. L. Hofman, M. K. Meyer, C. L. Trybus, and T. C. Wiencek, "Development of very-high-density low-enriched-uranium fuels," *Nuclear Engineering and Design,* vol. 178, pp. 119-126, 1997.

[10] D. D. Keiser Jr, S. Hayes, M. K. Meyer, and C. Clark, "High-density, low-enriched uranium fuel for nuclear research reactors," *Journal of Materials,* vol. 55, pp. 55-58, 2003.

[11] E. Wilson, A. Bergeron, J. Stillman, T. Heltemes, D. Jaluvka, and L. Jamison, "US High Performance Research Reactor Conversion Program: An Overiciew on Element Design." Argonne National Laboratory.

[12] R. Newell, A. Mehta, Y. J. Park, Y. H. Sohn, J. F. Jue, and D. D. Keiser Jr, "Relating Diffusion Couple Experiment Results to Observed As-Fabricated Microstructures in Low-Enriched U-10wt.% Mo Monolithic Fuel Plates," in *Defect and Diffusion Forum*, 2017, pp. 18-28.

[13] K. Huang, Y. J. Park, D. D. Keiser Jr, and Y. H. Sohn, "Interdiffusion Between Zr Diffusion Barrier and U-Mo Alloy," *Journal of Phase Equilibria and Diffusion*, vol. 33, pp. 443-449, 2012.

[14] K. Huang, C. C. Kammerer, D. D. Keiser Jr, and Y. H. Sohn, "Diffusion Barrier Selection from Refractory Metals (Zr, Mo and Nb) Via Interdiffusion Investigation for U-Mo RERTR Fuel Alloy," *Journal of Phase Equilibria and Diffusion,* vol. 35, pp. 146-156, 2013.

[15] J. F. Jue, B. H. Park, C. R. Clark, G. A. Moore, and D. D. Keiser Jr, "Fabrication of monolithic RERTR fuels by Hot Isostatic Pressing," *Nuclear Technology,* vol. 172, pp. 204-210, 2010.

[16] J. F. Jue, D. D. Keiser Jr, C. R. Breckenridge, G. A. Moore, and M. K. Meyer, "Microstructural characteristics of HIP-bonded monolithic nuclear fuels with a diffusion barrier," *Journal of Nuclear Materials*, vol. 448, pp. 250-258, 2014.

[17] J. F. Jue, D. D. Keiser Jr., F. Di Lemma, T. Trowbridge, J. Madden, A. Wilson, B. Rabin, "Characterization of Alternative Zr Coatings on U-Mo Monolithic Fuel Foils," Idaho National Laboratory, 2017.

[18] C. S. Barrett, M. H. Mueller, and R. L. Hitterman, "Crystal Structure Variations in Alpha Uranium at Low Temperatures," *Physical Review,* vol. 129, pp. 625-629, 1963.

[19] E. S. Fisher and H. J. McSkimin, "Low-Temperature Phase Transition in Alpha Uranium," *Physical Review,* vol. 124, pp. 67-70, 1961.

[20] L. T. Lloyd and C. S. Barrett, "Thermal expansion of alpha uranium," *Journal of Nuclear Materials,* vol. 18, pp. 55-59, 1966.

[21] A. C. Roberts and A. H. Cottrell, "Creep of alpha uranium during irradiation with neutrons," *Philosophical Magazine,* vol. 1, pp. 711-717, 1956.

[22] S. F. Pugh, "Swelling in alpha uranium due to irradiation," *Journal of Nuclear Materials,* vol. 4, pp. 177-199, 1961.

[23] B. Hudson, K. H. Westmacott, and M. J. Makin, "Dislocation loops and irradiation growth in alpha uranium," *Philosophical Magazine,* vol. 7, pp. 377-392, 1962.

[24] R. V. Hesketh, "A possible mechanism of irradiation creep and its reference to uranium," *Philosophical Magazine,* vol. 7, pp. 1417-1420, 1962.

[25] M. K. Meyer, J. Gan, J. F. Jue, D. D. Keiser Jr, E. Perez, A. Robinson, D. M. Wachs, N. Woolstenhulme, G. L. Hofman, and Y. S. Kim, "Irradiation Performance of U-Mo Monolithic Fuel," *Nuclear Engineering and Technology,* vol. 46, pp. 169-182, 2014.

[26] M. K. Meyer, T. C. Wiencek, S. L. Hayes, and G. L. Hofman, "Irradiation behavior of U6Mn–Al dispersion fuel elements," *Journal of Nuclear Materials,* vol. 278, pp. 358-363, 2000.

[27] G. L. Hofman, R. F. Domagala, and G. L. Copeland, "Irradiation behavior of low-enriched U6Fe-Al dispersion fuel elements," *Journal of Nuclear Materials,* vol. 150, pp. 238-243, 1987.

[28] C. S. Yoo, H. Cynn, and P. Söderlind, "Phase diagram of uranium at high pressures and temperatures," *Physical Review B,* vol. 57, pp. 10359-10362, 05/01/ 1998.

[29] G. L. Hofman, M. K. Meyer, and A. E. Ray, "Design of high density gamma-phase uranium alloys for LEU dispersion fuel applications," in *Proceedings of the 1998 International Reduced Enrichment for Test Reactor Conference,* 1998.

[30] R. Van Thyne and D. McPherson, "Transformation kinetics of uranium-molybdenum alloys," *Transactions of the American Society of Metals,* vol. 49, pp. 598-621, 1957.

[31] P. Repas, R. Goodenow, and R. Hehemann, "Transformation characteristics of U-Mo and U-Mo-Ti alloys," *Transactions of the American Society of Metals,* vol. 57, 1964.

[32] H. Saller, F. Rough, and A. Bauer, "Transformation kinetics of Uranium-Molybdenum alloys," Battelle Memorial Institutue, Columbus, Ohio, 1954.

[33] T. A. Pedrosa, A. M. M. dos Santos, F. S. Lameiras, P. R. Cetlin, and W. B. Ferraz, "Phase transitions during artificial ageing of segregated as-cast U–Mo alloys," *Journal of Nuclear Materials,* vol. 457, pp. 100-117, 2015.

[34] S. Parida, S. Dash, Z. Singh, R. Prasad, and V. Venugopal, "Thermodynamic studies on uranium–molybdenum alloys," *Journal of Physics and Chemistry of Solids,* vol. 62, pp. 585-597, 2001.

[35] V. Sinha, G. Prasad, P. Hegde, R. Keswani, C. Basak, S. Pal, and G. P. Mishra, "Development, preparation and characterization of uranium molybdenum alloys for dispersion fuel application," *Journal of Alloys and Compounds,* vol. 473, pp. 238-244, 2009.

[36] V. Sinha, P. Hegde, G. Prasad, G. Dey, and H. Kamath, "Effect of molybdenum addition on metastability of cubic γ-uranium," *Journal of Alloys and Compounds,* vol. 491, pp. 753-760, 2010.

[37] D. E. Burkes, T. Hartmann, R. Prabhakaran, and J. F. Jue, "Microstructural characteristics of DU–xMo alloys with x = 7–12 wt%," *Journal of Alloys and Compounds,* vol. 479, pp. 140-147, 2009.

[38] E. Brandes, G. Brook, and P. Paufler, "Smithells Metals Reference Book." Butterworth-Heinemann Ltd., Oxford, 1993.

[39] D. Ahmann, A. Snow, and A. Wilson, "The Uranium-Molybdenum Binary System," Iowa State Coll., Ames1945.

[40] A. Seybolt and L. Stark, "Uranium Alloy Development Part VI. Uranium-Molybdenum Alloys." Los Alamos Scientific Laboratory, New Mexico, 1944.

[41] J. Lehmann, "A study of phase transformations processes in 0, 5 to 4% mo uranium-molybdenum alloys," 1959.

[42] A. Harding and M. Waldron, "Transformations in uranium alloys with high solute solubility in the BCC γ phase. Part 1. Preliminary observations on the banded structures produced by non-equilibrium transformations in uranium alloys," United Kingdom Atomic Energy Authority. Atomic Energy Research Establishment, Harwell, Berks, England, 1958.

[43] K. Tangri and G. Williams, "Metastable phases in the uranium molybdenum system and their origin," *Journal of Nuclear Materials,* vol. 4, pp. 226-233, 1961.

[44] M. Steiner, E. Garlea, J. Creasy, A. DeMint, and S. Agnew, "Temperature dependent elastic properties of γ-phase U–8 wt% Mo," *Journal of Nuclear Materials,* vol. 500, pp. 184-191, 2018.

[45] Y. Goldstein and A. Bar-Or, "Decomposition of Gamma Phase in Uranium Alloys Containing 8, 10.8, and 14.3 wt. Percent Molybdenum," Israel Atomic Energy Commission, Tel-Aviv, Israel, 1967.

[46] A. Shoudy, W. McHugh, and M. Silliman, "The Effect of Irradiation Temperature and Fission Rate on the Radiation Stability of the Uranium-10 Wt.% Molybdenum Alloy," in *Radiation Damage in Reactor Materials. Part of the Proceedings of the Symposium on Radiation Damage in Solids and Reactor Materials*, 1963.

[47] F. Giraud-Heraud, J. Guillaumin, and R. Sifferlen, "Continuous and discontinuous precipitation in U-1.5 Mo alloys," *Journal of Nuclear Materials,* vol. 36, pp. 315-321, 1970.

[48] G. H. May, "The annealing of a quenched uranium-5 at % molybdenum alloy," *Journal of Nuclear Materials,* vol. 7, pp. 72-84, 1962.

[49] S. Jana, A. Devaraj, L. Kovarik, B. Arey, L. Sweet, T. Varga, C. Lavender, and V. V. Joshi, "Kinetics of cellular transformation and competing precipitation mechanisms during sub-eutectoid annealing of U10Mo alloys," *Journal of Alloys and Compounds,* vol. 723, pp. 757-771, 2017.

[50] B. Verlinden, J. Driver, I. Samajdar, and R. D. Doherty, "Chapter 7 Phase transformations," in *Pergamon Materials Series*. vol. 11, Pergamon, 2007, pp. 127-150.

[51] E. Hornbogen, "Systematics of the cellular precipitation reactions," *Metallurgical Transactions,* vol. 3, pp. 2717-2727, 1972.

[52] I. Manna, S. Pabi, and W. Gust, "Discontinuous reactions in solids," *International Materials Reviews,* vol. 46, pp. 53-91, 2001.

[53] G. Beghi, "Gamma Phase Uranium-Molybdenum Fuel Alloys. EUR 4053," 1968.

[54] T. C. Duong, "Integrated Computational Materials Science and Engineering for The Research and Development of Gen-IV Metallic Fuels: Application to Uranium-Niobium," 2015.

[55] J. D. Robson, "Modeling competitive continuous and discontinuous precipitation," *Acta Materialia,* vol. 61, pp. 7781-7790, 2013.

[56] S. Jana, N. Overman, T. Varga, C. Lavender, and V. V. Joshi, "Phase transformation kinetics in rolled U-10 wt.% Mo foil: Effect of post-rolling heat treatment and prior γ-UMo grain size," *Journal of Nuclear Materials,* vol. 496, pp. 215-226, 2017.

[57] P. Li, J. Li, Q. Meng, W. Hu, and D. Xu, "Effect of heating rate on ferrite recrystallization and austenite formation of cold-roll dual phase steel," *Journal of Alloys and Compounds*, vol. 578, pp. 320-327, 2013.

[58] F. G. Caballero, C. Capdevila, and C. G. de Andrés, "Influence of pearlite morphology and heating rate on the kinetics of continuously heated austenite formation in a eutectoid steel," *Metallurgical and Materials Transactions A*, vol. 32, pp. 1283-1291, 2001.

[59] J. Elmer, T. Palmer, W. Zhang, B. Wood, and T. DebRoy, "Kinetic modeling of phase transformations occurring in the HAZ of C-Mn steel welds based on direct observations," *Acta Materialia*, vol. 51, pp. 3333-3349, 2003.

[60] W. Johnson and R. Mehl, "Reaction kinetics in processes of reaction and growth," *Transactions of the Metallurgical Society of AIME*, vol. 135, pp. 42-58, 1939.

[61] M. Avrami, "Kinetics of phase change. I General theory," *The Journal of Chemical Physics*, vol. 7, pp. 1103-1112, 1939.

[62] M. Avrami, "Kinetics of phase change. II Transformation-time relations for random distribution of nuclei," *The Journal of Chemical Physics*, vol. 8, pp. 212-224, 1940.

[63] M. Avrami, "Granulation, phase change, and microstructure kinetics of phase change. III," *The Journal of Chemical Physics*, vol. 9, pp. 177-184, 1941.

[64] A. N. Kolmogorov, "On the statistical theory of the crystallization of metals," *Bulletin of theR Russian Academy of Sciences, USSR*, vol. 1, pp. 355-359, 1937.

[65] M. Fanfoni and M. Tomellini, "The Johnson-Mehl-Avrami-Kohnogorov model: a brief review," *Il Nuovo Cimento D*, vol. 20, pp. 1171-1182, 1998.

[66] C. Wert and C. Zener, "Interference of growing spherical precipitate particles," *Journal of Applied Physics*, vol. 21, pp. 5-8, 1950.

[67] M. Whelan, "On the kinetics of precipitate dissolution," *Metal Science Journal*, vol. 3, pp. 95-97, 1969.

[68] H. Carslaw and J. Jaeger, *Heat in solids* vol. 1: Clarendon Press, Oxford, 1959.

[69] Q. Zuo, F. Liu, L. Wang, C. F. Chen, and Z. H. Zhang, "An analytical model for secondary phase dissolution kinetics," *Journal of Materials Science*, vol. 49, pp. 3066-3079, 2014.

[70] X. Zhang, M. Guo, J. Zhang, and L. Zhuang, "Dissolution of Precipitates During Solution Treatment of Al-Mg-Si-Cu Alloys," *Metallurgical and Materials Transactions B*, vol. 47, pp. 608-620, 2016.

[71] Q. Zuo, F. Liu, L. Wang, C. Chen, and Z. Zhang, "Dissolution of interdendritic σ phase in cast Ni–Fe–Cr alloy," *Materials Science and Technology*, vol. 31, pp. 1288-1297, 2015.

[72] I. Solorzano and W. Gust, "Combined Phenomena of Grain Boundary Migration, Precipitation and Recrystallization in Cu-7.5 at% In," in *Materials Science Forum*, 1992, pp. 659-664.

[73] M. Tałach-Dumańska, P. Ziba, A. Pawłowski, J. Wojewoda, and W. Gust, "Practical aspects of discontinuous precipitation and dissolution," *Materials Chemistry and Physics*, vol. 80, pp. 476-481, 2003/05/26/ 2003.

[74] D. E. Burkes, R. Prabhakaran, J. F. Jue, and F. J. Rice, "Mechanical Properties of DU-xMo Alloys with x = 7 to 12 Weight Percent," *Metallurgical and Materials Transactions A*, vol. 40, pp. 1069-1079, 2009.

[75] D. E. Burkes, R. Prabhakaran, T. Hartmann, J. F. Jue, and F. J. Rice, "Properties of DU–10wt% Mo alloys subjected to various post-rolling heat treatments," *Nuclear Engineering and Design*, vol. 240, pp. 1332-1339, 2010.

[76] P. Beck and L. Demer, "Effect of Composition on Grain Growth in Aluminum-Magnesium Solid Solu tion," *Transactions of the Metallurgical Society of AIME*, vol. 180, p. 147, 1949.

[77] P. A. Beck, "Effect of recrystallized grain size on grain growth," *Journal of Applied Physics,* vol. 19, pp. 507-509, 1948.

[78] P. A. Beck, J. C. Kremer, L. Demer, and M. Holzworth, "Grain growth in high-purity aluminum and in an aluminum-magnesium alloy," *Transactions of the Metallurgical Socity of AIME,* vol. 175, pp. 372-400, 1948.

[79] W. E. Frazier, S. Hu, N. Overman, C. Lavender, and V. V. Joshi, "Short communication on kinetics of grain growth and particle pinning in U-10 wt.% Mo," *Journal of Nuclear Materials,* vol. 498, pp. 254-258, 2018.

[80] Z.-G. Mei, L. Liang, Y. S. Kim, T. Wiencek, E. O'Hare, A. M. Yacout, *et al.*, "Grain growth in U–7Mo alloy: A combined first-principles and phase field study," *Journal of Nuclear Materials,* vol. 473, pp. 300-308, 2016/05/01/ 2016.

[81] D. M. Wachs, C. R. Clark, and R. J. Dunavant, "Conceptual process description for the manufacture of low-enriched uranium-molybdenum fuel," Idaho National Laboratory, Idaho Falls, Idaho, 2008.

[82] G. A. Moore and M. C. Marshall, "Co-Rolled U10Mo/Zirconium-Barrier-Layer Monolithic Fuel Foil Fabrication Process,"; Idaho National Laboratory, INL/EXT-10-17774, Iadho Falls, Idaho, 2010.

[83] T. Fujikawa, M. Moritoki, and K. Homma, "The High Temperature HIP Furnace and Its Application in Densification of Ceramics," in *2nd International Conference on Isostatic Pressing, Stratford–upon–Avon*, 1982, p. 9.

[84] M. Bocanegra-Bernal, "Hot isostatic pressing (HIP) technology and its applications to metals and ceramics," *Journal of Materials Science,* vol. 39, pp. 6399-6420, 2004.

[85] A. E. Dwight, "The uranium-molybdenum equilibrium diagram below 900 C," *Journal of Nuclear Materials,* vol. 2, pp. 81-87, 1960.

[86] C. Peterson, W. Steele, and S. DiGiallonardo, "Isothermal transformation study of some uranium-base alloys," California. Univ., Livermore. Lawrence Radiation Lab.1964.

[87] Y. J. Park, N. Eriksson, R. Newell, D. D. Keiser Jr, and Y. H. Sohn, "Phase decomposition of γ-U (bcc) in U-10 wt% Mo fuel alloy during hot isostatic pressing of monolithic fuel plate," *Journal of Nuclear Materials,* vol. 480, pp. 271-280, 2016.

[88] Y. J. Park, J. Yoo, K. Huang, D. D. Keiser Jr, J. F. Jue, B. Rabin, G. A. Moore, and Y. H. Sohn, "Growth kinetics and microstructural evolution during hot isostatic pressing of U-10 wt.% Mo monolithic fuel plate in AA6061 cladding with Zr diffusion barrier," *Journal of Nuclear Materials,* vol. 447, pp. 215-224, 4// 2014.

[89] R. Newell, A. Mehta, Y. J. Park, D. D. Keiser Jr, and Y. H. Sohn, "Interdiffusion, Reactions, and Phase Transformations Observed during Fabrication of Low Enriched Uranium Monolithic Fuel System for Research and Test Reactors," in *Defect and Diffusion Forum*, 2018, pp. 10-16.

[90] J. F. Jue, T. L. Trowbridge, C. R. Breckenridge, G. A. Moore, M. K. Meyer, and D. D. Keiser Jr, "Effects of heat treatment on U–Mo fuel foils with a zirconium diffusion barrier," *Journal of Nuclear Materials,* vol. 460, pp. 153-159, 2015.

[91] Y. J. Park, N. Eriksson, D. D. Keiser Jr, J. F. Jue, B. Rabin, G. Moore, and Y. H. Sohn, "Microstructural anomalies in hot-isostatic pressed U–10 wt.% Mo fuel plates with Zr diffusion barrier," *Materials Characterization,* vol. 103, pp. 50-57, 5// 2015.

[92] V. Orlov, V. Sergeev, M. Fomishkin, A. Rostovtsev, and A. Kruglov, "Carbon diffusion in uranium during thermal reprocessing in vacuum," *Atomic Energy*, vol. 95, pp. 536-539, 2003.

[93] A. Nomine, D. Bedere, and D. Miannay, "Influence of physio-chemical parameters on the mechanical properties of some isotropic uranium alloys," in *Physical Metallurgy of Uranium Alloys*, 1976.

[94] E. Perez, B. Yao, D. D. Keiser Jr, and Y. H. Sohn, "Microstructural analysis of as-processed U–10 wt.%Mo monolithic fuel plate in AA6061 matrix with Zr diffusion barrier," *Journal of Nuclear Materials*, vol. 402, pp. 8-14, 2010.

[95] A. Robinson, D. Perez, D. Porter, G. Chang, D. Keiser Jr, D. Wachs, *et al.*, "Irradiation Performance of U-Mo Alloy Based "Monolithic" Plate-Type—Design Selection Update" INL/EXT-09-16807 Rev. 1, 2013.

[96] D. D. Keiser Jr, J. F. Jue, B. Miller, J. Gan, A. Robinson, P. Medvedev, J. Madden, D. Wachs, C. Clark, and M. K. Meyer, "Microstructural Characterization of the U-9.1Mo Fuel/AA6061 Cladding Interface in Friction-Bonded Monolithic Fuel Plates Irradiated in the RERTR-6 Experiment," *Metallurgical and Materials Transactions E*, vol. 2, pp. 173-189, 2015.

[97] T. Bierlein and D. Green, "The diffusion of Uranium into Aluminum," *Nuclear Science and Engineering*, vol. 2, pp. 778-786, 1957.

[98] E. Perez, D. D. Keiser Jr, and Y. H. Sohn, "Phase Constituents and Microstructure of Interaction Layer Formed in U-Mo Alloys vs Al Diffusion Couples Annealed at 873 K (600 °C)," *Metallurgical and Materials Transactions A*, vol. 42, pp. 3071-3083, 2011.

[99] E. Perez, B. Yao, D. D. Keiser Jr, and Y. H. Sohn, "Microstructural analysis of as-processed U–10 wt.%Mo monolithic fuel plate in AA6061 matrix with Zr diffusion barrier," *Journal of Nuclear Materials,* vol. 402, pp. 8-14, 2010.

[100] J. Gan, B. Miller, D. D. Keiser Jr, J. F. Jue, J. Madden, A. Robinson, H. Ozaltun, G. Moore, and M. K. Meyer, "Irradiated microstructure of U-10Mo monolithic fuel plate at very high fission density," *Journal of Nuclear Materials,* vol. 492, pp. 195-203, 2017.

[101] R. Willard and A. Schmitt, "Irradiation swelling, phase reversion, and intergranular cracking of U-10 wt.% Mo fuel alloy," Atomics International. Division of North American Aviation, Inc., Canoga Park, California, 1965.

[102] M. Bleiberg, L. Jones, and B. Lustman, "Phase Changes in Pile-Irradiated Uranium-Base Alloys," *Journal of applied Physics,* vol. 27, pp. 1270-1283, 1956.

[103] M. Bleiberg, "Effect of fission rate and lamella spacing upon the irradiation-induced phase transformation of u-9 wt% mo alloy," *Journal of Nuclear Materials,* vol. 1, pp. 182-190, 1959.

[104] J. A. Brinkman, "Production of atomic displacements by high-energy particles," *American Journal of Physics,* vol. 24, pp. 246-267, 1956.

[105] K. Huang, D. D. Keiser Jr, and Y. Sohn, "Interdiffusion, intrinsic diffusion, atomic mobility, and vacancy wind effect in γ (bcc) uranium-molybdenum alloy," *Metallurgical and Materials Transactions A,* vol. 44, pp. 738-746, 2013.

[106] Y. S. Kim, G. L. Hofman, J. S. Cheon, A. B. Robinson, and D. M. Wachs, "Fission induced swelling and creep of U–Mo alloy fuel," *Journal of Nuclear Materials,* vol. 437, pp. 37-46, 2013/06/01/ 2013.

[107] J. Rest, G. Hofman, and Y. S. Kim, "Analysis of intergranular fission-gas bubble-size distributions in irradiated uranium–molybdenum alloy fuel," *Journal of Nuclear Materials*, vol. 385, pp. 563-571, 2009.

[108] H. Ozaltun, M. H. Herman Shen, and P. Medvedev, "Assessment of residual stresses on U10Mo alloy based monolithic mini-plates during Hot Isostatic Pressing," *Journal of Nuclear Materials,* vol. 419, pp. 76-84, 2011.

[109] H. Ozaltun and P. G. Medvedev, "Structural behaviour of monolithic fuel plates during hot isostatic pressing and annealing," 2010.

[110] H. Ozaltun and S. J. Miller, "Evaluation of Blister Behavior for U10Mo Mini fuel plates with cold rolled foils," in *ASME 2012 International Mechanical Engineering Congress and Exposition,* 2012, pp. 1337-1345.

[111] A. Soulami, D. E. Burkes, V. V. Joshi, C. A. Lavender, and D. Paxton, "Finite-element model to predict roll-separation force and defects during rolling of U-10Mo alloys," *Journal of Nuclear Materials,* vol. 494, pp. 182-191, 2017.

[112] W. Mohamed and H. S. Roh, "Influence of Materials Properties on the Irradiation Behavior of U-10Mo Monolithic Mini-Plates," 2015.

[113] G. W. Coffey, K. D. Meinhardt, V. V. Joshi, L. R. Pederson, C. A. Lavender, and D. Burkes, "Concept Feasibility Report for Electroplating Zirconium onto Uranium Foil-Year 2," Pacific Northwest National Laboratory, Richland, Washington, 2015.

[114] D. R. Cummins, K. J. Hollis, C. Liu, M. L. Lovato, and D. E. Dombrowski, "Plasma Sprayed Zirconium Diffusion Barrier Development for Monolithic U-Mo Metallic Fuel," Los Alamos National Laboratory, New Mexico, 2016.

[115] "Standard Test Methods for Determining Average Grain Size," ASTM International, 2013.

[116] M. I. Mendelson, "Average grain size in polycrystalline ceramics," *Journal of the American Ceramic Society,* vol. 52, pp. 443-446, 1969.

[117] E. Case, J. Smyth, and V. Monthei, "Grain-size determinations," *Journal of the American Ceramic Society,* vol. 64, pp. 24-25, 1981.

[118] P. L. Ryder and W. Pitsch, "On the accuracy of orientation determination by selected area electron diffraction," *The Philosophical Magazine: A Journal of Theoretical Experimental and Applied Physics,* vol. 18, pp. 807-816, 1968.

[119] W. C. Oliver and G. M. Pharr, "An improved technique for determining hardness and elastic modulus using load and displacement sensing indentation experiments," *Journal of Materials Research,* vol. 7, pp. 1564-1583, 1992.

[120] W. C. Oliver and G. M. Pharr, "Measurement of hardness and elastic modulus by instrumented indentation: Advances in understanding and refinements to methodology," *Journal of Materials Research,* vol. 19, pp. 3-20, 2004.

[121] S. Sidhu, N. S. Murthy, F. Campos, and D. Zauberis, "Neutron and X-ray diffraction studies of nonstoichiometric metal hydrides," ACS Publications, 1963.

[122] W. Zhu, R. Wang, G. Shu, P. Wu, and H. Xiao, "First-principles study of different polymorphs of crystalline zirconium hydride," *The Journal of Physical Chemistry C,* vol. 114, pp. 22361-22368, 2010.

[123] Z. W. Lu, D. Singh, and H. Krakauer, "Equilibrium properties of hcp titanium and zirconium," *Physical Review B,* vol. 36, pp. 7335-7341, 1987.

[124] A. Devaraj, L. Kovarik, E. Kautz, B. Arey, S. Jana, C. Lavender, and V. V. Joshi, "Grain boundary engineering to control the discontinuous precipitation in multicomponent U10Mo alloy," *Acta Materialia,* vol. 151, pp. 181-190, 2018.

[125] A. Robinson, G. Chang, D. Keiser Jr, D. Wachs, and D. Porter, "Irradiation Performance of U-Mo Alloy Based ‘Monolithic’Plate-Type Fuel–Design Selection," Idaho National Laboratory, INL/EXT-09-16807, Idaho Falls, Idaho, 2009.

[126] D. D. Keiser Jr, J. F. Jue, B. Miller, J. Gan, A. Robinson, and J. Madden, "Observed Changes in As-Fabricated U-10Mo Monolithic Fuel Microstructures After Irradiation in the Advanced Test Reactor," *Journal of Materials,* vol. 69, pp. 2538-2545, 2017.

[127] C. J. Middleton and G. W. Form, "Direct Observation of an Austenite Memory Effect in Low-Alloy Steels," *Metal Science,* vol. 9, pp. 521-528, 1975.

[128] R. Newell, Y. J. Park, A. Mehta, D. D. Keiser Jr, and Y. H. Sohn, "Mechanical properties examined by nanoindentation for selected phases relevant to the development of monolithic uranium-molybdenum metallic fuels," *Journal of Nuclear Materials,* 2017.

[129] Y. H. Duan, Y. Sun, M. J. Peng, and S. G. Zhou, "Stability, elastic properties and electronic structures of L12-ZrAl3 and D022-ZrAl3 up to 40 GPa," *Journal of Physics and Chemistry of Solids,* vol. 75, pp. 535-542, 2014.

[130] C. M. Li, S. M. Zeng, Z. Q. Chen, N. P. Cheng, and T. X. Chen, "First-principles calculations of elastic and thermodynamic properties of the four main intermetallic phases in Al–Zn–Mg–Cu alloys," *Computational Materials Science,* vol. 93, pp. 210-220, 2014.

[131] E. S. Fisher and H. J. McSkimin, "Adiabatic Elastic Moduli of Single Crystal Alpha-Uranium," *Journal of Applied Physics,* vol. 29, pp. 1473-1484, 1958.

[132] M. Waldron, R. Burnett, and S. Pugh, "The mechanical properties of Uranium-Molybdenum alloys," United Kingdom Atomic Energy Authority. Atomic Energy Research Establishment, Harwell, Berks, England1958.

[133] R. L. Mullen, R. Ballarini, Y. Yin, and A. H. Heuer, "Monte Carlo simulation of effective elastic constants of polycrystalline thin films," *Acta Materialia,* vol. 45, pp. 2247-2255, 1997.

[134] L. Fu, J. L. Ke, Q. Zhang, B. Y. Tang, L. M. Peng, and W. J. Ding, "Mechanical properties of L12 type Al3X (X = Mg, Sc, Zr) from first-principles study," P*hysica Status Solidi b,* vol. 249, pp. 1510-1516, 2012.

[135] V. C. Gudla, K. Rechendorff, Z. I. Balogh, T. Kasama, and R. Ambat, "In-situ TEM investigation of microstructural evolution in magnetron sputtered Al–Zr and Al–Zr–Si coatings during heat treatment," *Materials & Design,* vol. 89, pp. 1071-1078, 2016.

[136] K. E. Knipling, D. N. Seidman, and D. C. Dunand, "Ambient- and high-temperature mechanical properties of isochronally aged Al–0.06Sc, Al–0.06Zr and Al–0.06Sc–0.06Zr (at.%) alloys," *Acta Materialia,* vol. 59, pp. 943-954, 2011.

[137] E. Clouet, J. M. Sanchez, and C. Sigli, "First-principles study of the solubility of Zr in Al," *Physical Review B,* vol. 65, p. 094105, 2002.

[138] I. S. Virk and R. A. Varin, "Mechanical behavior and microcracking of cubic ternary zirconium trialuminides," *Metallurgical Transactions A,* vol. 23, pp. 617-625.

[139] C. B. Basak, N. Prabhu, and M. Krishnan, "On the formation mechanism of UZr2 phase," *Intermetallics,* vol. 18, pp. 1707-1712, 2010.

[140] M. Akabori, T. Ogawa, A. Itoh, and Y. Morii, "The lattice stability and structure of delta-UZr2 at elevated temperatures," *Journal of Physics Condensed Matter,* vol. 7, pp. 8249-8257, 1995.

[141] Y. Park, D. D. Keiser Jr, and Y. H. Sohn, "Interdiffusion and reactions between U–Mo and Zr at 650 °C as a function of time," *Journal of Nuclear Materials,* vol. 456, pp. 351-358, 2015.

[142] M. Zinkevich and N. Mattern, "Thermodynamic assessment of the Mo-Zr system," *Journal of Phase Equilibria,* vol. 23, pp. 156-162, 2002.

[143] B. Beeler, C. Deo, M. Baskes, and M. Okuniewski, "First principles calculations of the structure and elastic constants of α, β and γ uranium," *Journal of Nuclear Materials,* vol. 433, pp. 143-151, 2013.

[144] M. Yovanovich, "Micro and macro hardness measurements, correlations, and contact models," in *Collection of technical papers—44th AIAA aerospace sciences meeting*, 2006, pp. 11702-11729.

[145] B. S. Seong, C. H. Lee, J. S. Lee, H. S. Shim, J. H. Lee, K. H. Kim, C. K. Kim, and V. Em, "Neutron diffraction study of U–10 wt% Mo alloy," *Journal of Nuclear Materials,* vol. 277, pp. 274-279, 2000.

[146] V. Orlov and V. Teplinskaya, "Structural features of martensite α-phases in alloys of uranium with transition metals," *Atomic Energy,* vol. 86, pp. 118-125, 1999.

[147] V. Orlov, V. Teplinskaya, and N. Chebotarev, "Decomposition of a metastable solid solution in uranium-molybdenum alloy," *Atomic Energy,* vol. 88, pp. 42-47, 2000.

[148] B. Howlett, "A study of the shear transformations from the gamma-phase in uranium-molybdenum alloys containing 6.0–12.5 at% molybdenum," *Journal of Nuclear Materials,* vol. 35, pp. 278-292, 1970.

[149] C. T. Olofson, G. E. Meyer, and A. L. Hoffmanner, "Processing and applications of depleted uranium alloy products," DTIC Document, 1976.

[150] A. Padel and C. De Novion, "Elastic Constants of the Carbides, Nitrides, and Oxides of Uranium and Plutonium," SECPER, Fontenay-aux-Roses, France, 1969.

[151] W. Martienssen and H. Warlimont, *Springer Handbook of Condensed Matter and Materials Data*: Springer Science & Business Media, 2006.